Dosimetry of a miniature x-ray source used in intraoperative radiation therapy

Peter G. F. Watson

Department of Physics
McGill University

A thesis submitted to McGill University in partial fulfillment of the requirements
of the degree of
Doctor of Philosophy

December 2018

For Lorri and Petey.

"It's been emotional."

–Big Chris, **Lock, Stock and Two Smoking Barrels** (1998)

Acknowledgements

When I started graduate school, I really didn't know where I would end up. Eleven years, two M.Sc. degrees, and one kid later, here we are! This period in my life has been interesting and complex. I have faced my hardest personal challenges thus far, yet also experienced great joys. It has been a bittersweet journey, and I am ready for the next chapter.

I would like to thank everyone who has helped and supported me over the (many) years. Firstly, to my supervisor Dr. Jan Seuntjens for his guidance, insight, and expert knowledge of radiation dosimetry and monte carlo methods. His hands-off management approach has helped me to become a better, more self-sufficient researcher and scientist. I also thank him for being understanding of my student-parent situation and allowing me a lot of schedule flexibility during my studies (also, for procuring funding for my project!). To my doctoral committee members, Drs. Malcolm McEwen and Stephen Davis, for their comments and feedback which has helped to shape the work presented in this thesis. To Dr. Hamed Bekerat for taking the time to assist me with operating the orthovoltage unit at the Jewish General Hospital, and for passing on his experience with EBT3 Gafchromic film dosimetry. To Dr. Pavlos Papaconstadopoulos for sharing his matlab codes, and being an all-around great office mate. To Dr. Marija Popovic who helped teach me how to operate the INTRABEAM, assisted with the half-value layer measurements, and provided the link to the clinic. To Marc-Andre Renaud for his expertise in all things coding, and for helping me debug/troubleshoot any problems with my programs (also a great office mate, right up there with Pavlos). To Joe Larkin for building the film holder. To all my friends, colleagues, and fellow students at the MPU for the camaraderie and stimulating conversations over lunch. To Margery Knewstubb and Tatjana Nisic for taking care of all administrative issues. To Hans Zimmer, Trent Reznor, and Atticus Ross for composing great music conducive to writing a thesis. The french translation of my abstract was kindly proof-read by Veronique Fortier.

Finally, my sincere appreciation to my family. To my parents for raising me to do my best, and always being there for me. To my wife, Lorri-Anne, for her support and love over an unreasonably long time span. We did it, your husband is no longer a student! And to my son Petey, who makes this and everything else worthwhile.

Abstract

The INTRABEAM System (Carl Zeiss Meditech AG, Jena, Germany) is a miniature x-ray source operating at 50 kVp for use in intraoperative radiation therapy (IORT). Electrons are accelerated towards a hemispherical thin gold target to produce a radially isotropic photon intensity distribution, consisting of bremsstrahlung and fluorescence photons. The INTRABEAM source is primarily used to treat breast cancer, and has shown to be a viable option compared to external beam radiation therapy through the results of the TARGIT-A clinical trial.

The x-ray source was modeled using EGSnrc, a Monte Carlo (MC) particle transport code. Source and applicator materials and dimensions were taken from published data and specifications provided by the manufacturer. The simulated spectrum results were compared with previously published simulation and measurement results, and validated with measurements of half-value layer performed in-air, and percent depth dose measurements in a water phantom. The effect of including explicit $M-$ and $N-$subshell atomic transitions versus averaged shells in the source simulations was investigated, and was found to be appreciable. The efficiency of using a phase space source of all particles leaving the surface of the INTRABEAM source probe, rather than an electron source striking the gold target was also investigated.

A dose formalism was proposed for calculating the absorbed dose to water from INTRABEAM bare source measurements performed in a water phantom with an air-kerma calibrated ionization chamber, relying on MC-calculated dose ratios. It was found that the formalism systematically calculated a larger dose (up to 23% greater) than the equation recommended by the manufacturer. It was determined that the uncertainty in the electrode separation of the PTW 34013 parallel plate ionization chamber used had a significant effect on the dose calculation uncertainty.

The MC-derived formalism (C_Q) and manufacturer recommended (Zeiss) dose determinations were compared with the dose calculation used in the TARGIT protocol as a function of depth in water. Radiochromic film measurements of absorbed dose were also performed and compared. The dose determined by the C_Q, Zeiss, and film methods generally agreed considering measurement uncertainties (5-6%). The TARGIT dose was considerably less than the other methods by 14% to

80%, suggesting that the TARGIT dose underestimates the physical dose to water. The results presented in this work provide strong evidence that the doses delivered in breast IORT treatments following the TARGIT protocol were significantly greater than the dose prescribed, and varied with the size of spherical applicator used.

Résumé

Le système INTRABEAM (Carl Zeiss Meditech AG, Jena, Allemagne) est une source miniature de rayons X qui fonctionne à 50 kVp pour utilisation en radiothérapie intra-opératoire (IORT). Dans la source, les électrons sont accélérés vers une cible aurifère hémisphérique produisant ainsi une distribution d'intensité des photons radialement isotrope, incluant des photons Bremsstrahlung et de fluorescence. Le système INTRABEAM est principalement utilisé pour traiter le cancer du sein et il s'est révélé être une option viable par rapport à la radiothérapie par faisceau externe, d'après les résultats de l'essai clinique TARGIT-A.

La source de rayons X a été modélisée en utilisant EGSnrc, un code de transport des particules basé sur la méthode Monte Carlo (MC). Les matériaux et les dimensions de la source et de l'applicateur ont été extraits des données publiées et des spécifications fournies par le fabricant. Les résultats du spectre simulé ont été comparés aux résultats de mesures et de simulations précédemment publiés, puis ils ont été validés à l'aide de mesures de la couche de demi-atténuation effectuées dans l'air et de mesures de pourcentage de dose en profondeur dans un fantôme d'eau. L'effet de l'inclusion dans les simulations des transitions atomiques explicites des sous-couches $M-$ et $N-$ par rapport à des coques moyennées a été étudié et a été jugé appréciable. L'efficacité d'utiliser une source "phase-space" de toutes les particules qui quittent la surface de la sonde INTRABEAM, plutôt qu'une source d'électrons frappant la cible en or, a également été étudiée.

Un formalisme de dose a été proposé pour calculer la dose absorbée dans l'eau à partir de mesures de source INTRABEAM nue effectuées dans un fantôme d'eau avec une chambre d'ionisation calibrée au kerma dans l'air, en se basant sur les rapports de dose calculés par MC. Il a été constaté que le formalisme calculait systématiquement une dose supérieure (jusqu'à 23% supérieure) à l'équation recommandée par le fabricant. Il a été déterminé que l'incertitude sur la séparation des électrodes de la chambre d'ionisation à plaques parallèles PTW 34013 utilisée avait un effet significatif sur l'incertitude du calcul de la dose.

Les formalismes de calcul de dose dérivé de MC (C_Q) et recommandé par le fabricant (Zeiss) ont été comparés à celui utilisé dans le protocole TARGIT en fonction de la profondeur dans

l'eau. Des mesures sur film radiochromique de la dose absorbée ont également été effectuées et comparées. La dose déterminée par les méthodes C_Q, Zeiss et film concordait généralement, compte tenu des incertitudes de mesure (5-6%). La dose de TARGIT était considérablement inférieure aux autres méthodes de 14 à 80%, ce qui suggère que la dose de TARGIT sous-estime la dose physique dans l'eau. Les résultats présentés dans ce travail fournissent des preuves solides que les doses délivrées dans les traitements IORT du sein selon le protocole TARGIT étaient significativement supérieures à la dose prescrite et variaient en fonction de la taille de l'applicateur sphérique utilisé.

Contents

Dedication iii

Acknowledgements v

Abstract vii

Résumé ix

List of Figures xv

List of Tables xxi

List of Abbreviations xxiii

Preface and Contribution of Authors xxv

1 Introduction 1
- 1.1 Breast Cancer and Radiation Therapy 1
  - 1.1.1 History of Breast Cancer Treatment 1
  - 1.1.2 Accelerated Partial Breast Irradiation 2
- 1.2 The INTRABEAM System 5
  - 1.2.1 Clinical Treatments 6
  - 1.2.2 Issues with INTRABEAM Dosimetry 7
- 1.3 Thesis Objectives 7
- 1.4 Thesis Outline and Scientific Contributions 8

2 Radiation Dosimetry and INTRABEAM **11**
2.1 Preface . . . 11
2.2 Introduction . . . 11
2.3 Dosimetry definitions and concepts . . . 12
  2.3.1 Dosimetric Quantities . . . 12
  2.3.2 Radiation Quality . . . 18
2.4 Radiation Detectors . . . 19
  2.4.1 Detector Response and Calibration . . . 19
  2.4.2 Desirable Properties of Dosimeters . . . 20
  2.4.3 Various Types of Dosimeters . . . 21
  2.4.4 Ionization Chambers . . . 21
  2.4.5 Radiochromic Film . . . 24
  2.4.6 Cavity Theory . . . 25
2.5 Kilovoltage X-ray Beam Reference Dosimetry . . . 30
  2.5.1 Primary standards for kV x-ray beams . . . 30
  2.5.2 Primary Standards for Miniature X-ray Sources . . . 30
  2.5.3 kV Dosimetry Protocols: Air-Kerma Calibration . . . 31
  2.5.4 kV Dosimetry Protocols: Absorbed Dose to Water Calibration . . . 33
  2.5.5 kV Dosimetry Protocols: Brachytherapy . . . 34
2.6 Dosimetry of the INTRABEAM System . . . 36
2.7 Conclusion . . . 38

3 Monte Carlo Simulations of the INTRABEAM System **39**
3.1 Preface . . . 39
3.2 Introduction . . . 39
3.3 Monte Carlo Particle Transport . . . 40
  3.3.1 EGSnrc Radiation Transport Software . . . 42
  3.3.2 Modeling the INTRABEAM source . . . 47
3.4 Materials and Methods . . . 49
  3.4.1 Photon Fluence Spectrum . . . 51
  3.4.2 Half Value Layer . . . 51
  3.4.3 Phase Space Source . . . 53
3.5 Results . . . 54
  3.5.1 Photon Spectrum . . . 54

3.5.2 Half Value Layer 57
3.5.3 Phase Space Source 60
3.6 Conclusion 68

4 Effect of explicit *M* and *N*-shell atomic transitions on a low-energy x-ray source 69
4.1 Preface 69
4.2 Abstract 70
4.3 Introduction 70
4.4 Methods 71
4.4.1 In-Air: Photon fluence spectra and HVL 71
4.4.2 In-Water: Relative depth dose 72
4.5 Results 72
4.5.1 In-Air: Photon fluence spectra and HVL 72
4.5.2 In-Water: Relative depth dose 73
4.6 Discussion 75
4.7 Conclusions 76
4.8 Acknowledgments 76

5 Determination of absorbed dose to water from a miniature kilovoltage X-ray source using a parallel-plate ionization chamber 79
5.1 Preface 79
5.2 Abstract 80
5.3 Introduction 80
5.3.1 The INTRABEAM system: source description, dosimetry, and QA . . . 81
5.3.2 Zeiss water phantom dosimetry protocol 82
5.3.3 Proposed absorbed dose formalism 83
5.4 Materials and methods 84
5.4.1 Monte Carlo Simulations 84
5.4.2 Measurements 89
5.4.3 Determination of absorbed dose to water 91
5.5 Results 92
5.5.1 MC model validation 92
5.5.2 Determination of absorbed dose to water 94
5.6 Discussion 97
5.7 Conclusion 98

5.8 Acknowledgments 99
5.9 Appendix 103
  5.1.1 N_{gas} and $(W/e)_{\text{air}}$ for kV photon beams 103
  5.1.2 Methods and materials 104
  5.1.3 Results and discussion 104

6 An investigation into the INTRABEAM miniature X-ray source dosimetry using ionization chamber and radiochromic film measurements 107
6.1 Preface 107
6.2 Abstract 108
6.3 Introduction 108
  6.3.1 INTRABEAM Dosimetry 109
  6.3.2 Purpose 112
6.4 Materials and Methods 112
  6.4.1 Ionization Chamber Measurements 113
  6.4.2 Film Measurements 118
6.5 Results 125
  6.5.1 Ion Collection Efficiency and Polarity Correction 125
  6.5.2 Timer Error 126
  6.5.3 EBT3 Film Calibration 126
  6.5.4 Film Holder Correction Factor 126
  6.5.5 Absorbed Dose Measurements 127
6.6 Discussion 128
6.7 Conclusions 135
6.8 Acknowledgments 135

7 Conclusion 137
7.1 Summary 137
7.2 Future Research Directions 138
7.3 Outlook 140

Bibliography 141

List of Figures

Figure 1.1 The INTRABEAM System x-ray source (XRS) and its sub-components. Image taken from [1] . . . 6

Figure 3.1 The INTRABEAM source with spherical applicator mounted on a floor stand. The inset on the right shows the internal components of the x-ray source. Image taken from Sethi *et al.* [2] . . . 48

Figure 3.2 Rendering of the INTRABEAM bare probe geometry used in EGSnrc simulations. . . . 49

Figure 3.3 INTRABEAM spherical applicators ranging in diameter from 1.5 cm to 5 cm. Image taken from Holmes *et al.* [3] . . . 50

Figure 3.4 EGSnrc geometries of an INTRABEAM spherical applicator (3.5 cm diameter) used in the simulation of photon fluence and HVL. The simplified model (a) was found to be insufficient for calculating the HVL. . . . 50

Figure 3.5 Experimental setup during attenuation measurements of the INTRABEAM source. . . . 53

Figure 3.6 The simulated photon fluence spectra of the INTRABEAM source for the bare probe and spherical applicators (3.5, 4.0, and 4.5 cm diameter). The source parameters of Yanch and Harte [4] were used. . . . 55

Figure 3.7 Simulated photon fluence spectra of the INTRABEAM bare probe using source parameters taken from Yanch and Harte [4], and Nwankwo *et al.* [5] The fluorescent peaks due to differences in material compositions have been identified. 56

Figure 3.8 The effect of enabling electron impact ionization (EII) on the photon fluence spectrum is evidenced in the increase of fluorescence photons. Inset shows zoomed in region of fluorescent lines. . . . 57

Figure 3.9 (a) INTRABEAM photon fluence spectra calculated with and without explicit $M-$ and $N-$subshell transitions [6]. (b) Explicit $M-$ and $N-$subshell transitions are required in EGSnrc for agreement with INTRABEAM fluorescence peak energies as calculated with GEANT4 (spectrum provided courtesy of C. Nwankwo). 58

Figure 3.10 The presence of a lead collimator used during HVL measurements was found to introduce fluorescence photons coming off of the collimator ($L-$lines of Pb) which had a significant effect on the HVL. Inset highlights the low energy region of fluorescent lines. 59

Figure 3.11 Comparison of measured and simulated (not accounting for lead collimator or applicator air channel) HVLs for the INTRABEAM source. A large discrepancy can be seen in the spherical applicator HVLs. Following this result, a more detailed model of the spherical applicators including the lead collimator was investigated. 60

Figure 3.12 Comparison of measured and simulated attenuation curves of the INTRABEAM source bare probe and spherical applicators. 61

Figure 3.13 Measured and simulated HVLs for the INTRABEAM bare probe and spherical applicators. The presence of the lead collimator and applicator air channel were accounted for in the EGSnrc simulation. 62

Figure 3.14 The INTRABEAM bare probe photon fluence spectra as calculated with a phase-space and electron source. Below, it can be seen that the difference between the two spectra are within statistical uncertainties. 63

Figure 3.15 (Top) The INTRABEAM bare probe relative depth dose curve calculated with a phase-space and electron source, and (Bottom) the local percent difference relative to the electron source. The dose curves were normalised to 5 mm depth in water. 64

Figure 3.16 The relative efficiency gain of using a phase-space over an electron source in calculating the dose to water from the INTRABEAM bare probe, as a function of depth in water. the numbers in the legend refer to the job splitting (amount of parallelization). 65

Figure 3.17 The same relative efficiency gain plot of figure 3.16 (on a single CPU core), but with all VRTs turned off. 66

Figure 3.18 The relative efficiency gain in calculating the dose to water by using VRTs (IPSS, XCSE, and range-based RR) for a phase-space and electron source. 67

Figure 4.1 50 kVp photon fluence spectra from a thin gold target, calculated with and without *M* and *N*-shell averaging. The energy range of the x-axis was limited to focus on the gold *L*-shell fluorescence photons. 73

Figure 4.2 a) The effect of *M* and *N*-shell averaging on RDD. Curves were normalised to dose at 3 mm depth from source. b) Local percent difference between RDDs in a). c) The effect of *M* and *N*-shell averaging on absolute depth dose. d) Percent difference between depth dose curves in c). All error bars are estimated by the MC statistical uncertainty. 74

Figure 4.3 Normalised 50 kVp photon fluence spectra at various depths in water. Fluence was scored across a circular plane ($r = 0.5$ cm). 75

Figure 5.1 (Left axis) The HVL of the INTRABEAM source as a function of depth in water. (Right axis) The corresponding $(\bar{\mu}_{en}/\rho)_{water}/(\bar{\mu}_{en}/\rho)_{air}$ for the INTRABEAM photon spectra as a function of depth in water. Results were calculated using the EGSnrc model described in section 5.4.1 83

Figure 5.2 Rendering of INTRABEAM source with PTW 34013 ionization chamber inside its waterproof holder. 87

Figure 5.3 T-series kV reference photon beam spectra provided at PTB. These spectra were measured in air at 30 cm source-to-detector distance. Courtesy of Ludwig Büermann. 89

Figure 5.4 Simulated INTRABEAM 50 $\mathrm{kV_p}$ photon spectra in air for source model parameters taken from Yanch and Harte (see table 5.1) and Nwankwo *et al.*. Spectra are normalised to the area under the curve. 92

Figure 5.5 Measured and simulated percentage depth dose curves in water for the Zeiss INTRABEAM, normalised at 5 mm depth (inset shows log scale). The simulated PDDs were calculated with both the Yanch and Harte, and Nwankwo *et al.* source models. The effect of the presence of the waterproof chamber holder can be seen. 94

Figure 5.6 Simulated and measured PTW 34013 ionization chamber k_Q values in T-series kV reference beams. Measured values were taken from the calibration certificates (PTW, Germany) of two individual chambers (SN000235 and SN000429). Measurement uncertainty was reported as 2%. 95

Figure 5.7 Ratio of $[D_{\mathrm{gas}}/K_a]$ for PTW 34013 ionization chamber in kV reference beam qualities. 96

Figure 5.8 (Top) Ratio of $[D_w/D_{\text{gas}}]$ for PTW 34013 ionization chamber with INTRABEAM source in water. The chamber effective point of measurement was defined as the inside of the entrance foil, or (Bottom) the air cavity centroid. 100

Figure 5.9 Comparison of the ratio of $[D_w/D_{\text{gas}}]$ calculated with the Yanch and Harte, and Nwankwo *et al.* INTRABEAM source models for a PTW 34013 chamber with nominal plate separation. Both curves agree well within uncertainties. . . . 101

Figure 5.10 (Top) INTRABEAM ionization chamber conversion factor C_Q for PTW 34013 chamber calibrated in T30 kV reference beam as a function of depth in water, with the effective point of measurement defined as the inside of the chamber entrance foil, or (bottom) the air cavity centroid. 102

Figure 5.11 (Dashed line) The combined values of the initial ion correction factor, k_{ii}, and $(W/e)_{\text{air}}$ energy dependence correction factor, k_w, taken from ICRU Report 90. (Solid lines) Photon fluence spectra from the INTRABEAM source at 1 mm depth in water, both with and without the presence of an air-filled ionization chamber (PTW 34013). Here, we use the photon fluence spectra to calculate the weighted average of $k_{ii}k_w$ to assess its variation with the relevant photon beam qualities 105

Figure 6.1 Fitted functions (solid lines) and confidence intervals (dashed lines) to the INTRABEAM ionization chamber conversion factor C_Q for a PTW 34013 chamber as a function of depth in water. Thick, thin and nominal refer to the modeled chamber plate separation. 116

Figure 6.2 Rendering of experimental setup during film irradiations in water with the INTRABEAM. This geometry was used to calculate the film holder correction factor. 124

Figure 6.3 Calibration curves for EBT3 Gafchromic film (red channel) for a range of kV photon beam qualities. 127

Figure 6.4 (Top) Film holder correction factor as a function of depth in water. (Bottom) Attenuation coefficient of water and EBT3 gafchromic film calculated with XCOM. The attenuation coefficient of EBT3 crosses that of water at around 21 keV due to competing effects of Compton scattering (proportional to electron density) and photoelectric effect (proportional to effective atomic number). . . . 132

Figure 6.5 The absorbed dose to water as a function of depth, as determined with ionization chamber methods and film. Results are shown in a (top) linear and (bottom) log dose scale. At all depths, the lowest dose was measured by the TARGIT method. 133
Figure 6.6 Percent difference of absorbed dose as measured with EBT3 film, and the C_Q and Zeiss ionization chamber methods compared to the TARGIT dose. 134

List of Tables

Table 3.1 Comparison of INTRABEAM source parameters used in Monte Carlo simulations. Specifications taken from Yanch and Harte [4] and Nwankwo *et al.* [5] 49

Table 3.2 Comparison of simulated (EGSnrc) and published (Reported) INTRABEAM HVL values. The simulation source-to-detector distance was set to match the experimental setup used in the reported references. (Broad) refers to measurements made with an uncollimated beam. 62

Table 5.1 Comparison of INTRABEAM source parameters used in Monte Carlo simulations. Specifications taken from Yanch and Harte (1996) and Nwankwo *et al.* (2013). 86

Table 5.2 Average of $k_{ii}k_w$ weighted by photon fluence spectrum. Values are shown both with and without the presence of a PTW 34013 ionization chamber. Uncertainties on the values were calculated to be at the fifth decimal place. 106

Table 6.1 Uncertainty budget in calculating absorbed dose to water with an ionization chamber using the Zeiss method. All values are in percent. 117

Table 6.2 Uncertainty budget in calculating absorbed dose to water with an ionization chamber using the TARGIT method. All values are in percent. 117

Table 6.3 Uncertainty budget in calculating absorbed dose to water with an ionization chamber using the C_Q method. All values are in percent. 118

Table 6.4 Orthovoltage beam qualities used to calibrate EBT3 films. 118

Table 6.5 HVL of INTRABEAM source at various depths in water. Results were calculated from simulated spectra. 123

Table 6.6 Overall elemental composition of EBT3 Gafchromic film in atomic percent. The effective atomic number and density are also listed. 125

Table 6.7 Uncertainty budget in calculating absorbed dose to water with film. All values are in percent. 125
Table 6.8 The depth dose rate as reported by the calibration file (calib) and as measured by the TARGIT method for INTRABEAM source XRS S/N 507299. The percent error from the calibration data was found to be within the measurement uncertainty (see table 6.2) 128

List of Abbreviations

AAPM	American Association of Physicists in Medicine
APBI	Accelerated Partial Breast Irradiation
CPE	Charged Particle Equilibrium
CRT	Conformal Radiation Therapy
CSDA	Continuous Slowing Down Approximation
EADL	Livermore Evaluated Atomic Data Library
EII	Electron Impact Ionization
FAC	Free-Air Ionization Chamber
HVL	Half-value Layer
IAEA	International Atomic Energy Agency
IMRT	Intensity Modulated Radiation Therapy
IORT	Intraoperative Radiation Therapy
IPSS	Intermediate Phase-Space Storage
kV	Kilovoltage
MC	Monte Carlo
MV	Megavoltage
netOD	Net Optical Density

NIST	National Institute of Standards and Technology
PDD	Percent Depth Dose
POM	Point Of Measurement
RAKR	Reference Air-Kerma Rate
RDD	Relative Depth Dose
ROI	Region Of Interest
RR	Russian Roulette
SDD	Source-to-Detector Distance
VRT	Variance Reduction Technique
WAFAC	Wide-Angle Free-Air Ionization Chamber
WBI	Whole Breast Irradiation
XCSE	Photon Cross-Section Enhancement

Preface and Contribution of Authors

This thesis consists of three manuscripts of which I was the first author, published in Medical Physics (Chapter 4 and Chapter 6) and Physics in Medicine and Biology (Chapter 5). In all cases, I performed the simulations and experiments, and wrote the manuscript. My supervisor, Prof. Jan Seuntjens, provided guidance in the conception and development of each research study.

In Chapter 5, Dr. Marija Popovic provided assistance in performing the half-value layer measurements and depth dose measurements with the INTRABEAM system. In Chapter 6, Dr. Hamed Bekerat assisted in the half-value measurements and reference dosimetry of the orthovoltage x-ray beams used to calibrate the radiochromic films, in addition to providing his expertise on EBT3 film energy dependence. Dr. Pavlos Papaconstadopoulos wrote the MATLAB scripts which were used to perform the image analysis and dose calculation of the radiochromic films. Dr. Stephen Davis helped to further develop the scope of the manuscript and offered valuable suggestions, drawing from his expertise in the dosimetry of miniature low-energy x-ray sources. All co-authors reviewed the manuscripts.

1

Introduction

1.1 Breast Cancer and Radiation Therapy

In 2012, 14.1 million new cases of cancer were reported worldwide, with 1.7 million of these cases incidences of female breast cancer [7]. In Canada, the Canadian Cancer Society estimates that over 200 000 Canadians will be diagnosed with cancer in 2017, and of these 26 300 will be new cases of female breast cancer. It is predicted that 1 in 8 Canadian women will develop breast cancer in their lifetime. Fortunately, the female breast cancer mortality rate has been declining in Canada since the mid-1980s, from 41.6 deaths per 100 000 to a projected rate of 23.2 deaths per 100 000 [8]. This downward trend is most likely due to increased mammography screening and more effective therapies following surgery.

1.1.1 History of Breast Cancer Treatment

Historically, breast cancer has been treated by the surgical excision of the tumour, going back to Leonides of Alexandria in the 1st century B.C.E. [9] Progress was made in surgical techniques over the centuries, following the introduction of cautery, disinfection, sterilisation and anaesthesia.

In 1894, William S. Halstead pioneered the “radical mastectomy”, a procedure where the entire breast and *pectoralis major* were removed to prevent the spread and recurrence of the cancer [10]. This practice remained standard of care until the 1970s, when the use of breast-conserving limited surgery (lumpectomy) in combination with chemotherapy and radiation therapy were investigated. A clinical trial (B-06) was started in 1976, conducted by the National Surgical Adjuvant Breast and Bowel Project, which followed 1843 women with breast cancer who were randomly assigned treatments of total mastectomy, lumpectomy, or lumpectomy with whole-breast irradiation. It was observed that the five year survival rates of disease-free survival, distant disease-free survival, and overall survival were not significantly different between patients in the three groups [11]. A follow-up study was performed after 20 years, which reported a similar observation on the survival rate of the three treatment groups. However, significant differences were reported in the cumulative incidences of tumour recurrence in the ipsilateral breast (i.e., breast which had contained the initial tumour) between patients receiving lumpectomy with or without radiation therapy (14.3% vs 39.2%, respectively) [12]. Subsequent studies have yielded similar conclusions on the success of radiation therapy post-surgery for breast cancer [13], establishing it as a standard of care [14].

1.1.2 Accelerated Partial Breast Irradiation

Unfortunately, not all breast cancer patients have easy access to radiation therapy [15], and even for those who do, the typical course of treatment (daily irradiations delivered over a period of six to six and a half weeks) can be stressful and inconvenient. To address this issue, the concept of accelerated partial breast irradiation (APBI) was investigated, where by limiting the volume of irradiated breast tissue the total treatment time could be reduced greatly [16]. The clinical and pathological motivation for APBI stemmed from observations that most local recurrences of cancer in breast patients would appear in a region surrounding the original tumour bed [17, 18]. Several different techniques have been developed for APBI, the most prominent being: multicatheter interstitial brachytherapy, intracavitary brachytherapy, external beam radiation therapy (3D conformal and intensity modulated), and intraoperative radiation therapy [19].

Multicatheter Interstitial Brachytherapy

Multicatheter interstitial brachytherapy involves the placement of ten to twenty catheters through the breast, surrounding the lumpectomy cavity. During treatment, a radioactive source (ex: Iodine-125 or Iridium-192 for low dose rate or high dose rate treatments, respectively) is precisely positioned along each catheter for a specified amount of time to deliver a homogeneous dose of radiation to the tumour bed and surrounding margin (1–3 cm). Clinical studies have shown that multicatheter interstitial brachytherapy treatments can provide similar local cancer control to whole breast irradiation with few side effects [20, 21] and is a treatment strongly recommended by the American Brachytherapy Society (ABS) [22], however access to this technique is limited to select institutions. As well, many prospective patients perceive the procedure to be potentially painful and opt for another treatment modality [19].

Intracavitary Brachytherapy

In intracavitary brachytherapy, an applicator is inserted into the lumpectomy cavity and a radioactive source (typically Iridium-192) is positioned within the applicator to deliver a targeted amount of radiation to the tissue surrounding the applicator surface. One such applicator design is the MammoSite, which consists of a balloon catheter which is inserted in the cavity and inflated with a saline solution. MammoSite treatments deliver a dose of 34 Gy to the applicator surface in ten fractions, twice daily. An American Society of Breast Surgeons (ASBS) registry trial (1440 patients) of breast APBI using MammoSite found good local cancer control after five years (3.8%), and good to excellent cosmesis in 90.6% of patients [23]. However, despite promising results, the stringent guidelines for appropriate selection of patients to be treated with MammoSite have limited its clinical use [19]. For greater flexibility in treatment planning and dose delivery, multi-catheter applicators such as the MammoSite ML and Contura (balloon), or SAVI (no balloon) have been developed. Results from a Contura registry trial reported a three year local cancer recurrence rate of 2.2%, with 88% good to excellent cosmesis outcomes [24].

External-Beam Radiation Therapy

In external beam APBI, a targeted dose of radiation is delivered to the tumour bed (plus additional margin) using an external linear accelerator, and thus does not require any device insertion into the patient. External beam APBI can be performed using three-dimensional conformal radiotherapy (3D-CRT), where dose to the target tissues is optimised given initial beam angles, and intensity-modulated radiotherapy (IMRT), where the dose to defined target volumes is optimised using inverse-planning software (IMRT can be thought of as an advanced type of 3D-CRT). The RAPID trial investigated the use of 3D-CRT APBI versus whole breast irradiation in 2135 patients. Randomised APBI patients received 38.5 Gy in ten fractions, twice daily. After three years follow-up, it was reported that the APBI cohort had increased rates of toxicity and worse cosmesis than whole breast irradiation [25]. However, another randomised trial (NSABP B-39) found no significant differences in toxicities between 3D-CRT APBI and whole breast irradiation after 42.6 months [26]. These conflicting results may be due to differences in the volume of breast tissue receiving dose [27]. Advantages of 3D-CRT APBI are that it is non-invasive, available at most hospitals, and has been shown to be the most cost-effective modality (in the U.S.A.) [28].

A randomised trial at the University of Florence compared IMRT APBI (30 Gy in five fractions, every other day) to whole breast irradiation and found no difference in the local cancer recurrence after five years, with reduced toxicity and improved cosmesis in the APBI arm [29]. Similar five year results were reported by the UK IMPORT LOW trial, which found IMRT APBI (40 Gy in 15 fractions) to be non-inferior to whole breast irradiation [30]. Based on this randomised data, IMRT APBI is strongly recommended by the ABS [22].

Intraoperative Radiation Therapy

Intraoperative radiation therapy (IORT) delivers a single dose of radiation to the tumour bed immediately following surgical resection, usually performed in the operating room. IORT can also be performed post-pathology, where the surgical cavity is reopened and irradiated at a later date. The single day treatment of IORT is logistically advantageous for the patient compared to the multi-day treatments of other APBI techniques. The most common techniques of IORT use mobile electron accelerators (3-12 MeV) or low energy x-rays (50 kV_p), which have characteristic dose distributions giving a large dose to the target tissue while sparing healthy tissue a few centimeters away [31].

The performance of electron IORT was investigated in the clinical ELIOT trial, which compared the outcomes of breast patients treated with 6-9 MeV electrons (21 Gy) to whole breast irradiation (50 Gy in 25 fractions, with additional 10 Gy boost to tumour bed in 5 fractions). While the overall survival rate after five years did not differ between the two groups, the local cancer recurrence rate was found to be significantly greater for the electron IORT patients (4.4% vs 0.4%) [32].

The TARGIT-A trial compared whole breast irradiation to IORT performed with 50 kV_p x-rays (20 Gy) delivered with a miniature x-ray source (The INTRABEAM System (Carl Zeiss Meditec AG, Jena, Germany)). The five year rate of local cancer recurrence was found to be larger with IORT (3.3% vs 1.3%), however this difference was within the tolerance criteria of the study (2.5%), with TARGIT IORT reported as a non-inferior treatment to whole breast irradiation [33, 34]. In addition, patients treated with IORT had fewer high grade skin toxicities, and fewer non-breast cancer-related deaths than with whole breast irradiation. The interpretations of the TARGIT-A results are divided, with proponents arguing that IORT using the INTRABEAM possesses a better health care value (fewer resources needed than external beam radiotherapy) and should be a standard of care [34, 35], while detractors highlight the increased rates of local recurrence, the lack of image guidance, and differences in the dosimetry [36, 22].

Ongoing IORT Clinical Trials

There are a number of breast IORT clinical trials currently accruing patients at the time of writing. The TARGIT-US trial is a registry trial taking place in the USA, with the objective of studying the efficacy and toxicity of breast INTRABEAM IORT with or without whole breast irradiation (ClinicalTrials.gov Identifier: NCT01570998). The technique and doses used are the same as in the TARGIT-A trial. The TARGIT-B trial is a randomised trial designed to test whether a tumour bed boost (an additional dose to the tissue surrounding the surgical cavity) delivered with INTRABEAM IORT is superior to an external beam radiotherapy boost (ClinicalTrials.gov Identifier: NCT01792726). In this trial, all patients receive postoperative whole breast irradiation. The TARGIT-E trial is a single-arm prospective study to investigate the efficacy of INTRABEAM IORT in elderly patients ($\geq$70 years old) with small breast tumours (ClinicalTrials.gov Identifier: NCT01299987). The TARGIT-C trial (ClinicalTrials.gov Identifier: NCT02290782) is a single-arm prospective study, based on the observation from the TARGIT-A trial that a single dose of IORT is non-inferior to whole breast irradiation. The study aims to measure the efficacy of IORT in a select group of patients with small breast tumours and the absence of risk factors.

While the TARGIT trials employ the INTRABEAM system to deliver IORT, there is one clinical trial studying the safety and efficacy of single dose breast IORT using the Xoft® Axxent® eBx™ System, a miniature 50 kV$_p$ x-ray source similar to the INTRABEAM. In this study (ClinicalTrials.gov Identifier: NCT01644669), a single dose of 20 Gy is delivered with the Xoft Axxent to the tumour bed following lumpectomy. The study seeks to assess the rate of local cancer recurrence at five years.

1.2 The INTRABEAM System

The INTRABEAM System is a miniature x-ray generator manufactured by Carl Zeiss Meditec AG (Jena, Germany). This device accelerates electrons from an electron gun to 50 keV, which are magnetically focused and drifted down an evacuated narrow probe tube (3.2 mm diameter, 10 cm length) to strike a thin, hemispherical gold target. The resulting 50 kV$_p$ bremsstrahlung and fluorescence photons produce a virtually isotropic dose distribution surrounding the source tip. The source output is monitored during operation by an internal radiation monitor (IRM), which measures the signal from back-scattered photons. A schematic of the INTRABEAM source (XRS) is shown in figure 1.1. The initial device (called the Photon Radiosurgery System (Photoelecton Corporation, MA, USA)) was developed in the 1990s for stereotactic interstitial radiosurgery to treat brain tumours [37]. The original device design operated at 40 kV_p, and is described in a report by Dinsmore *et al.* [38], and its dosimetry by Beatty *et al.* [39]. The original device photon spectrum and dose distribution were validated using Monte Carlo simulations by Yanch and Harte [4], and the source isotropy was investigated with ionization chamber and radiochromic film measurements by Yasuda *et al.* [40].

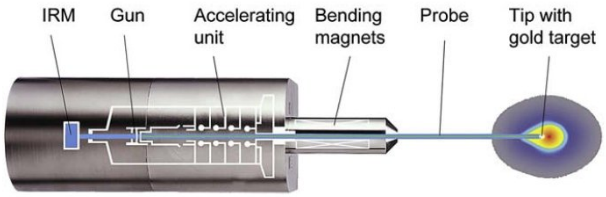

Figure 1.1 The INTRABEAM System x-ray source (XRS) and its sub-components. Image taken from [1]

1.2.1 Clinical Treatments

While the INTRABEAM was first used to treat brain tumours, the device is now used primarily for breast IORT treatments, which are performed using solid plastic (polyetherimide) spherical applicators [41]. As discussed in the preceding section, all of the TARGIT trials use the INTRABEAM to deliver breast IORT. In addition to breast treatments, the INTRABEAM has applications at various other sites in the body. Using a needle applicator, IORT can be delivered to the spine during kyphoplasty for vertebral metastases [42]. The manufacturer also offers flat and surface applicators to render the isotropic dose distribution homogeneous over a circular plane (i.e. the applicator surface) [43] for cutaneous treatments, or IORT of flat target tissues, such as rectum [44]. In the brain, the INTRAGO clinical trial [45, 46] used the INTRABEAM to deliver a single dose of IORT using a spherical applicator to the surgical margin of glioblastoma patients. A randomized phase III trial (INTRAGO-II, ClincalTrials.gov Identifier: NCT02685605) investigating the improvement in median progression-free survival with the addition of IORT to standard glioblastoma treatment (radiochemotherapy) is ongoing.

1.2.2 Issues with INTRABEAM Dosimetry

It is the goal of radiation therapy to deliver the prescribed radiation dose as accurately as reasonably achievable [47]. To ensure accurate radiation dosimetry, a calibration chain is employed where a user's radiation detector is calibrated in a way that is traceable to a so-called primary standard. Primary dosimetry standards are discussed in more detail in Chapter 2, but in general, are instruments which measure the absorbed dose from ionizing radiation without reference to an instrument measuring the same quantity. Primary standards are typically kept at national measurement institutes with the purpose of maintaining and improving primary radiation standards.

At the time of writing, no dosimetry primary standard has been established for the INTRABEAM system. In the absence of a primary standard, the INTRABEAM x-ray source is calibrated by the manufacturer. It is this manufacturer calibration dose that is used in the TARGIT protocols. The user is able to validate the manufacturer source calibration by performing independent measurements using a special water phantom and ionization chamber offered by Zeiss, along with using a recommended formula to calculate the absorbed dose to water. However, the measured water phantom dose must be "corrected" with a depth-dependent function to compare with the calibration dose data. The requirement for a depth-dependent correction function is troubling, as the absorbed dose to water by definition should be independent of the measurement technique. It is not clear if either one of these dose calculation methods (the manufacturer calibration or the recommended water phantom formula) were performed with reference to an absorbed dose standard, and which (if any) represents the physical dose to water.

1.3 Thesis Objectives

This thesis investigates the dosimetry of the INTRABEAM source, and proposes a new formalism for calculating the absorbed dose to water from the source using an ionization chamber calibrated in terms of air-kerma. The objectives of this work are the following:

1. To characterise the INTRABEAM source with a monte carlo (MC) particle transport model, to be validated with measurements performed in-air (half-value layer) and in-water (percent depth dose).

2. To evaluate the manufacturer dosimetry by deriving our own ionization chamber dose to water formalism using dose ratios calculated with the MC model.

3. To compare the absorbed dose to water as a function of distance from the source in water, measured by different methods:
    - With an ionization chamber, and calculated with either the manufacturer recommended water phantom formula, the “corrected” water phantom formula, and our formalism.
    - With radiochromic film.

1.4 Thesis Outline and Scientific Contributions

Chapter 1 introduces the treatment of breast cancer with radiation therapy, and the use of intraoperative radiation therapy as a form of accelerated partial breast irradiation. The INTRABEAM system is described, along with open questions about its dosimetry. This leads to the objectives of the thesis.

Chapter 2 provides a background in ionizing radiation dosimetry relevant to the research presented in this work, and discusses the dosimetry of the INTRABEAM system in more detail.

Chapter 3 discusses the basics of Monte Carlo (MC) particle transport simulations, and their use in radiation dosimetry calculations. The development of an MC model of the INTRABEAM source is presented. While investigating the MC calculation results, it was discovered that the inclusion of explicit $M-$ and $N-$subshell atomic transitions in the simulation had a noticeable effect on the calculated photon spectra, half-value layer, and relative dose in water which was previously unreported. These findings were published as a technical note in Medical Physics [6], and are presented in Chapter 4.

In Chapter 5, a new formalism for calculating the absorbed dose to water using an ionization chamber calibrated in terms of air-kerma is proposed, making use of MC calculated dose ratios to determine the chamber energy response and conversion of air-kerma to dose to water for the relevant photon spectra. Using the MC model described in Chapters 3 and 4, these ratios were calculated for the INTRABEAM and the formalism was applied. It was determined that the dose calculated with the manufacturer-recommended method systematically underestimates the dose to water. This chapter was published as a paper in the journal *Physics in Medicine & Biology* [48].

Chapter 6 compares the absorbed dose to water calculated with the ionization chamber formalism presented in Chapter 5 with the water phantom method recommended by the manufacturer, and the dose calculation used in the TARGIT protocol. These results were also compared with absorbed dose measurements performed with radiochromic film. It was found that the doses calculated with our formalism, the manufacturer recommended formula, and radiochromic film generally agreed to within the measurement uncertainties (5-6%). The TARGIT dose was found to underestimate the physical dose to water by 14% to 80%. This chapter was published as a paper in Medical Physics [49].

Chapter 7 is a summary and conclusion to the thesis, and proposes future research avenues.

2

Radiation Dosimetry and INTRABEAM

2.1 Preface

This chapter provides a background to the field of radiation dosimetry, and presents the reference dosimetry protocols used in radiation therapy with kilovoltage photons. The current dosimetry program of the INTRABEAM system is described. These concepts are necessary for understanding the topics presented in the later chapters.

2.2 Introduction

Radiation dosimetry is concerned with the transfer of energy from particle interactions in a material. It is from this energy transfer that the chemical and biological effects of radiation (ex: cell death) are manifest. The experimental measurement of radiation dosimetric quantities are performed with radiation detectors, which are typically calibrated with reference to a primary dosimetry standard to ensure accuracy and uniformity. In radiation therapy, dosimetry measurements are performed following a reference dosimetry protocol, or code of practice, which outlines a procedure to determine the absorbed dose at a reference point for specific conditions. The use of a reference dosimetry protocol leads to uniformity and harmonisation of all clinical dosimetry measurements following the protocol, allowing for meaningful comparisons of radiation therapy outcomes (that is, everyone agrees on what doses were delivered).

2.3 Dosimetry definitions and concepts

2.3.1 Dosimetric Quantities

As dosimetry involves quantifying the energy transferred by a field of particles to a medium, dosimetric quantities deal with the number or the energy transported by a field of particles. While particles and their interactions are themselves discrete quantities, most applications[1] in dosimetry deal with very large numbers of particles/interactions. It is valid to describe their behaviour in terms of mean or expectation value, and quantities can be approximated as continuous phenomena [50].

The fluence, Φ, is defined as the number of particles dN incident on an area da perpendicular to the particle direction,

$$\Phi = \frac{\mathrm{d}N}{\mathrm{d}a}. \tag{2.1}$$

This definition implies that the fluence is a measure of the number of particles crossing a sphere of cross-sectional area da. For particles of energy E, the related quantity of energy fluence, Ψ, is the radiant energy crossing a sphere of cross-sectional area da:

$$\Psi = E\Phi. \tag{2.2}$$

The interaction of a field of particles with a target medium is described by the interaction cross section, σ:

$$\sigma = \frac{N}{\Phi}, \tag{2.3}$$

where N is the total number of interactions. From this definition, σ has units of area (m^2) and can be thought of as the effective surface area seen by the impinging particles and is proportional to the probability for an interaction to occur. A cross section can be defined for each type of possible interaction j, σ_j, with the total cross section equal to the sum of all interaction cross sections, $\sigma = \sum \sigma_j$.

---

[1] An exception is *microdosimetry*, which deals with particle interactions at the cellular length scale.

Uncharged Particles

While the cross section is a microscopic quantity, we can define the related macroscopic quantity of an element's linear attenuation coefficient, μ:

$$\mu = \sigma \rho \frac{N_\mathrm{A}}{A} \tag{2.4}$$

where N_A is the Avogadro constant, and ρ and A are the mass density and atomic mass number of the element in question. The linear attenuation coefficient can also be expressed as the mean fraction of particles that experience an interaction while traveling a distance dl through a material,

$$\mu = \frac{1}{\mathrm{d}l} \frac{\mathrm{d}N}{N} \tag{2.5}$$

and its inverse yields the mean distance between interactions (mean free path). The material density dependence of μ is (somewhat) accounted for by diving by ρ, defining the mass attenuation coefficient, μ/ρ. From equation (2.5), it can be shown that the ratio of the number of non-interacting (N_t) to total initial particles (N_0) passing through a material of thickness t is:

$$\frac{N_t}{N_0} = e^{-\mu t}, \tag{2.6}$$

also known as the law of exponential attenuation, or Beer-Lambert law[2].

While μ/ρ deals with the number of particle interactions, the material mass energy-transfer coefficient, μ_tr/ρ, is related to the energy transferred by these interactions:

$$\frac{\mu_\mathrm{tr}}{\rho} = \frac{1}{\rho \mathrm{d}l} \frac{\mathrm{d}E_\mathrm{tr}}{E}, \tag{2.7}$$

where dE_tr is the mean energy transferred by uncharged particles of energy E into kinetic energy of charged particles.

If there are multiple types of interactions which involve energy transfer, μ_tr can be expressed as the weighted sum of the interaction linear attenuation coefficients, μ_j:

$$\mu_\mathrm{tr} = \sum_j \bar{f}_j \mu_j \tag{2.8}$$

---

[2] Specifically, the Beer-Lambert law describes the attenuation of light.

where $\bar{f}_j$ is the so-called energy-transfer function and represents the mean fraction of initial particle energy that is transferred into charged particle kinetic energy for interaction j. For photons, energy transfer is possible through photoelectic, Compton, and pair/triplet production interactions.

Once energy has been transfered to charged particles, it is possible that a fraction of this energy will then be converted in a radiative process (such as bremsstrahlung, fluorescence, or in-flight annihilation) and leave the local volume. To account for this loss of locally absorbed energy, the mass energy-absorption coefficient is defined:

$$\frac{\mu_{\mathrm{en}}}{\rho} = \frac{\mu_{\mathrm{tr}}}{\rho}(1-g) \tag{2.9}$$

where g, or the radiative fraction, is the *mean* fraction of charged particle kinetic energy lost to radiative processes. In practice, g is negligibly small for photon energies below 100 keV and for low atomic number materials, and $\frac{\mu_{\mathrm{en}}}{\rho} \approx \frac{\mu_{\mathrm{tr}}}{\rho}$ in this regime [50].

For dosimetry using air-filled ionization chambers, an important quantity is the mean energy expended in air per ion pair formed, W_{air}/e:

$$\frac{W_{\mathrm{air}}}{e} = \frac{E}{q} \tag{2.10}$$

where for a charged particle of initial energy E, a mean total charge of q will be liberated as the particle dissipates all its energy through the creation of ion pairs (e is the elementary charge, 1.6022×10^{-19} C). For an electron traversing dry air, the recommended value is $W_{\mathrm{air}}/e = 33.97 \pm 0.05$ J C^{-1} [51], however this value may not be accurate depending on the incoming electron energy. Below 10 keV, a significant fraction of the initial electron energy is lost through non-ionizing processes, and W_{air}/e begins to diverge. Furthermore, the definition of equation (2.10) does not account for the initial charged particle, which would necessarily be included in a measurement of q. ICRU Report 90 [52] defines two correction factors to calculate the effective value of W_{air}/e for monoenergetic photons,

$$\frac{W_{\mathrm{eff}}}{e} = \frac{k_{ii} k_w W_{\mathrm{air}}}{e}, \tag{2.11}$$

where k_{ii} accounts for the initial ion pair set in motion by an incident photon, and k_w uses the model of Buhr *et al.* to correct for the electron energy dependence of W_{air}/e [53]. These corrections are significant for low energy photons, and are as large as 5.5% for k_w and 6.8% for k_{ii} at 1 keV.

However, the product of $k_{ii}k_w$ yields some cancellation, with the combined correction being less than 2%.

An early dosimetric quantity specific to photon interactions in air is exposure, X:

$$X = \frac{\mathrm{d}q}{\mathrm{d}m} \tag{2.12}$$

where dq is the mean total charge liberated after initial photon interaction in a mass dm of dry air, with units of C kg^{-1}[3].

The concept of exposure has ostensibly been superseded by the more general quantity of kerma (kinetic energy released per unit mass), K:

$$K = \frac{\mathrm{d}E_{\mathrm{tr}}}{\mathrm{d}m} \tag{2.13}$$

where dE_{tr} is the mean value of energy transferred to charged particles by incident uncharged particles in a mass dm of the material in question. Kerma is measured in gray (Gy), which in SI units is J kg^{-1}. From the definition of mass energy-transfer coefficient (Eq.(2.7)), it can be shown that for polyenergetic photons, the kerma in a medium is

$$K_{\mathrm{med}} = \int_0^{E_{\max}} \Psi_{\mathrm{med}}(E) \left[\frac{\mu_{\mathrm{tr}}(E)}{\rho}\right]_{\mathrm{med}} \mathrm{d}E. \tag{2.14}$$

It is a convention to identify the kerma in a given medium by the nomenclature "medium-kerma", thus the kerma calculated in a volume of air is often referred to as air-kerma. This can be further specified by also identifying the medium in which the photon energy spectrum $\Psi_{\mathrm{med}}(E)$ is obtained by adding the qualifier "in medium". In this way, the kerma measured in a volume of air from a photon beam free in air would be the air-kerma in air, while one could also determine the kerma to an air volume inside a surrounding volume of water (i.e., using the energy spectrum in water) to get the air-kerma in water [54].

Similar to the discussion of mass energy-absorption coefficient (Eq.(2.9)), the component of kerma which only includes local energy deposition (the collisional, or electronic kerma) can be calculated as:

$$(K_{\mathrm{el}})_{\mathrm{med}} = \int_0^{E_{\max}} \Psi_{\mathrm{med}}(E) \left[\frac{\mu_{\mathrm{en}}(E)}{\rho}\right]_{\mathrm{med}} \mathrm{d}E, \tag{2.15}$$

---

[3] Historically, exposure was measured in roentgen, where 1 R = 2.58×10^{-4} C kg^{-1}.

and it follows that $K_{\mathrm{el}} = (1-g)K$. From Eqs.(2.10) and (2.12), the relationship between exposure and electronic air-kerma is:

$$X = (K_{\mathrm{el}})_{\mathrm{air}} \left(\frac{e}{W_{\mathrm{air}}} \right). \tag{2.16}$$

Charged Particles

In principle, the attenuation coefficient concept can be applied to both charged and uncharged particles, however, charged particle interactions occur much more frequently and in a higher density than uncharged particles, and are typically described by their energy loss ($\mathrm{d}E$) per unit length ($\mathrm{d}l$), or *stopping power*:

$$S = \frac{\mathrm{d}E}{\mathrm{d}l}. \tag{2.17}$$

Similar to the mass attenuation coefficient, the density dependence of a material's stopping power is largely removed[4] by defining the mass stopping power, S/ρ. The stopping power can be expressed as components defined by the type of interaction: ionization or excitation of atomic electrons (mass electronic stopping power S_{el}), bremsstrahlung emission in the electric field of atomic nuclei or electrons (mass radiative stopping power S_{rad}), and elastic Coulomb interactions with atomic nuclei (mass nuclear stopping power S_{nuc}). The mass stopping power is the linear combination of these components,

$$\frac{S}{\rho} = \frac{1}{\rho}(S_{\mathrm{el}} + S_{\mathrm{rad}} + S_{\mathrm{nuc}}). \tag{2.18}$$

The mass radiative stopping power is proportional to Z^2/A, where Z is the medium atomic number, and proportional to the charged particle energy E (for $E \gg m_e c^2$), and thus becomes more significant in materials with large Z and at high energies. The ratio of S_{rad} to S_{el} can be approximated by

$$\frac{S_{\mathrm{rad}}}{S_{\mathrm{el}}} \approx \frac{EZ}{700 \pm 100\ \mathrm{MeV}} \tag{2.19}$$

and the energy at which $S_{\mathrm{rad}} = S_{\mathrm{el}}$ is known as the *critical energy*. For electrons, the energy transfer with nuclei is negligible, and S_{nuc} is usually ignored.

The distance a charged particle travels in a medium along its path before stopping is known as its *range*. If the charged particle energy loss is assumed to be continuous along its path, the

---

[4] A residual dependence on material density still persists in the mass stopping power formulation, known as the *density effect*.

continuous-slowing-down range, or CSDA range R_{CSDA}, can be calculated from Eq.(2.17) by

$$R_{\text{CSDA}} = \rho \int_0^{E_0} \frac{\mathrm{d}E}{S(E)}. \tag{2.20}$$

where $S(E)$ represents the total linear stopping power. The formulation of the CSDA assumes that as a charged particle slows down (i.e. loses energy) as it traverses a medium, it produces secondary particles through the interactions listed in Eq.(2.18) which are part of an overall continuous energy loss. Electrons generated from these interactions are known as *secondary electrons*, and those with sufficient kinetic energy (termed *knock-on electrons* or δ rays) can then undergo their own Coulomb interactions, transferring their energy along a separate path distinct from the primary charged particle. Due to scattering, the CSDA is often less than the depth of maximum penetration into a material.

In dosimetry, it is of interest to calculate the energy deposition which remains in the volume of interest, that is the *local* energy. A concept related to local energy deposition is the *restricted stopping power*, $S(E,\Delta)$, which is a formulation of the stopping power but only considering charged particle energy losses below a threshold energy Δ. Here, Δ is related to the dimension of the volume of interest and the charged particle range at that energy. The restricted stopping power can be defined both for electronic (collisional) energy loss as well as for radiative energy loss, i.e., restricted electronic or restricted radiative stopping powers. A similar but non-identical quantity to restricted stopping power is the *linear energy transfer*, or LET $L_\Delta(E)$, which excludes only losses to kinetic energy above Δ while still containing the binding energy for all interactions [50].

While kerma deals with the energy transferred by uncharged particles to charged particles in a volume, a related quantity is that of absorbed dose, D, which is concerned with the mean energy *imparted* to a volume. Here, mean imparted energy is the difference between the mean particle energy entering ($\bar{E}_{\text{in}}$) and leaving ($\bar{E}_{\text{out}}$) a volume, including all changes in mean rest energy ($\sum Q$) in the volume:

$$\bar{\varepsilon} = \bar{E}_{\text{in}} - \bar{E}_{\text{out}} + \sum Q. \tag{2.21}$$

The absorbed dose to a mass dm is then:

$$D = \frac{\mathrm{d}\bar{\varepsilon}}{\mathrm{d}m} \tag{2.22}$$

with the same units as kerma, namely Gy. Pragmatically, the absorbed dose is then a measure of the energy lost by charged particles along their tracks across a volume. In the condition where the energy from all charged particles entering a volume is the same as from all leaving (charged particle equilibrium, or CPE), the absorbed dose is equal to the electronic kerma:

$$D = K_{\mathrm{el}}. \tag{2.23}$$

2.3.2 Radiation Quality

In an ideal situation, one would have knowledge of all particle types, energies, and directions when describing a radiation field. Such information is available when performing a Monte Carlo simulation of particle transport, however in reality this is not feasible. As most radiation dosimetry quantities depend on particle energy, knowledge of only the energy fluence spectrum for a radiation field is generally sufficient for dosimetric calculations. While energy fluence spectra can be measured or calculated by Monte Carlo methods, the equipment and time necessary to acquire them are not practical in a clinical setting[5]. Because of this, clinical radiation fields are typically characterised by a relatively straightforward measurement known as a *beam quality specifier*. The metric used for beam quality specification depends on the particle type (ex: photons, electrons, heavy charged particles), and energy regime.

For kilovoltage x-ray beams ($<$300 keV), the incident energy spectrum is correlated with the amount of attenuation through a given amount of material. This attenuation is quantified as a beam quality specifier by the *half-value layer* (HVL), which is defined as the thickness of material (typically aluminum or copper) required to reduce the air-kerma rate by a factor of two. It is recommended for the measurement of HVL to use an ionization chamber detector with relatively constant energy dependence of the air kerma detector response, i.e., energy dependence of the ratio q/K_{air} over the energy range concerned, and to be performed under scatter-free and narrow beam conditions [54]. A related quantity to the HVL is the *effective energy*, which is defined as the energy of a monoenergetic photon which has the same HVL as the x-ray spectrum in question. The effective energy can be derived from the HVL through the relationship

$$\left(\frac{\mu}{\rho}\right)_{\mathrm{eff}} = \frac{\ln 2}{\rho\ \mathrm{HVL}} \tag{2.24}$$

where $(\mu/\rho)_{\mathrm{eff}}$ is the effective mass attenuation coefficient for the beam, in the medium used as the attenuator. By interpolating μ/ρ data for the given attenuator material, the effective energy corresponding to $(\mu/\rho)_{\mathrm{eff}}$ (and hence to the HVL) can be obtained.

---

[5] Treatment planning dose calculations and quality assurance verification calculations are examples of clinically deployed MC methods

While HVL is the conventional beam quality specifier for kilovoltage x-ray beams, it is not without limitations. The HVL is not a unique specifier in that different energy fluence spectra can yield the same HVL. As well, HVL is not directly related to the absorbed dose to water, which is the quantity of interest in most dosimetry protocols. The use of additional information, such as the tube potential or second HVL (thickness of material required to attenuate air-kerma rate from 50% to 25%) in conjunction with the HVL has been shown to reduce the uncertainties in certain factors used in kilovoltage dosimetry protocols [54, 55]. Other proposed kilovoltage beam quality specifiers include the ratio of absorbed doses at two different depths in water. It has been reported that the ratio of doses at 2 and 5 cm depth in water correlates well with the ratio of mass energy absorption coefficients of water to air at 2 cm depth [56]. The ratio of doses at two depths has also been shown to have a strong linear correlation with the beam quality correction factor $k_{\mathrm{Q,Q_0}}$ [57] used in the TRS-398 dosimetry protocol [55]. Despite this, the HVL remains the most common beam quality specifier for kV photon beams.

2.4 Radiation Detectors

2.4.1 Detector Response and Calibration

A radiation detector is a device which is able to measure a physical quantity (i.e. charge, temperature, etc.), from which a dosimetric quantity can be derived. Most radiation detectors are concerned with the measurement of kerma or absorbed dose, and are also known as *dosimeters*. Generally, a dosimeter will provide a signal M which is related to the mean absorbed dose deposited in its radiation sensitive volume. The detector *response* for a generic quantity, G, irradiated by a beam quality Q is defined as:

$$R_Q = \frac{M_Q}{G_Q} \tag{2.25}$$

and the inverse of the detector response is the *detector calibration coefficient*:

$$N_{G,Q} = \frac{1}{R_Q} = \frac{G_Q}{M_Q}. \tag{2.26}$$

In the metrological chain for ionizing radiation, the detector calibration coefficient is determined using a primary standard instrument at a standards laboratory under well established reference conditions. The user can then determine the quantity of interest at their facility by performing measurements with their calibrated detector using one of the reference dosimetry codes of practice discussed in sections 2.5.3 and 2.5.4.

2.4.2 Desirable Properties of Dosimeters

As mentioned, a dosimeter must provide a signal M which is related to the mean absorbed dose deposited in its radiation sensitive volume. There are several desirable characteristics which dosimeters should possess to be considered suitable for radiation dosimetry measurements.

Reproducibility: The reproducibility, or precision, of a dosimeter refers to the influence of random errors in performing the dosimetric measurement. The instrument reproducibility can be estimated by the standard deviation of a sample of repeated measurements.

Linearity: An ideal dosimeter would yield a signal M which is linearly proportional to the absorbed dose to the detector radiation sensitive volume. Most practical dosimeters are linear within a given dose range, but may experience non-linear behaviour beyond this range (ex: saturation at high doses).

Dose Range: The useful dose range of a dosimeter refers to the lower and upper dose limits between which the dosimeter response is sufficient enough to yield reproducible measurements. A dosimeter is suitable for dose measurements if they fall within its dose range.

Dose-Rate Dependence: A dosimeter reporting the time-integrated dose (i.e., cumulative dose during irradiation, not dose-rate) should be independent of the rate the dose is delivered. Conversely, a dosimeter reporting the dose-rate should yield a signal proportional to the delivered dose-rate (or a single-valued function of it) [50].

Stability: A dosimeter should be stable with time in regards to its characteristics, both prior to use (“shelf-life”), and post irradiation.

Energy Dependence: The energy dependence of a dosimeter refers to the dependence of its response R_Q to the spectral distribution, or beam quality Q, of the radiation used. The overall dosimeter energy dependence can be broken into its intrinsic energy dependence, or often called LET dependence (relation between signal M_Q and dose to detector sensitive volume $D_{\text{det},Q}$ as function of Q) and its dosimetric (i.e. air-kerma or absorbed dose) energy dependence, that is the relation between the dose to the medium of interest $D_{\text{med},Q}$ and dose to the detector $D_{\text{det},Q}$ as function of Q. It is desirable for a dosimeter to be energy independent across the relevant energy regime for measurement, and for its energy dependence to be well understood.

Directional Dependence: Depending on the geometry and construction, dosimeter response can be dependent on the direction of the incident radiation, and may not be suitable for use in certain orientations.

Spatial Resolution and Size Effects: The spatial resolution of a dosimeter is largely determined by the dimensions of its sensitive volume. In regions with large dose variations over the region of the detector, volume averaging effects will be present in the dosimeter sensitive volume.

2.4.3 Various Types of Dosimeters

Radiation dosimeters are used in a wide variety of applications and fields, such as physics, medicine, and industry, and in the measurement of a huge range of absorbed doses ($\sim \mu$Gy in environmental dosimetry to GGy in industrial materials modification). As such, there are many different types of dosimeter technologies available. Briefly, these detector classes are: calorimeters (measure dose through radiation-induced temperature increase), ionization chambers (measure dose through collection of radiation-induced ion-pairs), chemical detectors (measure dose through radiation-induced chemical reactions), and solid-state detectors (measure dose through radiation-induced ionization, detected either electronically or via light output). The work in this thesis primarily made use of two different dosimeters, that of air-filled ionization chambers and radiochromic film (a type of chemical detector). They are discussed in more detail below.

2.4.4 Ionization Chambers

The most commonly used dosimeter is the ionization chamber [50]. In this technology, radiation interacts with the sensitive volume of the chamber and produces ion pairs which are drawn by an applied electric field to a collecting electrode. This signal is measured with an electrometer as electrical charge or current. Designs of ionization chambers can be categorised as one of four types: Free air chambers (used by primary standards laboratories for the measurement of air-kerma, and are discussed in section (2.5.1)), cavity chambers, parallel-plate chambers, and transmission chambers. Transmission chambers are typically a special type of parallel-plate chamber with thin entrance and exit windows, and are used for monitoring changes in radiation beam output as a function of time.

Cavity Chambers

A cavity chamber consists of a wall material surrounding an air-filled cavity containing a collecting electrode. The geometry of the wall and cavity are typically one of three shapes: spherical, cylindrical, or thimble (cylinder with a hemispherical top). A polarizing potential of 200 V to 400 V is applied across the chamber wall to the electrode through connection with an electrometer, which also reads the signal from the electrode. Upon irradiation by a beam of ionizing radiation, interactions will occur in the air cavity producing electric charge (creation of ion pairs). The electric field causes mobility of the liberated charges and generates a measured current, which is proportional to the dose-rate.

The appropriate thickness of the chamber wall is determined by the application. For use in a photon beam free in air, the chamber wall should be thick enough to set up CPE across the cavity. When measurements are made in a solid or liquid phantom, the wall should either be thin enough to minimize any fluence perturbation, or thick enough to re-establish partial charged particle equilibrium in the wall itself. The wall material is often graphite or a plastic designed to be either air-equivalent or water-equivalent. Here, equivalence refers to having similar mean mass electron stopping powers (for charged particle beams) and mean mass-energy absorption coefficients (for photons beams) as air or water for the given particle energy spectrum at the point of interest.

Parallel-Plate Chambers

Parallel-plate chambers are comprised of two plane-parallel surfaces (an entrance window and collector) with a surrounding body creating a cylindrical air cavity. Most designs of parallel-plate chambers include a guard ring, which surrounds the collector radially. A polarizing potential is applied to the entrance window, while the guard is kept at ground and collector at virtual ground. The presence of a guard ring establishes a well-defined electric field in the collecting region, and the chamber can then be treated as an ideal parallel-plate capacitor. Parallel-plate chambers typically have a thin entrance window ($\sim$ mg cm^{-2}) which makes them ideal for x-ray beams below 70 kV$_p$, where the attenuation through a thicker cavity chamber wall significantly affects the photon energy spectrum [50]. The body of a soft x-ray parallel-plate chamber is designed to act as a small scattering phantom, which aids in reducing the chamber energy dependence. The collecting thickness (i.e. separation between entrance window and collector) can be made quite small ($\sim$ mm), yielding good spatial resolution for depth-dose distributions. The two ionization chambers used predominantly in this thesis (PTW 23342 and PTW 34013) are parallel-plate.

Chamber Influence Quantities

A chamber influence quantity is a parameter which can affect the measured signal of an ionization chamber under irradiation at a constant dose-rate. These quantities are well understood, and can be corrected for.

Air Temperature and Pressure: For air-filled ionization chambers open to the atmosphere, the response of the chamber is dependent on the mass of air in the cavity, and thus the ambient air conditions. The value of the chamber calibration coefficient was determined at a reference temperature (T_{ref}) and pressure (P_{ref}). Measurements made at a different temperature and pressure must be corrected back to the reference conditions by treating the cavity air as an ideal gas:

$$p_{\text{TP}} = \frac{P_{\text{ref}}}{P} \frac{(T(^{\circ}C) + 273.15)}{(T_{\text{ref}}(^{\circ}C) + 273.15)} \tag{2.27}$$

Air humidity also has a small effect on the ionization current in air, which may need to be accounted for in certain situations. As a general rule, a chamber air humidity correction is not necessary if the relative humidity is above 10% (assuming the chamber calibration coefficient is given for a relative humidity of 50%).

Polarity Effect: The polarity of the potential present in an ionization chamber (positive or negative) can affect the measured signal for a variety of reasons, such as: a small potential difference between the collector and guard in a parallel-plate chamber, excess current due to electrons ejected from the collector in a parallel-plate chamber, low-energy electrons emitted from asymmetric electrodes, and extra-cameral current (i.e., produced outside of the cavity, such as insulator leakage or cables). The correction for this effect is:

$$p_{\text{pol}} = \left| \frac{M^{+} - M^{-}}{2M} \right|, \tag{2.28}$$

where M^{+} and M^{-} are the readings at positive and negative bias, and the denominator M is the reading at the bias used for reference measurements (i.e. during chamber calibration).

Ion Recombination Effect: After air ionization in the cavity, some of ions may recombine with oppositely charged ions as they travel to/away from the collection electrode, and are thus not accounted for in the measurement signal. Extensive work has been done to model and estimate the true number of ions formed [58]. One method for estimating the ion recombination correction is by performing measurements at two different bias voltages. For a continuous radiation beam, the correction is:

$$p_{\text{ion}} = \frac{1-(V_H/V_L)^2}{M_H/M_L-(V_H/V_L)^2}, \tag{2.29}$$

where M_H is the signal from the chamber at normal operation voltage V_H, and M_L is the signal at voltage V_L ($V_L/V_H \leq 0.5$).

2.4.5 Radiochromic Film

Radiochromic film (known by its trade name Gafchromic$^{\text{TM}}$ film (Ashland, NJ)) is a chemical dosimeter, where radiation-induced polymerization of diacetylene molecules present in the film's active layer creates a visible change of the film optical properties (i.e., colour change), which is proportional to the absorbed dose. Unlike silver halide radiographic films which require chemical processing, the polymerization in radiochromic films does not require any developing, and the colour change is immediately visible to the naked eye upon exposure to radiation. Gafchromic film is available in a number of different models, which are sensitive over a dose range relevant to their application. EBT models (EBT2, EBT3, and EBT-XD) are designed for radiation therapy doses (0.01–40 Gy), XR-QA2 for diagnostic radiology (0.1–20 cGy), and MD-V3 and HD-V2 for high dose measurements (up to 100 Gy). In general, these models all feature an active layer containing diacetylene monomers incorporated into a gelatin matrix, sandwiched (or coated) onto a polyester base. The relatively small size of the induced diacetylene chromophore polymers enables excellent 2D spatial resolution (up to 1200 line pairs/mm) [59].

The response of radiochromic film to dose is quantified by the net optical density (netOD), which is defined as:

$$\text{netOD} = \log \frac{M_{\text{pre}}}{M_{\text{post}}} \tag{2.30}$$

where M_{pre} and M_{post} are the signal from a light transmission[6] measurement through the film pre- and post- irradiation. The most commonly used optical densitometers for measuring radiochromic film optical transmission are flat-bed document scanners [60]. Before use as a dosimeter, radiochromic film must be calibrated by determining the response, i.e th relationship between film netOD and absorbed dose for entire dose range. This response curve is unique for the film dosimetry system used, including the model of film, film scanner, film dosimetry protocol, and potentially even film batch number [50].

Film calibration is performed by first determining the absorbed dose output at a reference point from a radiation beam using an appropriate dosimetry formalism/code of practice (see

---

[6] In some cases, light reflection is used as the signal.

section 2.5.3). Once the radiation source output is known, a sample of films from the same batch are then irradiated at the same reference point, covering the appropriate dose range. The known delivered dose to the films is plotted as a function of the measured film netOD, generating the the film calibration curve. By fitting a functional form to this curve, the netOD from a subsequent film irradiation can be converted to a measured dose. One such functional form appropriate to radiochromic film dosimetry is the non-linear type:

$$D = a \cdot \text{netOD} + b \cdot (\text{netOD})^n \tag{2.31}$$

where a, b and n are fitting parameters.

The EBT model of Gafchromic film has been shown to be relatively energy independent for photon beams ranging from MV to a few hundred keV [61]. However, the energy dependence below this range could be quite large, with up to a 30% decrease in response at 25 keV compared to 4 MV [62]. This energy-dependent response at low photon energies is in part due to the presence of high-Z materials in the active layer, which leads to a signal enhancement from photoelectric interactions. The EBT2 model showed an improved energy dependence over the first-generation EBT, with energy response variations of up to 6.5% over 50 kV_p to 10 MV photon beams (compared to 7.7% for EBT over the same energy range) [63]. Bekerat *et al.* investigated the energy response of the third-generation of EBT films, EBT3, and found that by adding aluminium to the active layer, the energy response could be almost made energy independent down to 20 keV [64]. The most recent formulations of EBT3 film include aluminium, and have been shown to corroborate the energy independence predicted by Bekerat *et al.* [65, 66].

2.4.6 Cavity Theory

The experimental measurement of absorbed dose is performed using a radiation detector, or dosimeter, which yields a signal which is proportional to the mean absorbed dose in the detector's sensitive volume[7] (D_{det}). Cavity theory seeks to solve the general problem of relating D_{det} to the absorbed dose at a point in the medium of interest (D_{med}) by a proportionality factor f_Q,

$$D_{\text{med}} = f_Q D_{\text{det}} \tag{2.32}$$

---

[7] For an air-filled ionization chamber, this volume is the air *cavity*. The term "cavity" is often applied generically to the sensitive volume of other detector technologies.

where Q refers to the particular radiation quality. Cavity theory can give quasi-exact analytical solutions for f_Q in two situations; when the cavity is *small* or *large* compared to the range of secondary electrons.

A special case where cavity theory is not necessary is if the detector has been calibrated in the same conditions in which the measurements are being performed (i.e., identical radiation quality, field size, position in medium). The dose to the medium is then:

$$D_{\mathrm{med},Q_0} = M_{\mathrm{det}} N_{D,\mathrm{med},Q_0} \tag{2.33}$$

where M_{det} is the detector signal and N_{D,med,Q_0} is the detector calibration coefficient at radiation quality Q_0. Here, N_{D,med,Q_0} effectively includes f_{Q_0} in its determination. A method such as cavity theory would be required to modify Eq.(2.33) to calculate D_{med} in a beam quality other than Q_0.

Small Cavity: Bragg-Gray and Spencer-Attix

A cavity is considered "small" if the range of secondary electrons[8] for the relevant beam quality is greater than the cavity dimensions. It then follows that the vast majority of electrons crossing the cavity would originate from the surrounding medium and not in the cavity itself, and that the electron fluence would be negligibly perturbed by the presence of the cavity. A cavity satisfying these conditions is said to be a *Bragg-Gray cavity*, and the mean dose in a Bragg-Gray cavity is proportional to the dose in the medium by the ratio of unrestricted electron mass electronic stopping-powers (S_{el}/ρ) for the medium and the detector cavity materials:

$$D_{\mathrm{med}} = \frac{[S_{\mathrm{el}}/\rho]_{\mathrm{med}}}{[S_{\mathrm{el}}/\rho]_{\mathrm{det}}} D_{\mathrm{det}}. \tag{2.34}$$

For a continuous secondary electron spectra, the dose to a Bragg-Gray cavity becomes

$$D_{\mathrm{det}} = \int_0^{E_{\mathrm{max}}} [\Phi_E^{\mathrm{sec}}][S_{\mathrm{el}}(E)/\rho]_{\mathrm{det}} \mathrm{d}E, \tag{2.35}$$

where Φ_E^{sec} is the secondary electron fluence (not including δ rays and their progeny). The dose to the surrounding medium can be found in a similar way:

$$D_{\mathrm{med}} = \int_0^{E_{\mathrm{max}}} [\Phi_E^{\mathrm{sec}}][S_{\mathrm{el}}(E)/\rho]_{\mathrm{med}} \mathrm{d}E. \tag{2.36}$$

---

[8] In principle, cavity theory applies to any type of charged particle provided the underlying assumptions are valid. For clinical photon and electron beams, we are only concerned with the dose deposited by electrons.

The equality in Eq.(2.34) holds using the integral forms of Eqs.(2.35) and (2.36) by assuming that the electron fluence is identical both in the detector and the medium. The formulation of the above Bragg-Gray equations implicitly assumes that the energy deposition in the cavity by any δ rays generated in the medium is exactly balanced by energy deposited in the medium by δ rays produced in the cavity, or so-called δ ray equilibrium.

Spencer and Attix [67] modified Bragg-Gray cavity theory by removing the assumption of δ ray equilibrium. In their formulation, they explicitly accounted for energy deposition of energetic δ rays and introduced a cut-off energy Δ which was related to the cavity dimension. Electrons with energies less than Δ were assumed to be local and deposited all their energy either inside the cavity or outside of it. For an air-filled ionization chamber cavity, $\Delta \sim 10$ keV to 15 keV. Spencer-Attix theory also considered the total electron fluence incident on the cavity from secondary electrons and higher order generations (i.e.δ rays and their progeny). For a continuous electron spectra, the Spencer-Attix cavity dose is:

$$D_{\text{det}} = \int_{\Delta}^{E_{\max}} [\Phi_E^{\text{tot}}]_{\text{med}} [L_{\Delta}(E)/\rho]_{\text{det}} \mathrm{d}E \tag{2.37}$$

where Φ_E^{tot} is the total electron fluence and $L_{\Delta}(E)/\rho$ is the mass LET of the detector cavity material.

The Spencer-Attix theory was further modified by Nahum [68], who proposed an additional term to account for the energy deposited by electrons slowing down below an energy of Δ (so-called *track ends*). The Spencer-Attix cavity dose with track end correction is then:

$$D_{\text{det}} = \int_{\Delta}^{E_{\max}} [\Phi_E^{\text{tot}}]_{\text{med}} [L_{\Delta}(E)/\rho]_{\text{det}} \mathrm{d}E + [\Phi_E^{\text{tot}}(\Delta)]_{\text{med}} [S_{\text{el}}(\Delta)/\rho]_{\text{det}} \Delta \tag{2.38}$$

where $[\Phi_E^{\text{tot}}(\Delta)]_{\text{med}} [S_{\text{el}}(\Delta)/\rho]_{\text{det}} \Delta$ estimates the dose due to electrons slowing down below energy Δ.

The factor f_Q for Spencer-Attix cavity theory can be determined from the dose ratio in the medium to that in the detector cavity material,

$$\begin{aligned} \frac{D_{\text{med}}}{D_{\text{det}}} &= \frac{\int_{\Delta}^{E_{\max}} [\Phi_E^{\text{tot}}]_{\text{med}} [L_{\Delta}(E)/\rho]_{\text{med}} \mathrm{d}E + [\Phi_E^{\text{tot}}(\Delta)]_{\text{med}} [S_{\text{el}}(\Delta)/\rho]_{\text{med}} \Delta}{\int_{\Delta}^{E_{\max}} [\Phi_E^{\text{tot}}]_{\text{med}} [L_{\Delta}(E)/\rho]_{\text{det}} \mathrm{d}E + [\Phi_E^{\text{tot}}(\Delta)]_{\text{med}} [S_{\text{el}}(\Delta)/\rho]_{\text{det}} \Delta} && (2.39) \\ &= \left(\frac{\bar{L}_{\Delta}}{\rho}\right)_{\text{det}}^{\text{med}} && (2.40) \end{aligned}$$

Large Cavity

A cavity is considered "large" when its dimensions are much greater than the ranges of secondary electrons. Large cavity theory is only relevant for photon beams. In this geometry, most secondary electrons are liberated by photon interactions in the detector material. In a state of CPE, the dose to the detector is

$$D_{\text{det}} = \Psi_{\text{det}} \left(\frac{\mu_{\text{en}}}{\rho} \right)_{\text{det}} \tag{2.41}$$

recalling the CPE equivalence of dose and electronic kerma from Eq.(2.23). However, due to photon attenuation only partial CPE is possible, modifying Eq.(2.41) with a factor β_{det}, defined to be the ratio of absorbed dose to electronic kerma in the detector:

$$D_{\text{det}} = \beta_{\text{det}} \Psi_{\text{det}} \left(\frac{\mu_{\text{en}}}{\rho} \right)_{\text{det}}. \tag{2.42}$$

Similarly, the dose to the medium can be calculated just as in Eq.(2.42). The ratio of dose in the undisturbed medium to the detector is:

$$\frac{D_{\text{med}}}{D_{\text{det}}} = \left(\frac{\beta_{\text{med}}}{\beta_{\text{det}}} \right) \frac{\Psi_{\text{med}} (\mu_{\text{en}}/\rho)_{\text{med}}}{\Psi_{\text{det}} (\mu_{\text{en}}/\rho)_{\text{det}}} \tag{2.43}$$

It is assumed that $\beta_{\text{det}} \approx \beta_{\text{med}}$, and that the photon energy fluence in negligibly perturbed by the detector ($\Psi_{\text{det}} \approx \Psi_{\text{med}}$). For a continuous photon energy spectra, this gives the large cavity relationship:

$$\begin{aligned} D_{\text{med}} &= \frac{\int_0^{E_{\text{max}}} \Psi_{\text{med}}(E) (\mu_{\text{en}}(E)/\rho)_{\text{med}} \mathrm{d}E}{\int_0^{E_{\text{max}}} \Psi_{\text{med}}(E) (\mu_{\text{en}}(E)/\rho)_{\text{det}} \mathrm{d}E} D_{\text{det}} && (2.44) \\ &= \left(\frac{\bar{\mu}_{\text{en}}}{\rho} \right)^{\text{med}}_{\text{det}} D_{\text{det}}. && (2.45) \end{aligned}$$

Historically, air-filled ionization chambers were calibrated in terms of exposure. Under the assumptions of the large cavity limit and recalling Eq.(2.16), the relationship between absorbed dose and exposure is:

$$\begin{aligned} D_{\text{med}} &= \left(\frac{W_{\text{air}}}{e} \right) \left(\frac{\bar{\mu}_{\text{en}}}{\rho} \right)^{\text{med}}_{\text{air}} X && (2.46) \\ &= fX && (2.47) \end{aligned}$$

where the so-called f-factor converts exposure to absorbed dose to the given medium.

Intermediate Cavity: Burlin

For photon beams, there exists an intermediate class of cavities which satisfy neither the Bragg-Gray conditions or large cavity limit. The general cavity theory of Burlin approaches this issue phenomenologically by defining a weighting factor ω_{BG} to calculate the ratio of dose to the detector and medium:

$$\frac{D_{\mathrm{det}}}{D_{\mathrm{med}}} = \omega_{\mathrm{BG}} \left(\frac{\bar{L}_{\Delta}}{\rho} \right)_{\mathrm{med}}^{\mathrm{det}} + (1 - \omega_{\mathrm{BG}}) \left(\frac{\bar{\mu}_{\mathrm{en}}}{\rho} \right)_{\mathrm{med}}^{\mathrm{det}} \tag{2.48}$$

where it can be seen that $\omega_{\mathrm{BG}} \approx 1$ corresponds to a Bragg-Gray cavity, and $\omega_{\mathrm{BG}} \approx 0$ represents a large cavity [69]. The Burlin theory has been criticised for being too simplistic and requiring restrictive approximations, and is not used in practice [70].

Practical detector cavities

In reality, very few radiation detectors are a perfect Bragg-Gray or large photon detector cavity, but deviate only slightly from the given cavity theory conditions. One approach for these detectors is to account for the deviation with multiplicative perturbation correction factors p_i, which can originate from different effects (i.e. presence of ionization chamber wall, change in electron fluence due to cavity, etc.). For an air-filled ionization chamber approximating a Bragg-Gray cavity, the dose to medium from Spencer-Attix theory would then be

$$D_{\mathrm{med}} = D_{\mathrm{air}} \left(\frac{\bar{L}_{\Delta}}{\rho} \right)_{\mathrm{air}}^{\mathrm{med}} \prod_i p_i \tag{2.49}$$

where is it assumed that p_i are close to unity and are independent of each other[9].

None of the above: direct determination of f_Q

While the goal of cavity theory is to find the dose ratio f_Q of Eq.(2.32), it is not the only means. It is possible to determine f_Q directly through measurement (such as the example of Eq.(2.33)) or by Monte Carlo simulation [71]. The direct determination of f_Q has the advantage of not requiring

---

[9] In reality, the p_i are related to the electron and photon fluence and thus are not independent. The reader is directed to Section 15.6 in Ref. [50] for a thorough treatment of the subject.

any of the assumptions (or perturbations) implicit in cavity theory, in particular for intermediate cavities [72]. The Monte Carlo approach has only become feasible in recent times thanks to advances in computer processing power and the development of accurate and versatile Monte Carlo particle transport codes.

2.5 Kilovoltage X-ray Beam Reference Dosimetry

2.5.1 Primary standards for kV x-ray beams

A primary measurement standard refers to an instrument which is able to determine a physical quantity of interest to a high degree of accuracy and precision, without needing to refer to another instrument which measures the same quantity. For kilovoltage photon beams (few keV to few hundred keV), the primary standard for the measurement of air-kerma is the free-air ionization chamber (FAC). FACs are designed to be sufficiently large such that the incident photons and liberated charged particles only interact in air; the walls of the chamber do not influence the measurement. This requirement means that the dimensions of the FAC must be greater than the range of secondary electrons, limiting their practical use to x-ray beams below 300 kV [50]. For the measurement of low dose rate kV photon sources (such as those used in brachytherapy), a primary standard exists using a wide-angle free-air ionization chamber (WAFAC) [73]. Compared to a traditional FAC, the WAFAC has a wider acceptance angle and large collecting volume, allowing for greater sensitivity. There has been some development for an absorbed dose to water primary standard for use with kilovoltage photons using water calorimetry [74–77].

2.5.2 Primary Standards for Miniature X-ray Sources

Miniature x-ray sources, such as the Zeiss INTRABEAM and Xoft Axxent, are a relatively new class of low dose rate kV photon-emitting devices. As such, the development of primary standards for these devices is relatively recent, and in the case of the INTRABEAM, still ongoing. In 2014, a primary standard reporting the reference air-kerma rate for the Xoft Axxent was established at the National Institute of Standards and Technology (NIST, USA) [78]. This standard measures the air-kerma rate at 50 cm, in air, without conversion to *in vacuo* conditions. The decision to report air-kerma in air rather than *in vacuo* was made as it was found that the corrections for attenuation and scattering could be as large as 25% for the Axxent [79], compounded with additional uncertainties due to source-to-source variations [80]. Because of this, the assumption of perfect inverse-square law behaviour does not apply and thus air-kerma strength is not relevant. In principle, the NIST air-kerma rate standard could be developed for the INTRABEAM or other miniature x-ray sources.

In 2012, the German (PTB) and Czech Republic (CMI) national metrology labs embarked on a joint project through the European Metrology Research Programme (EMRP) to develop a suitable absorbed dose standard for miniature x-ray sources [81]. A prototype was built based on the current primary standard at PTB for I-125 brachytherapy sources. This standard uses an extrapolation ionization chamber in a phantom of water-equivalent material (GROVEX II) to measured the absorbed dose to water [82]. However, it was found that the phantom material (RW1) was not suitable for the low energy photon spectra of miniature x-rays due to induced fluorescence [83]. Subsequent work has been done on this project [84], however as of writing a primary standard has not yet been established. As such, a primary standard does not yet exist for the INTRABEAM source.

2.5.3 kV Dosimetry Protocols: Air-Kerma Calibration

In kilovoltage x-ray beams, air-filled ionization chambers do not behave as a Bragg-Gray cavity, with up to 30% of the air ionizations being produced by photon interactions in the air cavity [85]. As well, the ranges of secondary electrons produced by kV photons are very small (<1 mm in water), meaning that virtually all electrons liberated in the surrounding medium are unable to penetrate the ionization chamber wall. Provided a sufficient wall thickness, these effects contribute to a state of CPE in the air cavity. From Eq.(2.23), it is then possible to approximate the absorbed dose to the air cavity by the electronic air-kerma. Due to these above reasons, the most common reference dosimetry protocols for kV photon beams are based on ionization chambers calibrated in terms of air-kerma, where the absorbed dose to water is calculated by exploiting the large cavity relationship of Eq.(2.45) [86]. Some of the different kV x-ray beam dosimetry protocols or codes of practice currently in use are (along with the country/region of issue): DIN 6809-4 [87] and DIN 6809-5 [88] (Germany), IPEMB [89, 90] (UK), AAPM TG-61 [54] (North America), NCS-10 [91] (Netherlands and Belgium), and IAEA TRS-277 [92, 93] (international).

In the air-kerma protocols, the user must have an ionization chamber which has been calibrated against an FAC at a standards lab, yielding a chamber-specific air-kerma calibration coefficient (N_K) for a reference beam quality Q_0. The air-kerma from a kV x-ray beam of quality Q_0 can then be determined by a measurement with the ionization chamber (yielding a signal M, corrected for influence quantities):

$$K_{\text{air}} = MN_K \tag{2.50}$$

It is the objective of the aforementioned protocols to determine the absorbed dose to water from the measurement of air-kerma. While each protocol is distinct, they share many similarities in their recommendations in their dose formalisms. In general, the procedures for dose determination are subdivided by energy range, related to the clinical application of the x-ray beam.

Low energy x-rays ($\sim< 100$ kV$_p$) are typically used for superficial treatments, thus one is concerned with the dose to the surface of a water phantom. These measurements can be performed in air, or alternatively on the surface of a dedicated phantom with a parallel-plate ionization chamber (recommended for very low energy x-rays, $<$50 kV$_p$). For the in air method, the air-kerma is measured by irradiating an ionization chamber free in air. The air-kerma is converted to dose to water at the surface of a water phantom by first multiplying by the ratio of mass energy absorption coefficients of water to air in air (yielding water-kerma in air), followed by multiplication with a backscatter factor (BSF) which converts water-kerma in air to water-kerma at the surface of a water phantom (depth of $z = 0$). Due to the presence of CPE, it is assumed that water-kerma is equivalent to absorbed dose to water:

$$D_{w,z=0} = MN_K B_w \left[\left(\frac{\bar{\mu}_{\text{en}}}{\rho} \right)^w_{\text{air}} \right]_{\text{air}} \tag{2.51}$$

where B_w is the BSF in water for the given beam quality, field size, and source to surface distance, and $[(\bar{\mu}_{\text{en}}/\rho)^w_{\text{air}}]_{\text{air}}$ is the mass energy absorption coefficient ratio of water to air, free in air. The values of B_w and $[(\bar{\mu}_{\text{en}}/\rho)^w_{\text{air}}]_{\text{air}}$ are provided in the codes of practice. In the TG-61 code of practice, an additional factor, $P_{\text{stem,air}}$, is included in Eq.(2.51) which corrects for the change in photon scatter from the chamber stem between measurement and calibration field sizes (if the same field size is used in calibration and measurement, $P_{\text{stem,air}} = 1$).

When performing the measurement on the surface of a phantom, it is important to know whether the chamber air-kerma calibration coefficient was determined with or without the presence of the phantom. If without, the absorbed dose is:

$$D_{w,z=0} = MN_K p_{\text{ch}} \left[\left(\frac{\bar{\mu}_{\text{en}}}{\rho} \right)^w_{\text{air}} \right]_{z=0,\phi} \tag{2.52}$$

where the mass energy absorption coefficient ratio is calculated from the x-ray spectrum at the surface of the water phantom (including scattered photons), and a given field diameter ϕ. The perturbation factor p_{ch} corrects for the presence of the ionization chamber and any differences between measurement and calibration conditions. It has been reported that p_{ch} can be as large as 1.10 [90]. If the chamber N_K had been measured with the presence of the phantom at the standards lab (i.e. N_K is based on readings which include backscatter), the formalism of Eq.(2.51) holds.

Medium energy x-rays ($\sim$100 to 300 kV$_p$) are often used to treat deep-seated tumours in tissue, thus it is more relevant to determine the dose at a depth in water (typically 2 cm) rather than on the surface. These measurements are performed by irradiating an ionization chamber positioned at 2 cm depth in a water phantom. The absorbed dose to water at this depth is:

$$D_{w,z=2} = MN_K p_{\text{ch}} \left[\left(\frac{\bar{\mu}_{\text{en}}}{\rho} \right)^{w}_{\text{air}} \right]_{z=2,\phi} \tag{2.53}$$

where $[(\bar{\mu}_{\text{en}}/\rho)^{w}_{\text{air}}]_{z=2,\phi}$ is calculated from the x-ray spectrum in water at a depth of 2 cm for a field diameter ϕ. The perturbation factor p_{ch} corrects for all the effects mentioned in Eq.(2.52), as well as the possible presence of a waterproofing sleeve for the ionization chamber.

2.5.4 kV Dosimetry Protocols: Absorbed Dose to Water Calibration

As the desired quantity in radiation dosimetry is the absorbed dose to water, there have been advances at primary standards laboratories to provide a direct absorbed dose to water standard (based on calorimetry, ionometry and chemical dosimetry). These standards allow for ionization chambers to be calibrated in terms of absorbed dose to water, yielding a chamber absorbed dose to water calibration coefficient, N_{D,w,Q_0}, at reference quality Q_0. The absorbed dose to water can then be determined at a reference depth z_{ref} for the beam quality Q_0 by from a chamber measurement M:

$$D_{w,Q_0}(z_{\text{ref}}) = M(z_{\text{ref}}) N_{D,w,Q_0}. \tag{2.54}$$

Dosimetry protocols which are based on the absorbed dose to water are generally more recent, and tend to be less complex (i.e., less prone to user error) than those based on air-kerma. As well, there are multiple international metrology standards for the absorbed dose to water compared to only the FAC for air-kerma, giving a robustness to $N_{D,w}$ dosimetry systems which is not present with N_K protocols [50]. However, absorbed dose to water calibrations are not generally available for kV x-ray beams, and most codes of practice based on $N_{D,w}$ are only applicable to high energy photon/electron beams [86]. An exception is the IAEA TRS-398 protocol [55], which provides a general formalism for a wide range of radiation beams including kV x-rays. In this formalism, the absorbed dose to water from a beam quality Q different than the chamber calibration quality Q_0 is

$$D_{w,Q}(z_{\text{ref}}) = M(z_{\text{ref}}) N_{D,w,Q_0} k_{Q,Q_0} \tag{2.55}$$

where k_{Q,Q_0} is a correction factor which accounts for the effects of the differences between Q and Q_0 on N_{D,w,Q_0}. As mentioned, most standards labs only offer N_K ionization chamber calibration for kV x-rays, however it is possible to derive N_{D,w,Q_0} from N_K. For medium energy x-ray measurements performed in phantom, the chamber absorbed dose to water calibration coefficient can be found from:

$$N_{D,w,Q_0} = N_{K,Q_0} \left[\left(\frac{\bar{\mu}_{\text{en}}}{\rho} \right)^{w}_{\text{air}} \right]_{\text{phantom}} p_{\text{ch},Q_0} \tag{2.56}$$

where $[(\bar{\mu}_{\text{en}}/\rho)^{w}_{\text{air}}]_{\text{phantom}}$ is evaluated for the beam quality Q_0 at the measurement depth in the phantom. For low energy x-ray measurements of the dose to the phantom surface, N_{D,w,Q_0} is related by

$$N_{D,w,Q_0} = \frac{M_{\text{air}}}{M_{\text{surface}}} N_{K,Q_0} \left[\left(\frac{\bar{\mu}_{\text{en}}}{\rho} \right)^{w}_{\text{air}} \right]_{\text{air}} B_w \tag{2.57}$$

where M_{air} and M_{surface} are the chamber readings free in air, and on the surface of the phantom, respectively [55].

2.5.5 kV Dosimetry Protocols: Brachytherapy

The reference dosimetry protocols for an external radiation beam all involve measurements performed with an ionization chamber to determine the absorbed dose to water a point of interest. In brachytherapy, the source of radiation is not external, but contained within the medium of interest, and given information about the source (radiation strength, geometry, etc.), it is possible to calculate the absorbed dose to water at any point in the medium. As such, the dosimetry protocols for brachytherapy sources involve calibration of the source itself at a primary standards lab. The calibration of photon-emitting brachytherapy sources is performed by standards labs using one of two quantities related to air-kerma: reference air-kerma rate ($\dot{K}_R$, or RAKR), or air-kerma strength (S_K).

The RAKR is defined as the air-kerma rate, in air, at a reference distance of 1 m from the source center (corrected for air attenuation and scattering, i.e. *in vacuo*). For low energy photon sources, ICRU Report 72 [94] recommends that the RAKR only include contributions from photons above a threshold energy δ, where the value of δ is typically 5 keV but can vary with the source energy and application [95]. This revised definition, $\dot{K}_\delta$, was proposed as photons below δ

do not contribute significantly to the absorbed dose rate in water beyond ∼1 mm depth, however they do affect the air-kerma measurement.

Air-kerma strength was introduced by the AAPM [96], defined as the product of air-kerma rate (*in vacuo*) measured at a distance d from the source center along the perpendicular bisector, and the square of the distance:

$$S_K = \dot{K}_R(d)d^2. \tag{2.58}$$

Similar to the modification of RAKR, an updated definition of air-kerma strength was recommended by Rivard *et al.* [97] which removed the contribution from low-energy photons by using $\dot{K}_\delta$ in the place of $\dot{K}_R$. Assuming inverse-square law behaviour of a point source, the value of air-kerma strength is independent of the measurement distance. Since RAKR is measured at 1 m, the numerical values of reference air-kerma rate and air-kerma strength for a source will be identical, however they will have different units (mGy h^{-1} and mGy h^{-1}m^2, respectively).

The AAPM Task Group 43 [98, 97] (TG-43) recommended a generalised formalism for the calculation of absorbed dose to water from brachytherapy sources, which has been adopted worldwide [95]. In this formalism, the dose rate to water at a reference point (defined as a distance $r_0 = 1$ cm from the source center on a perpendicular bisector, $\theta_0 = 90°$) is:

$$\dot{D}(r_0, \theta_0) = S_K\Lambda \tag{2.59}$$

where Λ is the source dose rate constant, which converts air-kerma strength to absorbed dose to water measured at the reference point. The value of Λ can be determined either experimentally or by Monte Carlo simulation, and is provided in TG-43 (and its update, TG-43U1) for most brachytherapy source types.

To calculate the absorbed dose to water at any point, the extended expression of Eq.(2.59) is:

$$\dot{D}(r, \theta) = S_K\Lambda\frac{G_L(r, \theta)}{G_L(r_0, \theta_0)}g_L(r)F(r, \theta) \tag{2.60}$$

where $G_L(r, \theta)$ is the geometry function ($G_L(r, \theta) \to r^2$ for a point source), $g_L(r)$ is the radial dose function which accounts for attenuation and scattering, and $F(r, \theta)$ is the anisotropy function which accounts for dose variation as a function of polar angle θ. Again, values for these parameters are provided in TG-43 for most brachytherapy sources. Parameters specific to the Xoft Axxent source can be found in Rivard *et al.* [99]

Since the NIST primary standard for the Xoft Axxent reports the air-kerma rate in air at 50 cm, rather than the air-kerma strength, a modification to the TG-43 formalism was proposed by

DeWerd *et al.* [80] in 2015. In their approach, the dose rate to water can be found for the source and applicator i:

$$\dot{D}(r,\theta) = \dot{K}_{50cm}\chi_i(r_0,\theta_0)G_P(r,\theta)g_i(r)F_i(r,\theta) \tag{2.61}$$

where $\chi_i(r_0,\theta_0)$ is the dose rate conversion coefficient for applicator i, $G_P(r,\theta)$ is the geometry function (point source approximation), and $g_i(r)$ and $F_i(r,\theta)$ are the radial dose function and anisotropy function for applicator i, as in the original equation (2.60). Analogous to the dose rate constant Λ, the dose rate conversion coefficient converts the air-kerma rate in air at 50 cm to absorbed dose to water at the reference point of $r_0 = 1$ cm, $\theta_0 = 90°$.

2.6 Dosimetry of the INTRABEAM System

As mentioned in section 2.5.2, there is no primary standard for the INTRABEAM. The calibration of the INTRABEAM system is performed by the manufacturer using a soft x-ray ionization chamber (PTW 23342, Physikalisch Technische Werkstätte, Freiburg) submerged in a water phantom along with the INTRABEAM source [100]. The chamber measurements are in terms of exposure rate, which are then converted to absorbed dose rate to water using a factor of $f = 0.881$ cGy/R, based on data from ICRU Report 17 for 20 keV monoenergetic photons [101]. This process is repeated for a range of distances from the source in water, generating a depth dose rate curve which is used for calculating treatment delivery time [102].

The reproducibility of the INTRABEAM source output is monitored as part of the system quality assurance. Before the user is able to operate the INTRABEAM, the output must be measured using a PTW 23342 ionization chamber mounted in a QA tool (PAICH - Probe Adjuster/Ionization Chamber Holder). The PAICH measurement is related to the calibration dose in water at a reference depth, and any small variation in output is accounted for by the INTRABEAM treatment software by adjusting the treatment time [100]. This method of calibration was established prior to the start of the TARGIT-A trial (pre-2000), and has been maintained to ensure consistency in the delivered prescription doses despite the development of improved kilovoltage dosimetry protocols (i.e. AAPM TG-61 [54] or IAEA TRS 398 [55]).

Zeiss offers an optional water phantom for users wishing to perform depth dose measurements with their INTRABEAM source. The self-shielded phantom includes a 3-dimensional translational stage for mounting and positioning the source. Measurements are performed with a PTW 34013 soft x-ray ionization chamber placed in a waterproof holder. The following equation is recommended for calculating the absorbed dose to water:

$$D_W^{Zeiss}(z) = M(z) N_k k_Q k_{K_a \to D_W}, \tag{2.62}$$

where $M(z)$ is the measured charge (corrected for influence quantities), N_k is the PTW 34013 air-kerma calibration coefficient, k_Q is the conversion factor from reference to INTRABEAM beam quality, and $k_{K_a \to D_W}$ is the chamber conversion factor from air-kerma to dose to water in a reference beam. The INTRABEAM beam quality is assumed to be equivalent to a 30 kV$_p$ (T30) reference beam ($k_Q = 1$), and that k_Q is depth independent [102].

However, to compare the dose calculated with Eq.(6.1) ("Zeiss dose") with the dose reported in the calibration file, it must first be multiplied by a depth-dependent conversion factor, $f'(z)$, yielding the so-called TARGIT dose,

$$D_W^{TARGIT}(z) = f'(z) \cdot D_W^{Zeiss}(z). \tag{2.63}$$

The factor $f'(z)$ can vary from 0.5 to 0.9, and is intended to account for the differences in measurement conditions between the manufacturer source calibration and the Zeiss water phantom. The INTRABEAM water phantom manual explains these differences to be: the change in effective point of measurement between the ionization chamber models used (PTW 23342 and 34013); different designs of waterproof holders for the two ionization chamber models; and different chamber calibration schemes (PTW 23342 in terms of exposure with $f = 0.881$ cGy/R, and PTW 34013 in air kerma with $k_{K_a \to D_W}$, presumably calculated with updated mass-energy absorption coefficients and $(W/e)_{\mathrm{air}}$) [103]. The differences in chamber effective point of measurement (presumably due to volume averaging and different beam solid angles accepted by chamber entrance windows; 2.9 mm vs 5.2 mm diameter for the 34013 and 23342, respectively) and the presence of different waterproof holder designs can explain the depth-dependence of $f'(z)$, while the calibration in terms of exposure vs air-kerma would lead to a constant offset.

Whatever the justifications are for $f'(z)$, by definition the absorbed dose to water is the energy imparted per unit mass of water and should not be influenced by the experimental measurement setup. The requirement for a conversion factor to relate the TARGIT dose with the water phantom Zeiss dose is problematic, and it is not clear if the physical dose to water is best described by the TARGIT dose, the Zeiss dose, or neither [31]. This confusion in the system dosimetry makes it impossible to perform meaningful comparisons between the doses delivered with the INTRABEAM and other radiation emitting devices, and is clinically unacceptable.

2.7 Conclusion

In this chapter, the basic quantities used in radiation dosimetry relevant to this thesis were defined. The different types of ionizing radiation detectors used in radiation therapy were discussed, with a focus on air-filled ionization chambers and radiochromic film. Cavity theory was introduced, and contrasted with the direct determination of f_Q via MC simulations of radiation detector response. The current primary standards and reference dosimetry protocols for kilovoltage photon beams were covered. Lastly, the dosimetry of the INTRABEAM system was discussed, motivating the investigations of this thesis.

3

Monte Carlo Simulations of the INTRABEAM System

3.1 Preface

This chapter covers the basics of Monte Carlo particle transport simulations and describes a model of the INTRABEAM x-ray source created using the EGSnrc particle transport code. This model will be used in Chapters 5 and 6 to calculate parameters for a new dose formalism to calculate the absorbed dose to water from the INTRABEAM.

3.2 Introduction

The Monte Carlo (MC) method is a class of numerical procedures for estimating the solution to a problem (often too complex to be solved analytically) by using randomly sampled probability distributions. The random sampling of the distributions requires the use of random numbers, hence the gambling analogy to “Monte Carlo”, a term attributed to N. Metropolis, one the pioneers of MC methods [104]. From the sampled events, deterministic calculations may them be performed, and an accurate solution can be reached by aggregating the results from a large number of events. Notably, MC methods were formally developed by physicists working at Los Alamos on thermonuclear weapons research in the late 1940s [105].

The MC method estimates the expectation value (m_x) and variance (σ_x^2) of a probability distribution by sampling a large number of determinations (x_i). In the large sample limit ($N \to \infty$), the expectation value can be estimated by the sample arithmetic mean:

$$m_x \approx \bar{x} = \frac{1}{N}\sum_{i=1}^{N} x_i \tag{3.1}$$

and the variance by the square of the standard deviation of the sample:

$$\sigma_x^2 \approx s_x^2 = \frac{1}{N-1}\sum_{i=1}^{N}(x_i - \bar{x})^2. \tag{3.2}$$

The standard uncertainty is defined as the standard deviation of the mean,

$$\sigma_{\bar{x}} = \frac{s_x}{\sqrt{N}} \tag{3.3}$$

hence the Type A uncertainty on the value of $\bar{x}$ is inversely proportional to the root of the number of samples performed. Reducing the Type A uncertainty then requires the calculation of large sample sizes, which manifests as longer computational time to run the simulation. In order to reduce the calculation time of an MC simulation without compromising the uncertainty, various techniques have been developed collectively known as *variance reduction techniques*, which use various methods (ex: weighting factors to increase the occurrence of certain sampling regions) without biasing the results. Another technique to reduce simulation time is through *parallelisation*, where the total number of samples to be performed is distributed over multiple CPU cores to be run in parallel. This method exploits the parallel nature of MC simulations, where each sample is assumed to be independent from one another provided they use different random numbers. The results from parallel runs can then be combined.

3.3 Monte Carlo Particle Transport

The simulation of particle transport lends itself to MC methods as the mechanisms of particle interactions with matter are described by probability distributions (via interaction cross sections) and are discrete stochastic processes. As well, the integro-differential equations which describe radiation transport (i.e. Boltzmann transport equation) are challenging to solve analytically for even the simplest geometries and require severe approximations.

In an analogue MC simulation, all particle interactions are simulated in a discrete manner. The probability of a particle interaction between a path length s and $s+\Delta s$ is assumed to follow a Poisson distribution. It can be shown that the probability density function of a Poisson process is an exponential distribution:

$$f(s) = \mu e^{-\mu s} \tag{3.4}$$

where μ is the linear attenuation coefficient of the material (inverse of mean free path). One can apply the inverse-transform method of random sampling to Eq.(3.4), where the cumulative probability distribution is transformed to a random number between 0 and 1. From here, we derive the equation for sampling the particle distance traveled between two consecutive interactions:

$$s = -\frac{1}{\mu}\ln(1-\xi) \tag{3.5}$$

where ξ is a random number between [0,1]. Once the path length to the next interaction has been determined, the type of interaction is sampled from appropriate relative probabilities. The *analogue* approach (or event-by-event) is used by most MC codes for the transport of uncharged particles[1], where the mean free paths are relatively large compared to the dimensions of the geometry under investigation.

The highly dense nature of charged particle interactions renders an analogue simulation excessively long. A solution to this issue was the development of the *condensed history* technique by Berger [106], where large numbers of transport and collision processes are condensed into a single step. The transition from step n to step $n+1$ accounts for the cumulative effect of many individual interactions by considering multiple scattering distributions and the stopping power to sample the net change of particle energy, direction and position. For both analogue and condensed history simulations, a particle is tracked until its kinetic energy drops below a defined cut-off energy, or the particle exits a region of interest.

---

[1] Analogue codes also exist for transporting very low energy charged particles in microscopic geometries (ex: <1 keV electrons in a cell nucleus).

3.3.1 EGSnrc Radiation Transport Software

The EGSnrc code [107] was developed at the National Research Council of Canada (NRC) in Ottawa, and was adapted from the EGS4 (Electron-Gamma-Shower) code [108] originally written for high energy physics simulations at the Stanford Linear Accelerator (SLAC) in Stanford, California. EGSnrc is a general MC particle transport code with enhancements for use in medical physics research, and can simulate the transport of photons, electrons and positrons in matter. Particles are transported in the energy range of 100 GeV down to 1 keV through materials with user defined geometries. Materials can be any element with $Z = 1$ to 100, and users have the option to create arbitrary compounds and mixtures.

Photon Transport

In the EGSnrc code, photons may interact with the surrounding media by five processes: photoelectric absorption, incoherent (Compton) scattering with atomic electrons, coherent (Rayleigh) scattering with molecules/atoms, pair/triplet production, and photonuclear attenuation. Photon transport is performed by an analogue simulation as outlined in Eq.(3.5).

In photoelectric absorption, the photon is absorbed by an atom and an electron is emitted with a kinetic energy equal to the incident photon energy minus the electron binding energy. The vacancy left in the ionized atomic shell is then filled though a relaxation process, leading to the emission of fluorescent photons and/or Auger or Coster-Kronig electrons. In the EGSnrc simulation, the total cross section for the interaction can be taken from a preset library, or can be user-supplied. For compounds and mixtures, first the interacting element is explicitly sampled. Next, the interacting electronic shell is explicitly sampled using photo-absorption branching ratios, and the binding energy of the interacting shell is subtracted from the photoelectron energy. The photoelectron direction is sampled from the Sauter distribution [109]. The relaxation of shell vacancies is performed by a subroutine, which can lead to the creation of additional fluorescence photons and/or Auger or Coster-Kronig electrons.

In Compton scattering, the photon interacts inelastically with the atom, resulting in a deflected photon with less energy, a liberated electron, and a shell vacancy. The default model in EGSnrc for calculating the Compton cross section is the Klein-Nishina formula (free electron at rest), with inclusion of electron binding effects and Doppler broadening (i.e. initial electron momentum) using the relativistic impulse approximation. The impulse approximation assumes a constant potential so that the target electron states can be represented by plane waves [107]. Radiative Compton corrections (one-loop approximation of Brown and Feynman [110]) can also be taken into account. There is an option for the user to instead use the bound Compton cross sections in the XCOM library, or to supply their own.

In Rayleigh scattering, the photon interacts elastically with the atom, resulting in a deflected photon with the same energy. By default, Rayleigh scattering is turned off, however it should be turned on for all simulations considering photons below 1 MeV. The elemental total Rayleigh cross section can be taken from a preset library, or can be user-supplied. The atomic form factors (i.e., amplitude of scattered EM wave normalised to incoming wave) are based on the work of Hubbell and Øverbø [111], and form factors for molecules are derived using the independent atom approximation (or can be user-supplied).

In pair production, a photon with energy greater than $2m_ec^2$, where m_e is the electron rest mass, can interact with the EM field of a nucleus and create an electron-positron pair. In triplet production, a photon with energy greater than $4m_ec^2$ can also interact with the field of an atomic electron, setting it free and producing an electron-positron pair (3 charged particles in final state). The total cross sections for pair and triplet events can be taken from a preset library, or can be supplied by the user. The pair production cross sections differential in energy are calculated using the extreme relativistic Born approximation with screening. By default, in EGSnrc triplet production is not explicitly modeled, but is taken into account by an approximate way by adding the triplet total cross section to the pair total cross section to sample the distances to subsequent pair production events. Recently, an option has been added to explicitly simulate triplet events according to the first Born approximation results of Votruba [112] and Mork [113]. In this thesis, all EGSnrc simulations concerned photons well below the pair threshold of 1.022 MeV, thus pair/triplet production was not included.

In photonuclear attenuation, an atomic nucleus absorbs an energetic photon, enters an excited state, and then decays. Ali and Rogers [114] added the photonuclear effect (attenuation only, no generation of secondary particles) into EGSnrc with the inclusion of photonuclear cross sections, taken from IAEA photonuclear data [115]. By default, photonuclear attenuation is turned off in EGSnrc. Photonuclear events can only occur for photons in the MeV range, and are not relevant for the work in this thesis.

Photon Cross Sections

As mentioned above, the total cross sections for photoelectric absorption, Rayleigh scattering, and pair/triplet production can be taken from a preset library. The EGSnrc default is to use the NIST XCOM database [116]. XCOM contains up-to-date photon cross sections for all elements from 1 keV to 100 GeV, and is one of the most widely used photon datasets [117]. Users can also select from the Evaluated Photon Data Library (EPDL) [118], or the older data (1970) of Storm & Israel [119].

Of note, the XCOM and EPDL data for photoelectric cross sections are based on unrenormalised subshell cross sections. In their review of key data for kV x-rays, ICRU Report 90 [52] remarked that accurate measurements of μ_{en}/ρ at low photon energies (<60 keV) [120, 53] had better agreement with older data compiled by Hubbell [121], based on the 1973 calculations of *renormalised* subshell cross sections by Scofield [122]. The differences between μ_{en}/ρ calculated with unrenormalised and renormalised values can be as large as 3.5% for air at 1 keV, however for the ratio of water to air, $(\mu_{\text{en}}/\rho)_{\text{w,air}}$, the differences are negligible in practice. As of late 2017, users of the develop branch of EGSnrc can request to use the renormalised photoelectric cross sections of Sabbatucci and Salvat [123].

Atomic Relaxations

Following the creation of an electronic shell vacancy, an ion will relax to its ground state through a series of electronic transitions, emitting fluorescence photons and/or Auger or Coster-Kronig electrons. In EGSnrc, the relaxation cascade is handled by a subroutine independent to the process which created the vacancy (ex: photoelectric absorption). This subroutine ignores transitions to/from shells with binding energy less than 1 keV. Transitions involving $K-$, LI, LII, and $LIII$ shells are calculated explicitly, while the $M-$ and $N-$ subshells are averaged by default. As of EGSnrc release V4-2.4.0 (2013), an option was added to account for the transitions to/from explicit $M-$ and $N-$ subshells using data from the Livermore Evaluated Atomic Data Library (EADL) [124]. Chapter 4 investigates the effect of including explicit $M-$ and $N-$shell transitions in the simulation of a low-energy x-ray source (Zeiss INTRABEAM).

Electron Transport

In EGSnrc, electrons and positrons can interact with matter through three processes: bremsstrahlung emission in the atomic or nuclear EM field, inelastic collisions with atomic electrons, and elastic collisions with nuclei and atomic electrons. Positrons are also able to annihilate with electrons, creating two 511 keV photons in the center-of-momentum frame. As discussed in section 3.3, due to the large ($\sim 10^6$) number of interactions charged particles undergo before they are locally absorbed, an analog simulation of particle transport is often impractical. EGSnrc employs a condensed history approach for electron transport of type “Class II”, where collisions with small energy losses are grouped into a single large step, but occasional catastrophic collisions with energy losses above given threshold energies are treated separately and simulated explicitly.

Bremsstrahlung production is modeled explicitly for bremsstrahlung photon energies above a threshold energy (1 keV in this work). Below this threshold, bremsstrahlung energy loss is accounted for in the electron restricted radiative stopping power used in the condensed history grouping. The EGSnrc default bremsstrahlung cross sections use that of Bethe & Heitler, with first Born approximation for electron energies below 50 MeV, and a high energy approximation with Coulomb correction above 50 MeV [125]. Users also have the option to use bremsstrahlung cross sections taken from the NIST database [126], which were used in the radiative stopping powers recommended in ICRU Report 37 [127]. A third option exists to use the NRC cross sections, which have the same nuclear bremsstrahlung cross sections as in the NIST database, but uses a more accurate calculation of electron-electron bremsstrahlung [107].

Like with bremsstrahlung production, electron inelastic collisions are modeled explicitly if the kinetic energy of the scattered electron is greater than a specified threshold. By default, in EGSnrc the binding energy of atomic electrons is ignored and the Møller cross section is used for electron-electron scattering (and Bhabha cross section for positron-electron scattering). Below the threshold energy, inelastic collisions are accounted for in the restricted electronic stopping power (and CSDA) used in the condensed history grouping. The effect of $K-$ and $L-$shell binding energies can be accounted for by enabling electron impact ionization (EII). When EII is set to ON, interactions with $K-$ and $L-$shell electrons with binding energies above 1 keV are computed using bound electron cross sections (chosen by user), and the shell vacancy is handled by the relaxation subroutine. All other interactions use the Møller cross section.

Positron-electron annihilation is considered a catastrophic event and is modeled explicitly in EGSnrc. Only annihilation into 2 photons is considered, and the cross section calculated with the first Born approximation is used.

In elastic scattering there is no energy loss to the incident electron, thus there are no catastrophic events to be modeled explicitly following the Class II implementation. Away from a boundary between materials, EGSnrc uses an exact multiple elastic scattering theory based on Goudsmit-Saunderson distributions, which is valid for any arbitrary step size. In the region close to a geometry boundary (i.e. an interface between two different materials), it is possible that in the next condensed history step a portion of the electron path could be in another material if the step size is too large, leading to an interface artifact. To address this, EGSnrc uses a boundary crossing algorithm which switches from multiple to single elastic scattering in the vicinity of a boundary. The switch to single elastic scattering was found to be most computationally efficient at 3 elastic mean free paths perpendicular distance from the electron to the closest boundary (the current default value) [107].

Variance Reduction Techniques

A variance reduction technique (VRT), in the context of MC particle transport simulation, is a statistical method which improves the simulation efficiency without biasing the result (i.e. physical processes remain accurate and statistical estimators remain unbiased). Other speed-up techniques used in the literature, such as raising the minimum energy for transporting electrons (below which they deposit their energy on the spot), are not true VRTs as they introduce a bias. Here, efficiency is defined as

$$\varepsilon_{\mathrm{MC}} = \left(\frac{\bar{x}}{\sigma_{\bar{x}}}\right)^2 \frac{1}{t} \tag{3.6}$$

where t is the amount of simulation time required to reach the standard uncertainty $\sigma_{\bar{x}}$ of quantity $\bar{x}$. Recall from Eq.(3.3) that $\sigma_{\bar{x}}$ is inversely proportional to the square root of the number of samples N, and that computation time is approximately linearly proportional with N. It follows from the definition of Eq.(3.6) that the efficiency is independent of the number of simulated samples.

EGSnrc and its many user codes have implemented a variety of VRTs. The VRTs used in this thesis will be briefly discussed.

Particle Splitting: A particle splitting technique enhances the number of particles (and hence, the probability for interaction) by replicating a given particle n_s times, with each split particle having a statistical weight of $1/n_s$. In this work, uniform (i.e., isotropic) bremsstrahlung splitting was employed to increase the efficiency of the INTRABEAM x-ray source simulation. A uniform fluorescence photon splitting routine was implemented in the `egs_chamber` user code to mitigate fluctuations in variance caused by unequal statistical weights between bremsstrahlung and fluorescence photons.

Range-Based Russian Roulette (RR): This technique is used to reduce the amount of computational time spent tracking electrons which do not have enough energy to reach a region of interest (i.e., cavity of ionization chamber) and thus cannot contribute directly to the dose. At each electron step, the CSDA range is evaluated. If this range is less than the shortest distance between the electron and a user-defined geometry surrounding the region of interest, the electron undergoes Russian Roulette (i.e., the electron will be terminated based a given survival probability, $1/N_r$). The surviving electrons will have a statistical weight increase by a factor of N_r, and any photons generated by a radiative event (bremsstrahlung or relaxation after electron impact ionization) will also have a high weight and must be split N_r times to avoid statistical fluctuations.

Forced Detection: Used with photons, forced detection is a technique where the contributions (i.e., kerma) from photons aimed at a scoring surface are accounted for before they cross the scoring region boundary. At every interaction point, all photons whose direction would intersect the scoring region in a straight line are fictitiously transported to the scoring surface, accounting for attenuation through any materials in their path. Forced detection was used in simulations with the EGSnrc user code `cavity` to calculate the air-kerma and/or HVL at a reference point.

Intermediate Phase-Space Storage (IPSS): In this method, a virtual surface surrounding a given volume of interest is defined. For any particle crossing the virtual surface, their phase-space (i.e. position, direction, and energy) is stored, and their transport is terminated. This phase-space is then used as a source for subsequent calculations, and can be reused for many different scenarios (i.e. different positions of an ionization chamber). IPSS was used in simulations with the EGSnrc user code `egs_chamber` to calculate the dose to an ionization chamber air cavity or small water volume.

Photon Cross Section Enhancement (XCSE): To increase the number of photon interactions in a region of interest, the material photon cross section in that region is increased by a factor b. Any incident photon is split into an interacting photon (weight of w_0/b) and a non-interacting photon (weight of $w_0(1-1/b)$), where w_0 is the weight of the incident photon. All secondary particles originating from a XCSE interaction will have weight w_0/b. Secondary charged particles are further transported, but all higher generation photons are terminated with probability $1/b$, likewise all non-interacting photons are terminated with probability $1-1/b$, restoring a weight of w_0 for all survivors. XCSE was used in regions in and surrounding the ionization chamber geometry (or small water volume) with `egs_chamber` simulations.

3.3.2 Modeling the INTRABEAM source

EGSnrc (Version 4-2.4.0) was used to perform simulations of the INTRABEAM source (see figure 3.1) to calculate dosimetric quantities of interest. A model of the INTRABEAM source was created with the `egs++` class library [128], based on published source geometry and material specifications of Yanch and Harte [4], and a more recent source model reported by Nwankwo *et al.* [5]. In both of these source models, the INTRABEAM probe body consists of an evacuated hollow nickel cylinder 3.2 mm in diameter, with an inner diameter of 2.2 mm. The distal 1.6 cm tip of the probe is beryllium in the place of nickel to allow for x-ray transmission. The x-ray target is a hemispherical shell of gold, on which a 50 keV electron beam is incident upon. The probe outer surface is coated with thin layers of biocompatible materials. Details of the two sets of IN-

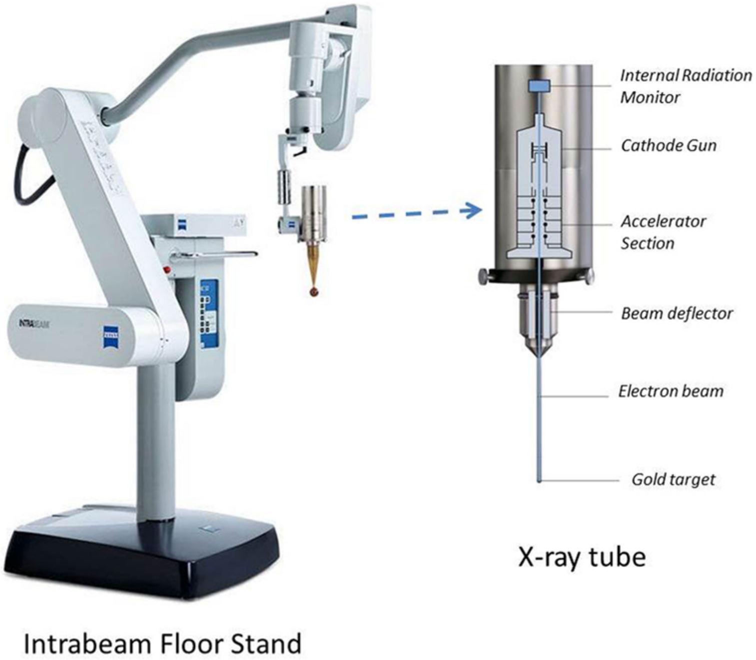

Figure 3.1 The INTRABEAM source with spherical applicator mounted on a floor stand. The inset on the right shows the internal components of the x-ray source. Image taken from Sethi *et al.* [2]

TRABEAM source parameters used are listed in table 3.1, taken from Ref.[48]. Unless otherwise specified, the Nwankwo *et al.* parameters were used in the simulations. Figure 3.2 shows a 3D representation of the INTRABEAM source geometry used in the simulations. The INTRABEAM electron source was modeled as a circular parallel beam ($r = 1.1$ mm) of monoenergetic 50 keV electrons.

The spherical applicators used in many INTRABEAM IORT treatments were also modeled (diameters of 3.5, 4.0 and 4.5 cm). Figure 3.3 shows the range of diameters of available spherical applicators. Initially, the applicators were treated as solid polyetherimide spheres, with the tip of the INTRABEAM probe situated at the sphere center. A more detailed spherical applicator model containing an air channel for inserting the INTRABEAM source probe was created based on specifications provided by the manufacturer. A cylindrical lead collimator used to create a narrow beam geometry during HVL measurements was also included in later simulation models. Figure 3.4 displays (a) the simplified spherical applicator model, and (b) the detailed model including lead collimator.

Table 3.1 Comparison of INTRABEAM source parameters used in Monte Carlo simulations. Specifications taken from Yanch and Harte [4] and Nwankwo *et al.* [5]

Materials		Yanch and Harte [μm]		Nwankwo *et al.* [μm]
Target	Au	0.5		1.0
Body	Be	500.0		500.0
Biocompatible	Ni	3.4	NiO	2.5
Layers	Rh	0.4	Ni	2.5
	TiN	1.0	CrN	2.5

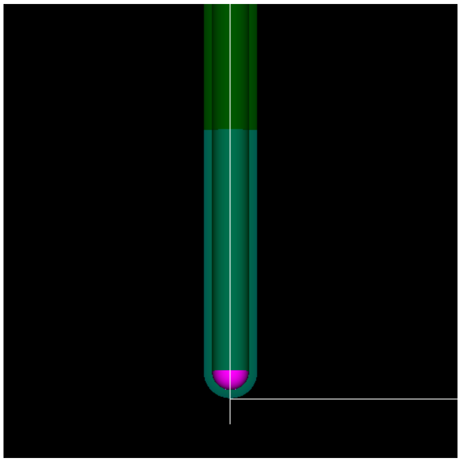

Figure 3.2 Rendering of the INTRABEAM bare probe geometry used in EGSnrc simulations.

3.4 Materials and Methods

The EGSnrc model of the INTRABEAM source was used to simulate the photon fluence spectra and HVL of the bare probe and spherical applicators. The fluence spectrum of the bare probe was compared qualitatively with the simulation results of Nwankwo *et al.*, who had used the GEANT4 [129] MC particle transport code in their calculation. The simulated HVLs were compared with published measured values, and our own HVL measurements. Simulations of absorbed dose to water in a water phantom using the EGSnrc model of the INTRABEAM are investigated in Chapter 5, and are compared with ionization chamber dose measurements.

Figure 3.3 INTRABEAM spherical applicators ranging in diameter from 1.5 cm to 5 cm. Image taken from Holmes *et al.* [3]

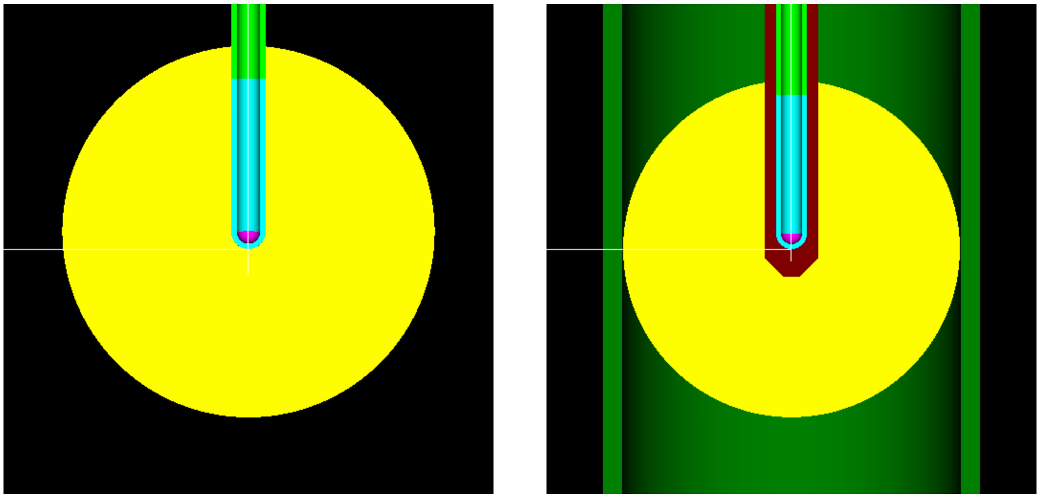

(a) Example of simplified applicator model

(b) Detailed applicator model including air channel (red) and cylindrical lead collimator (green)

Figure 3.4 EGSnrc geometries of an INTRABEAM spherical applicator (3.5 cm diameter) used in the simulation of photon fluence and HVL. The simplified model (a) was found to be insufficient for calculating the HVL.

3.4.1 Photon Fluence Spectrum

The EGSnrc user code `cavity` was used to calculate the photon fluence spectrum in vacuum, scored across a 1 cm diameter circular plane positioned at various distances from the probe tip/applicator surface, along the probe longitudinal axis. The position of the scoring plane relative to the INTRABEAM source was set to match the detector position during HVL measurements (both our own, and those reported in the literature). The fluence was binned by photon energy (0.1 keV bin width) from 1 keV to 51 keV.

3.4.2 Half Value Layer

The INTRABEAM bare probe and spherical applicator HVLs were determined by analytical calculation from spectra, and by attenuation measurements using a PTW 23342 soft x-ray parallel-plate ionization chamber.

Calculating HVL from Spectra

The HVL was determined analytically from the photon fluence spectra by first computing the air-kerma at the reference point:

$$K_i = E_i \Phi_i \left(\frac{\mu_{en}}{\rho} \right)_{i,\mathrm{air}}, \tag{3.7}$$

where E_i is the energy of photon bin i, and $\left(\frac{\mu_{en}}{\rho} \right)_{i,\mathrm{air}}$ is the mass energy absorption coefficient for air at energy E_i. Technically, Eq.(3.7) determines the electronic air-kerma, however, at the energies investigated the radiative fraction g is negligible and the electronic kerma is effectively equivalent to kerma. The air-kerma ratio for an attenuated to unattenuated beam was then calculated. As the simulations were performed in vacuum, the attenuation due to air is accounted for in the air-kerma ratio. As a first order approximation of ionization chamber response, the attenuation through the chamber entrance foil was also accounted for. The air-kerma ratio is given by:

$$K_{\mathrm{ratio}} = \frac{\sum_i K_i \exp(-\mu_{i,\mathrm{att}} x_{\mathrm{att}} - \mu_{i,\mathrm{air}} x_{\mathrm{air}} - \mu_{i,\mathrm{foil}} x_{\mathrm{foil}})}{\sum_i K_i \exp(-\mu_{i,\mathrm{air}} x_{\mathrm{air}} - \mu_{i,\mathrm{foil}} x_{\mathrm{foil}})}, \tag{3.8}$$

where μ_{att}, μ_{foil} and μ_{air} are the attenuation coefficients of the attenuator material (aluminium), chamber entrance foil (polyethylene) and air, respectively. Similarly, x_{att}, x_{foil} and x_{air} are the thicknesses of the attenuating material, chamber entrance foil (0.03 mm per manufacturer specifications) and air (source-to-detector distance). All attenuation coefficients were obtained from the NIST XCOM database [116]. The HVL was determined recursively by finding the thickness of aluminium (x_{att}) which attenuated the air-kerma by one half; $K_{\text{ratio}} = 0.5$.

The Type A uncertainty in the simulated HVL was estimated by error propagation of the statistical uncertainty (1σ) of Φ_i, and the uncertainty of the XCOM attenuation coefficients, taken to be 2% [130], across Eq.(3.8). The Type B uncertainties considered were: the error in source-to-detector distance positioning (±5 mm), the error in positioning the lead collimator (±1 cm), and for the spherical applicators, variations in applicator material (polyetherimide) density (±10%). The total uncertainty was the quadrature sum of all Type A and Type B uncertainties.

HVL Measurements

INTRABEAM attenuation measurements were performed by placing various thicknesses of high purity aluminium foils (99.0% pure) in between the source and PTW 23342 chamber during irradiation. The cylindrical lead collimator (1 mm thick lead sheet wrapped into a cylinder, 16 cm length) was positioned around the spherical applicators (inner diameter equal to applicator diameter), or in the case of the bare probe, around a hollow polyethylene cylinder used to protect the source during transportation (3.5 cm inner diameter). The aluminium attenuators (0.05 to 0.3 mm thick) were positioned at the exit of the collimator, 8 cm from the bare probe tip. The PTW 23342 chamber was positioned in line with the source probe and in the center of the collimator area using a laser ruler. Due to the small collecting volume of the ionization chamber (0.02 cm^3) and relatively low source output, the source-to-chamber distance of 1 m as recommended by TG-61 was found to give an insufficient signal during irradiation. A suitable signal was obtained by placing the chamber 13 cm from the bare probe source, and 9.5 cm from the source when spherical applicators were present (i.e. 7.75 to 7.25 cm from surface of the spherical applicators). The experimental setup of the attenuation measurements is shown in figure 3.5.

The collected charge during a 60 s irradiation was measured, repeated three times for each thickness of aluminum/no attenuator. The mean value μ and standard deviation σ were calculated for each set of measurements, and an attenuation curve was created by normalising the attenuator measurements by the signal through air only. The HVL was determined by fitting a function of the form $f(x) = ae^{-bx} + ce^{-dx}$ to the attenuation curve, and solving for the thickness which attenuated the open beam signal by half. This was done in MATLAB R2013b (The MathWorks, Inc., Natick, MA) using a fit weighted by the standard deviation of each attenuation data point,

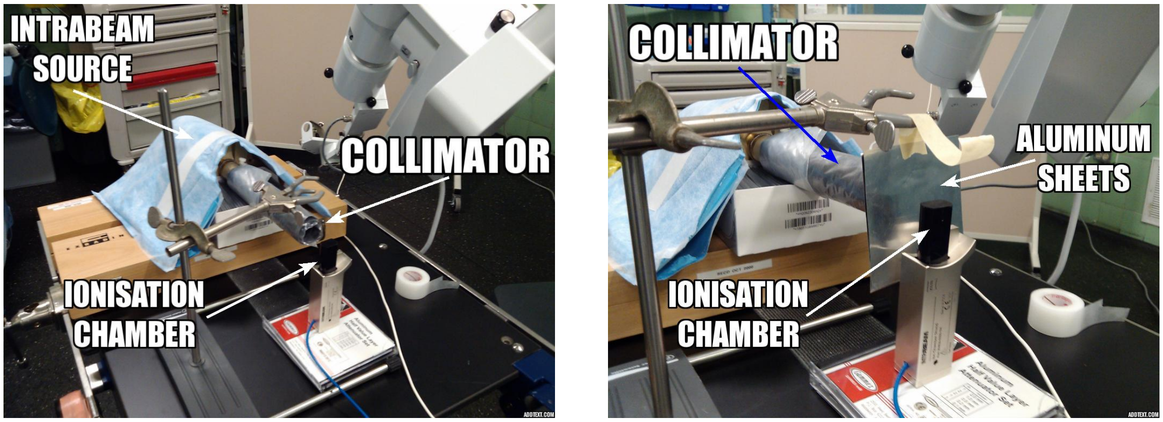

(a) Air measurement (no attenuator).

(b) Attenuator measurement.

Figure 3.5 Experimental setup during attenuation measurements of the INTRABEAM source.

$1/\sigma^2$. The 95% confidence interval of the fit at the HVL thickness was estimated by the function `predint` for a new observation at a single predictor value.

The total uncertainty in the HVL measurement was estimated to be the quadrature sum of the fitted confidence interval and the quoted tolerance of the aluminum foil thickness (assuming a rectangular distribution).

3.4.3 Phase Space Source

The EGSnrc model of the INTRABEAM source described above begins with an electron source striking the gold target, producing bremsstrahlung and fluorescence photons. However, most of the photons produced are reabsorbed within the gold target, and approximately only one photon per 500 initial electrons exits the INTRABEAM source probe. One technique in the MC simulation of x-ray sources is to write a phase-space file all particles crossing a user-defined boundary, usually at the exit of the x-ray source [131]. This phase-space file can then be used as a particle source for later simulations concerning interactions downstream from the x-ray source. The phase-space source has the advantage of not needing to spend computational time tracking the initial electrons through the x-ray target. However, phase-space files containing many particles (needed for sufficient statistics) require a large amount of disk space, and retrieving phase-space data over a network file system has been shown to be a computational bottleneck in some situations [132]. With these effects in mind, the efficiency gain of using an INTRABEAM phase-space source in the simulation of absorbed dose to water in a water phantom was investigated.

A set of `egs++` software tools to read and write phase-space files in IAEA format were created at McGill University by M.A. Renaud and A. Marchildon (private communication). A phase-space file was created of all particles exiting the outermost surface of the INTRABEAM source probe. This phase space file was then used as a particle source to calculate the photon fluence spectra and HVL (as in sections 3.4.1 and 3.4.2) which were compared with the results from using an electron source simulation.

Using the same phase-space source, the absorbed dose to water to a small cylindrical water volume ($r = 1.5$ mm, $h = 1$ mm) in a cubic water phantom ($30 \times 30 \times 30$ cm^3) was calculated at various depths in water using the `egs_chamber` user code. The dose was measured from 1 mm to 20 mm from the source in 0.5 mm increments along the source longitudinal axis. The same calculation was performed using an electron source, and the two sets of simulation results were compared by creating relative depth-dose curves, normalised to the 5 mm depth dose value. Both sets of simulations (phase-space and electron source) used the same parameters for the VRTs used: intermediate phase-space storage, photon cross section enhancement, and range-based Russian Roulette. Bremsstrahlung and fluorescence splitting was not used in these simulations.

The relative efficiency gain of using a phase-space source over an electron source in computing the dose to water was defined as $\varepsilon_{PHSP}/\varepsilon_e$, where the efficiency ε was determined by Eq.(3.6) at each depth in water. The effect of simulation parallelization was also investigated. Simulation "jobs" were submitted to run on 1 to 256 CPU cores, with the same total number of starting particles (also known as *histories*). All simulations were performed on the Guillimin high performance computing cluster at McGill University, managed by Calcul Quebec and Compute Canada. Jobs requiring fewer than 16 cores were run on Dual Intel Westmere EP Xeon X5650 processors (6-core, 2.66 GHz, 12MB cache, 95W), with 3 GB memory per core. Jobs using 16 or more cores were run on Dual Intel Sandy Bridge EP E5-2670 processors (8-core, 26 GHz, 20 MB cache, 115W), with 4 GB memory per core. The Guillimin cluster uses a 2:1 blocking QDR InfiniBand network to communicate between nodes.

3.5 Results

3.5.1 Photon Spectrum

The photon fluence spectra was calculated for the INTRABEAM bare probe and spherical applicators at a point 1 cm from the source tip/applicator surfaces. The results for the source model using the Yanch and Harte parameters are shown in figure 3.6. It can be seen that the spherical applicators are effective in attenuating the fluence below 20 keV, greatly reducing the contribution from fluorescence photons. In these spectra, atomic relaxations were calculated using averaged $M-$ and $N-$shells binding energies. The effect of the different source parameters reported by Yanch and Harte, and Nwankwo *et al.* on the INTRABEAM bare probe fluence spectrum is shown in figure 3.7. The variation in the bremsstrahlung portion of the spectra is due to the difference in the gold target thicknesses between the two models. The fluorescent peaks originating from the different material compositions in the outer biocompatible layers have been identified, while the shared peaks are $K-$lines of nickel (7.5 and 8.3 keV), and $L-$lines of gold.

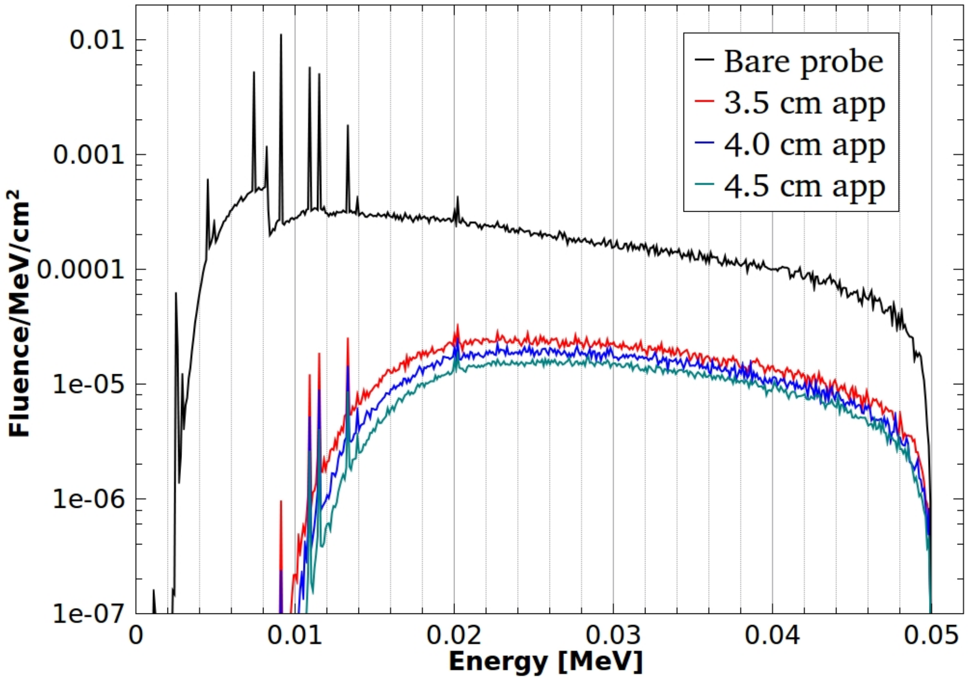

Figure 3.6 The simulated photon fluence spectra of the INTRABEAM source for the bare probe and spherical applicators (3.5, 4.0, and 4.5 cm diameter). The source parameters of Yanch and Harte [4] were used.

The effect of electron impact ionization (EII) on the fluence spectra was investigated by simulating the Nwankwo *et al.* source with EII disabled, and EII enabled using the cross sections of Bote and Salvat [133] (PENELOPE option). As shown in figure 3.8, enabling EII lead to a considerable increase in the number of fluorescence photons. This effect is expected, as EII accounts for the vacancies (and the subsequent relaxation process) produced by inelastic electron collisions with $K-$ and $L-$shell orbital electrons. Interestingly, the increase in fluence from EII

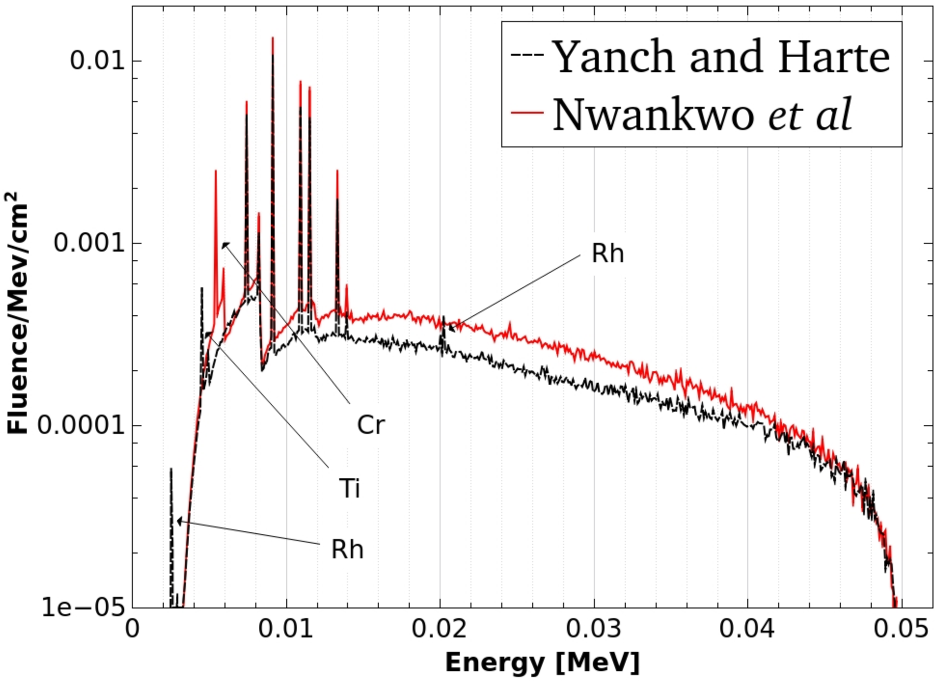

Figure 3.7 Simulated photon fluence spectra of the INTRABEAM bare probe using source parameters taken from Yanch and Harte [4], and Nwankwo *et al.* [5] The fluorescent peaks due to differences in material compositions have been identified.

fluorescence photons lead to a decrease in the mean energy of the fluence spectrum (20.1 keV to 18.1 keV), while increasing the HVL (0.068 mm Al to 0.072 mm Al). This phenomenon can be explained in that the HVL is a measure of beam penetration, and while correlated with the spectrum energy, it is not a straightforward relationship. Increasing the yield of fluorescence photons leads to a more penetrating spectra through aluminum, while reducing the mean energy.

By default, atomic transitions to and from the $M-$ and $N-$shells are treated in an average way in EGSnrc, however there exists an option to consider explicit $M-$ and $N-$subshell binding energies. The effect of $M-$ and $N-$shell averaging on the fluence spectra is evident with the introduction of new fluorescence peaks (see figure 3.9 (a)). Enabling all atomic transitions in EGSnrc is necessary for agreement between the fluorescence photon energies in the INTRABEAM fluence spectra simulated using GEANT4 (provided courtesy of C. Nwankwo), as shown in figure 3.9 (b). A more thorough discussion of the effect of explicit $M-$ and $N-$shell transitions on modeling the INTRABEAM source is presented in Chapter 4.

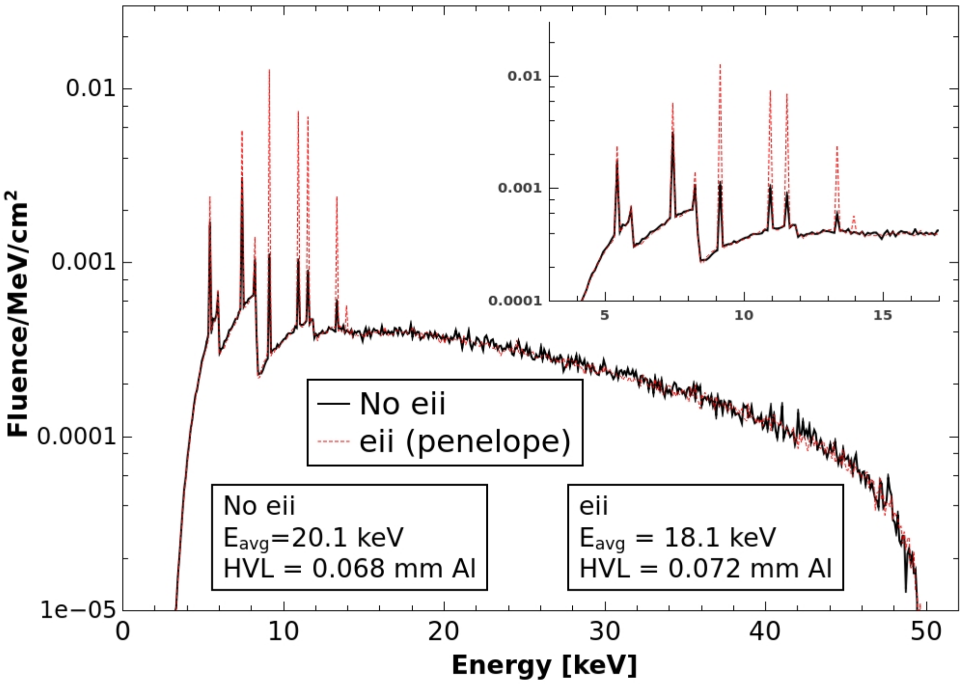

Figure 3.8 The effect of enabling electron impact ionization (EII) on the photon fluence spectrum is evidenced in the increase of fluorescence photons. Inset shows zoomed in region of fluorescent lines.

In the earliest set of photon fluence simulations of the spherical applicators, the presence of the lead collimator used during HVL measurements was ignored. A large discrepancy was found between the simulated and measured applicator HVLs (see figure 3.11), which could be accounted for by including the lead collimator in the EGSnrc simulation (see figure 3.13). This measurable effect on the HVL was determined to originate from the addition of fluorescence photons emanating off of the lead collimator (10 keV and 12 keV $L-$lines of Pb), as shown in figure 3.10. Including a small air channel in the center of the spherical applicators in the EGSnrc simulations was found to have a much smaller effect on the calculated HVL.

3.5.2 Half Value Layer

The HVL was calculated from the simulated photon fluence spectra using Eq.(3.8). For the bare probe, the uncertainty in the simulated HVL was estimated to be ΔHVL = 0.001 mm Al (0.0008 mm Al statistical uncertainty, and 0.0006 mm Al source-to-detector position uncertainty). For

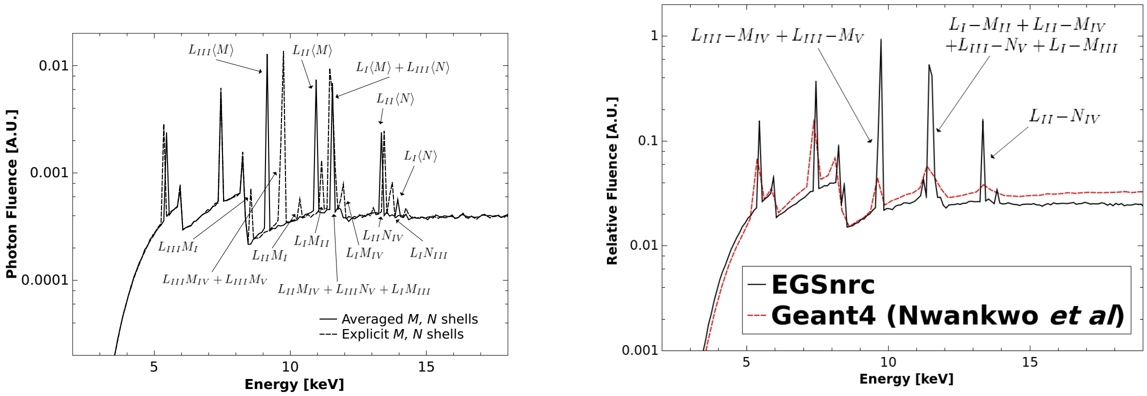

(a) Effect of $M-$ and $N-$shell averaging on photon fluence spectra.

(b) Comparison of INTRABEAM spectra calculated with GEANT4 and EGSnrc (explicit $M-$ and $N-$subshell transitions enabled).

Figure 3.9 (a) INTRABEAM photon fluence spectra calculated with and without explicit $M-$ and $N-$subshell transitions [6]. (b) Explicit $M-$ and $N-$subshell transitions are required in EGSnrc for agreement with INTRABEAM fluorescence peak energies as calculated with GEANT4 (spectrum provided courtesy of C. Nwankwo).

the spherical applicators, the uncertainties introduced by the position of the lead collimator along the beam axis, and variation in polyetherimide (applicator material) density were estimated by performing simulations at the extreme cases of each (i.e., maximum and minimum polyetherimide density, collimator shifted by ±1 cm) and calculating the change in HVL. For all applicator diameters, the simulated HVL uncertainty was determined to be ΔHVL = 0.04 mm Al (0.003 mm Al statistical uncertainty, 0.03 mm Al density variation, 0.03 mm Al collimator position, and 0.0005 mm Al source-to-detector position uncertainty).

For the measured data, attenuation curves were generated for the bare probe and spherical applicators and fit with a function, which was used to determine the HVL. Plots of the measured attenuation curves (with fits and confidence interval), along with simulated data are shown in figure 3.12.

The uncertainty of the measured HVLs was estimated by the fit confidence and tolerance on the thickness of aluminum attenuators (assuming a rectangular distribution of foil thicknesses). The attenuator thickness uncertainty ranged from 0.014 mm Al to 0.02 mm Al, and the fit confidence from 0.006 mm Al (bare probe), to 0.023-0.058 mm Al for the spherical applicators. The total uncertainty was determined to be ΔHVL = 0.016 mm Al (bare probe), and ΔHVL = 0.030 mm Al to 0.061 mm Al for the spherical applicators.

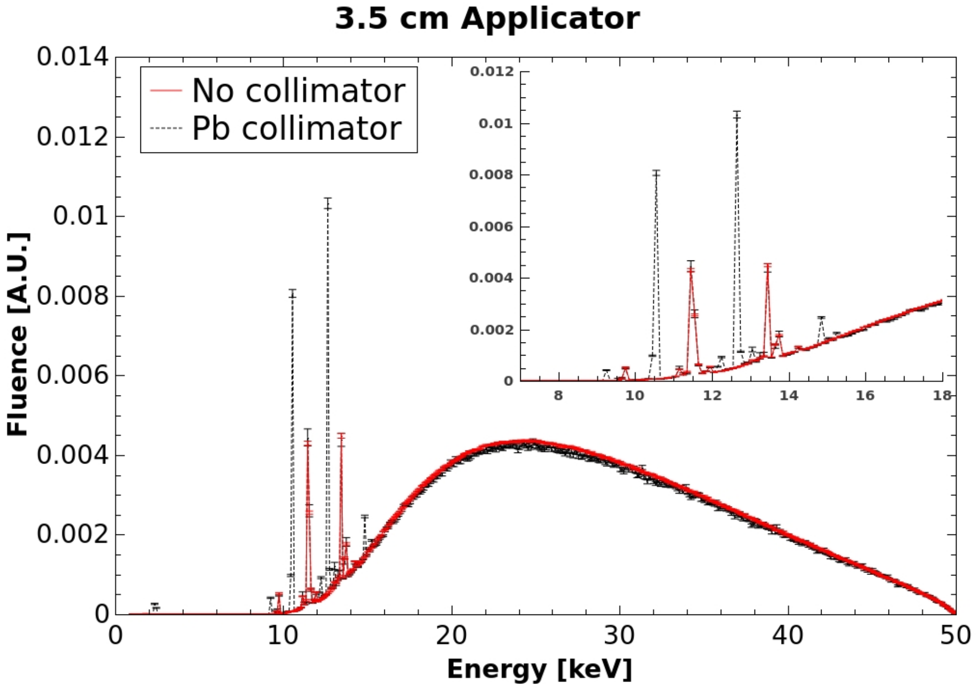

Figure 3.10 The presence of a lead collimator used during HVL measurements was found to introduce fluorescence photons coming off of the collimator ($L-$lines of Pb) which had a significant effect on the HVL. Inset highlights the low energy region of fluorescent lines.

Figure 3.13 shows the measured and simulated HVLs for the INTRABEAM bare probe and spherical applicators when accounting for the lead collimator and detailed applicator model in the EGSnrc simulation. The results are generally in good agreement considering uncertainties, with the largest discrepancy occurring for the 4.5 cm applicator (0.725 ± 0.04 mm Al vs 0.671 ± 0.034 mm Al for the simulated and measured HVLs, respectively), a 7.7% difference from the average value. Due to the sensitivity of the measured HVL on the photon spectrum, the relative position of the source and collimator to the detector, and the relatively low measured signal (<1 pA) during attenuation measurements, accurate measurements of the INTRABEAM spherical applicator HVLs are challenging.

The HVLs calculated from the INTRABEAM simulated fluence spectra were also compared with published values (see table 3.2). The simulated HVLs were calculated for the same source-to-detector distances as reported in the experimental setups of the given references. Many of the reported HVL values were measured in a broad beam (uncollimated) geometry, and contain air and room scatter which was not accounted for in the EGSnrc simulation, leading to an increase

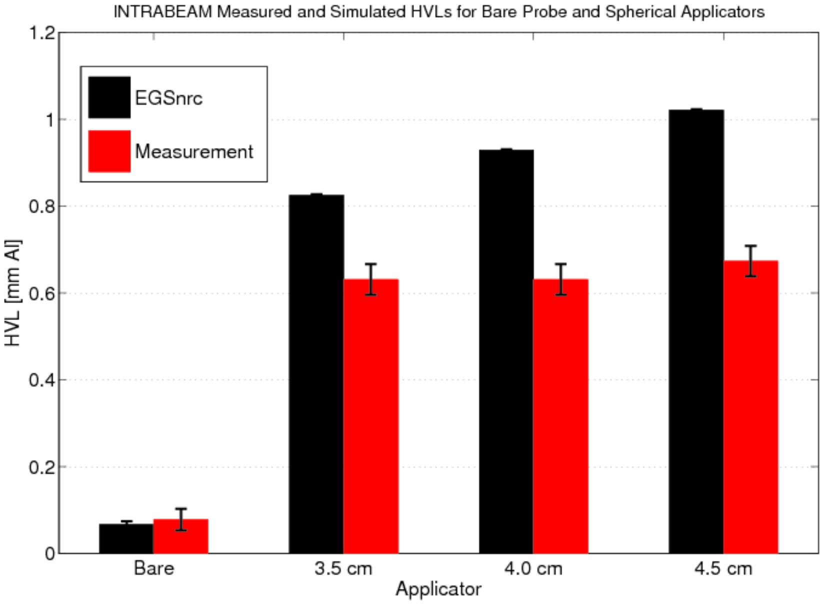

Figure 3.11 Comparison of measured and simulated (not accounting for lead collimator or applicator air channel) HVLs for the INTRABEAM source. A large discrepancy can be seen in the spherical applicator HVLs. Following this result, a more detailed model of the spherical applicators including the lead collimator was investigated.

in measured HVL. As well, the measurements of Eaton and Duck [41] were performed using a Farmer-type NE2571 thimble ionization chamber as opposed to a parallel-plate soft x-ray chamber, which may introduce a larger energy dependence in their measurement [134]. In general, the simulated HVLs were consistent with the reported values to within ±6%.

3.5.3 Phase Space Source

A phase-space file containing $\sim 10^8$ particles ($\sim$5 Gb) was generated on the surface of the INTRABEAM source probe. The photon fluence spectra from both the phase-space and electron sources were scored across a 1 cm diameter circle situated 1 cm from the tip along the longitudinal axis of the source. The spectra from the two sources were found to be in excellent agreement, as shown in figure 3.14. The HVLs at 1 cm in air were computed using Eq.(3.8) (ignoring attenuation through chamber entrance foil), and were also found to be in excellent agreement (0.0685 ± 0.0004 mm Al for electron source, versus 0.0685 ± 0.0005 mm Al for phase-space

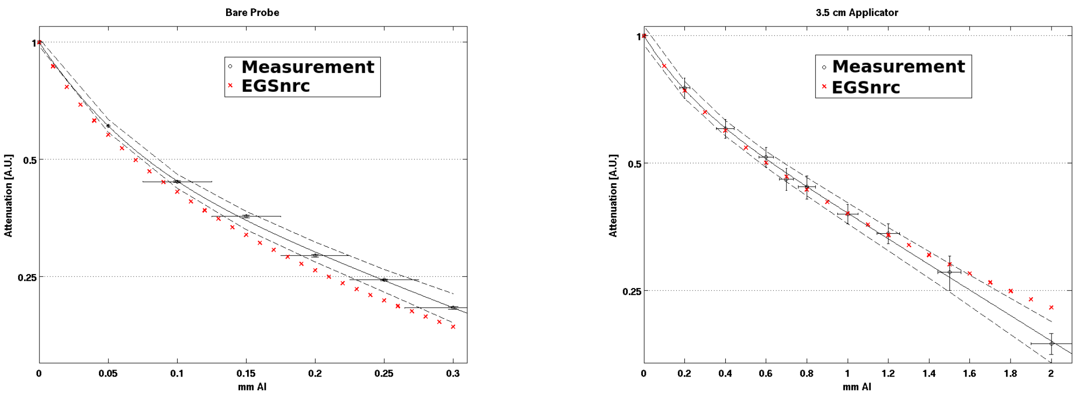

(a) Bare probe (b) 3.5 cm applicator

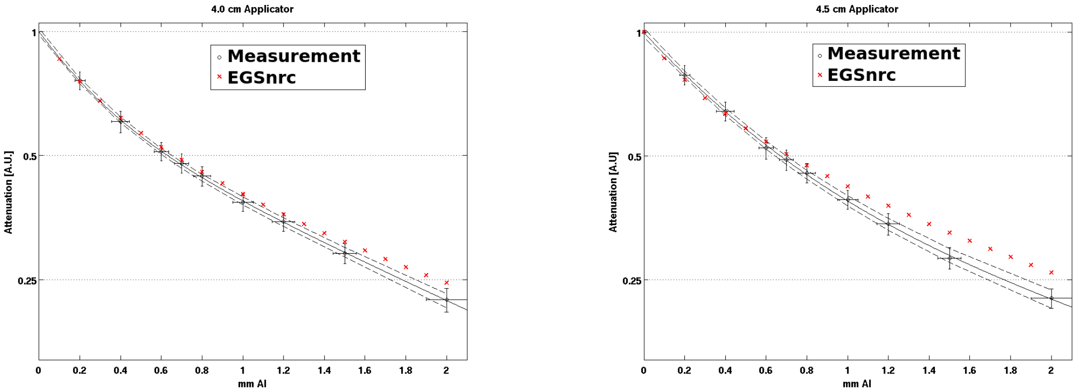

(c) 4.0 cm applicator (d) 4.5 cm applicator

Figure 3.12 Comparison of measured and simulated attenuation curves of the INTRABEAM source bare probe and spherical applicators.

source). These results suggest that the phase-space source is able to reproduce the INTRABEAM photon fluence spectrum and HVL as calculated with an electron source.

The relative depth dose to water (normalised to 5 mm depth) was calculated for both the phase-space and electron source. Figure 3.15 (Top) shows the two depth dose curves, while the bottom figure displays the local percent difference between the two curves. In general, there is good agreement between the two source curves, with a root mean square (RMS) error of 0.51% across the depth range investigated. A small discrepancy on the order of 1% difference is visible between the two source curves in the region 1-4 mm from the probe surface. However, this difference may be attributable to statistical fluctuations ($1\sigma \approx 0.3\%$ in this region).

The relative efficiency gain of using a phase-space source over an electron source when calculating the dose to a small water volume is shown in figure 3.16 as a function of depth in

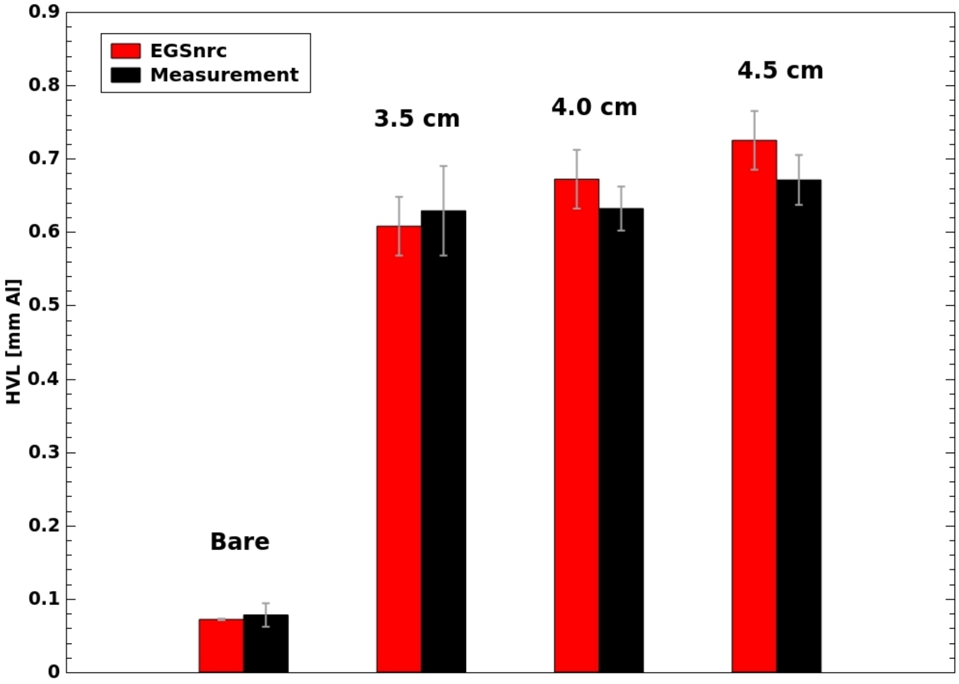

Figure 3.13 Measured and simulated HVLs for the INTRABEAM bare probe and spherical applicators. The presence of the lead collimator and applicator air channel were accounted for in the EGSnrc simulation.

Table 3.2 Comparison of simulated (EGSnrc) and published (Reported) INTRABEAM HVL values. The simulation source-to-detector distance was set to match the experimental setup used in the reported references. (Broad) refers to measurements made with an uncollimated beam.

	HVL [mm Al]		
	EGSnrc	Reported	Ref
Bare probe	0.076	0.11 (broad)	[135]
		0.10 (broad)	[39]
3.5 cm	0.85	0.80 (broad)	[136]
		0.85	[41]
4.0 cm	0.95	0.98 (broad)	[136]
4.5 cm	1.04	1.10 (broad)	[136]

water. The gain in efficiency was found to range from 190 to 20 and decreased with depth in water.

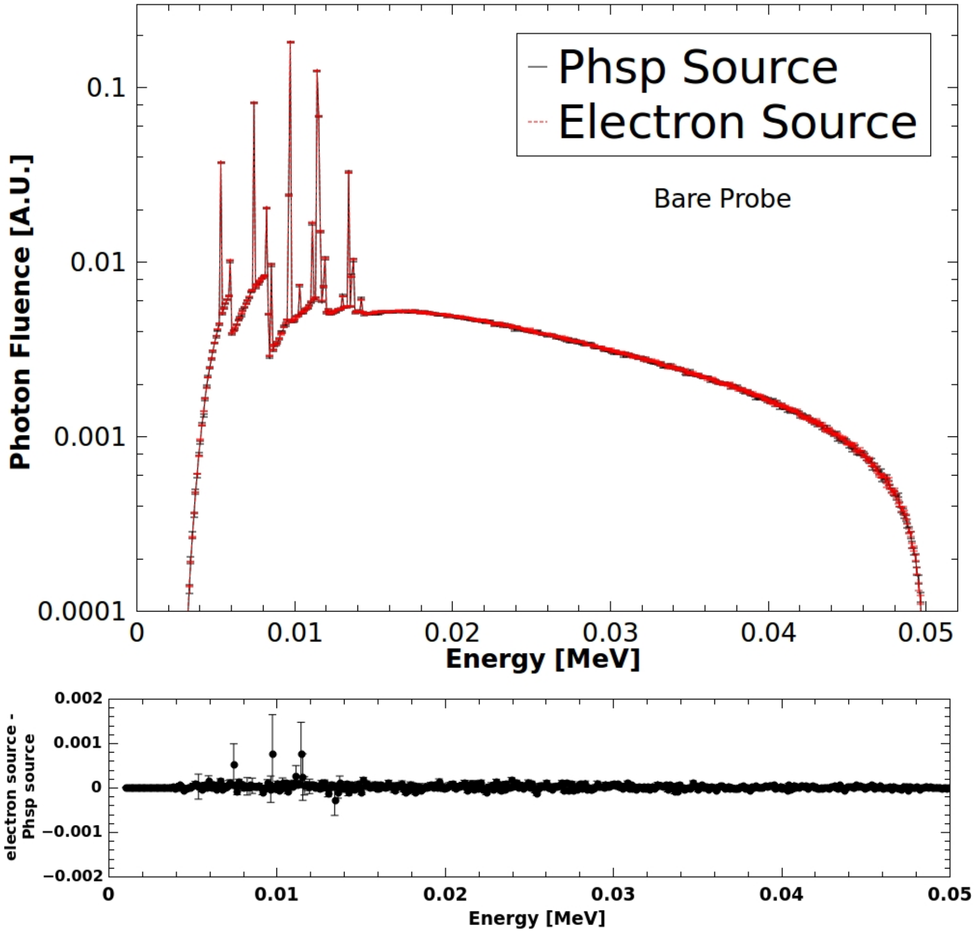

Figure 3.14 The INTRABEAM bare probe photon fluence spectra as calculated with a phase-space and electron source. Below, it can be seen that the difference between the two spectra are within statistical uncertainties.

The parallelisation of simulation runs was not found to have any adverse effect on the efficiency, highlighting the capability of the Gullimin cluster network system.

To investigate the origin of the depth dependence of the relative efficiency gain seen in figure 3.16, the dose to water simulations were performed again for each source, with all VRTs turned off. In this situation, the gain in efficiency of using a phase-space source increased to nearly 2000, and was independent with depth in water (see figure 3.17), suggesting that the VRTs enhance the efficiency of the electron source simulation more than the phase-space source, and that they are more effective at greater depths in the water phantom. In figure 3.18, the relative efficiency gain as defined by $\varepsilon_{VRT}/\varepsilon_{NoVRT}$ is plotted for both the phase-space and electron sources.

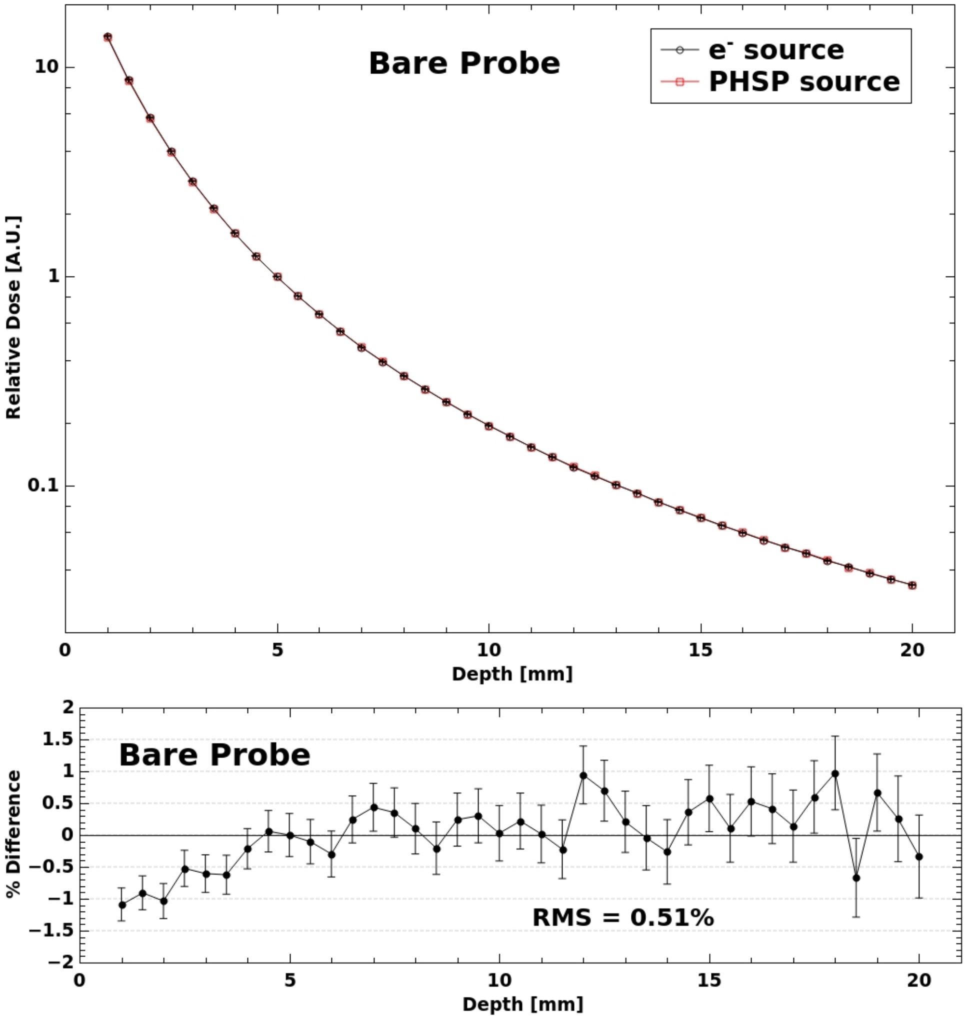

Figure 3.15 (Top) The INTRABEAM bare probe relative depth dose curve calculated with a phase-space and electron source, and (Bottom) the local percent difference relative to the electron source. The dose curves were normalised to 5 mm depth in water.

The VRT efficiency gain for the phase-space source increases from 10 to 60 with depth in water, while the electron source gain ranges from 100 to 4000 across the same depth. This result shows that the VRTs are indeed more helpful towards the electron source than the phase-space source in improving the calculation efficiency deep in the phantom. This may be due to VRT enhancements made during transport in the INTRABEAM x-ray target which do not occur with the phase-space source.

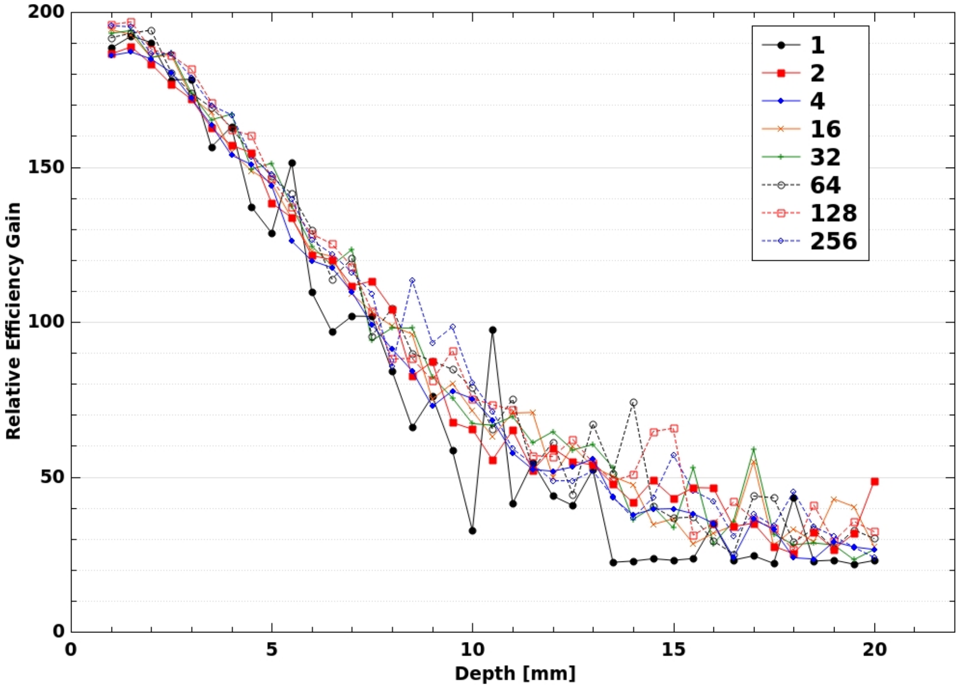

Figure 3.16 The relative efficiency gain of using a phase-space over an electron source in calculating the dose to water from the INTRABEAM bare probe, as a function of depth in water. the numbers in the legend refer to the job splitting (amount of parallelization).

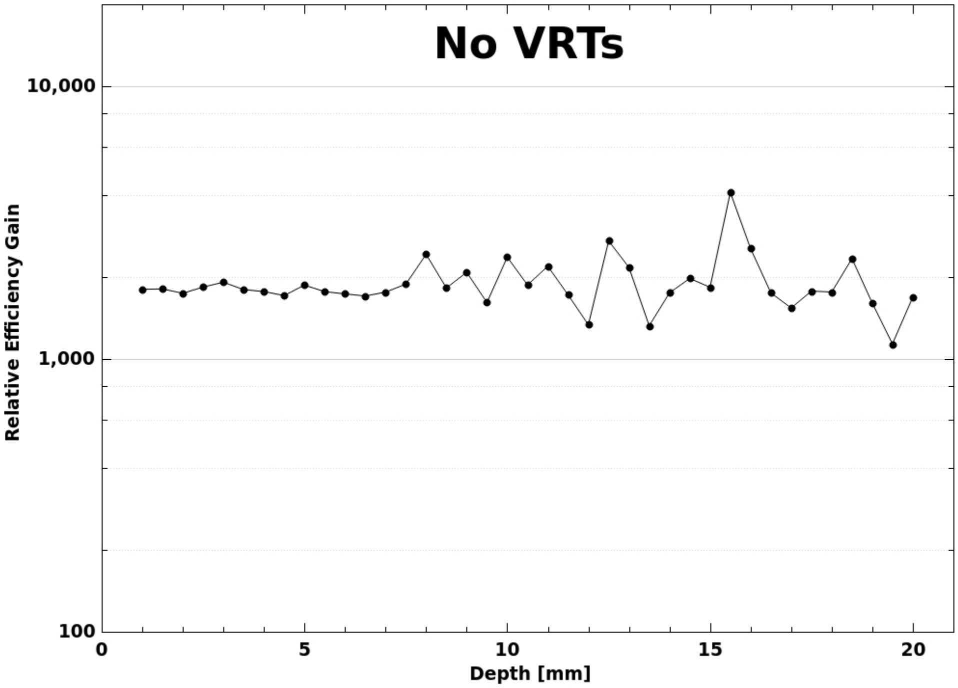

Figure 3.17 The same relative efficiency gain plot of figure 3.16 (on a single CPU core), but with all VRTs turned off.

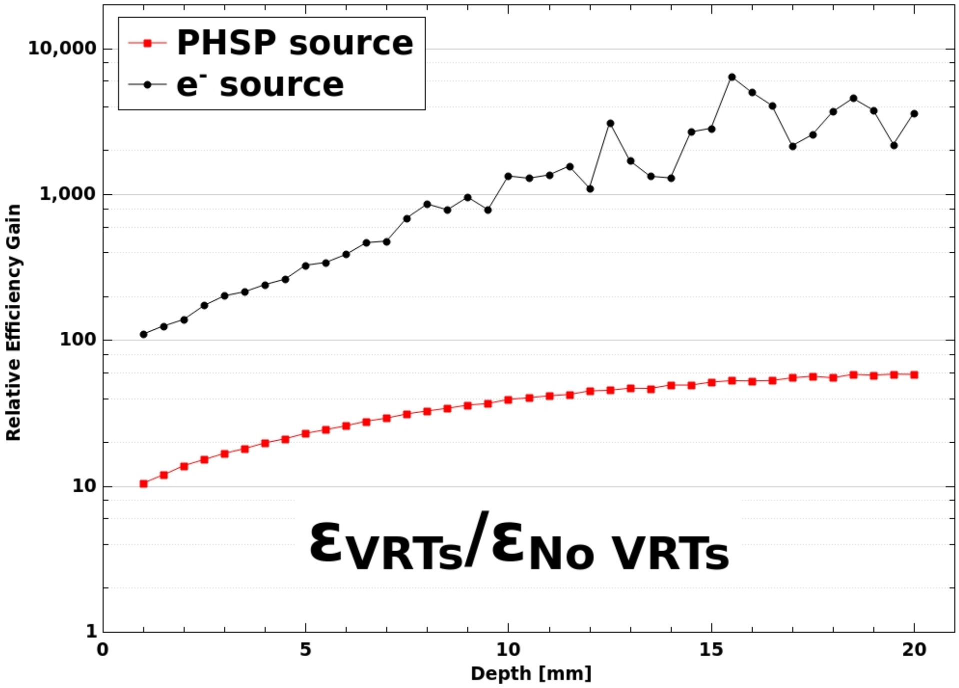

Figure 3.18 The relative efficiency gain in calculating the dose to water by using VRTs (IPSS, XCSE, and range-based RR) for a phase-space and electron source.

3.6 Conclusion

In this chapter, the basics of MC particle transport were introduced, followed by a summary of the EGSnrc particle transport code. A model of the INTRABEAM source with spherical applicators was created in EGSnrc based on specifications available in literature (Yanch and Harte, Nwankwo *et al.*) for the bare probe, and specifications provided by the manufacturer (Carl Zeiss Meditec AG) for the spherical applicators. These models were used to simulate photon fluence spectra, which were used to calculate the HVLs of the bare probe and spherical applicators. The simulation HVL results were compared with published values and found to agree within 6%, with the largest discrepancy for the bare probe. This agreement is outside of our estimated simulation uncertainties, however many of the reported HVLs were measured in a broad beam with different scatter conditions, and with the exception of Eaton and Duck (±0.04 mm Al), did not include a measurement uncertainty. Simulation results were also compared with HVL measurements performed with an INTRABEAM source at the McGill University Health Center. It was discovered that the presence of a lead collimator used to create narrow-beam geometry during HVL measurements introduced fluorescence photons ($L-$lines of Pb) which had a significant impact on the measured HVLs of the spherical applicators. Subsequent simulations of the spherical applicators were made to include the lead collimator, and a more detailed model of the applicators featuring a hollow air channel for inserting the INTRABEAM probe. By including the collimator and air channel, good agreement (less than 7.7% difference) was obtained between the measured and simulated HVLs, considering the experimental uncertainties of 4% to 21% (bare probe). For future measurements, a potential solution to remove the contaminant lead fluorescence photons would be to line the inside of the collimator with a low-Z material (i.e. plastic) to attenuate these photons.

The efficiency gain of using a phase-space source of the INTRABEAM probe over a full simulation starting with the electron beam was investigated. It was found that the efficiency in calculating the absorbed dose to a small volume of water in a water phantom could be increased by a factor of 20 to 190 by using a phase-space source. This efficiency gain was largest for a scoring region close to the INTRABEAM source probe, and decreased with depth in water. The depth dependence of the efficiency gain was determined to be caused by the VRTs used (IPSS, XCSE, and range-based RR), which were more effective at enhancing the efficiency deep in the water phantom for the electron source than the phase-space source.

4

Effect of explicit *M* and *N*-shell atomic transitions on a low-energy x-ray source

Peter G. F. Watson and Jan Seuntjens

Technical note published in: *Medical Physics* [6]

4.1 Preface

This chapter investigates the effect of considering explicit versus averaged M and $N-$subshell atomic transitions in MC simulations of the INTRABEAM source described in Chapter 3. Based on these findings, the simulation results in the later chapters all include explicit M and $N-$shell transitions.

4.2 Abstract

Purpose: In EGSnrc, atomic transitions to and from the M and N-shells are treated in an average way by default. This approach is justified in that the energy difference between explicit and average M and N-shell binding energies is less than 1 keV, and for most applications can be considered negligible. However, for simulations of low energy X-ray sources on thin, high-Z targets, characteristic X-rays can make up a significant portion of the source spectra. As of release V4-2.4.0, EGSnrc has included an option to enable a more complete algorithm of all atomic transitions available in the EADL compilation. In this article, the effect of M and N-shell averaging on the calculation of half-value layer (HVL) and relative depth dose curve (RDD) of a 50 kVp intraoperative X-ray tube with a thin gold target was investigated.

Methods: A 50 kVp miniature X-ray source with a gold target (The INTRABEAM System, Carl Zeiss, Germany) was modeled with the EGSnrc user code `cavity`, both with and without M and N-shell averaging. From photon fluence spectra simulations, the source HVLs were determined analytically. The same source model was then used with `egs_chamber` to calculate RDD curves in water.

Results: A 4% increase of HVL was reported when accounting for explicit M and N-shell transitions, and up to a 9% decrease in local relative dose for normalisation at 3 mm depth in water.

Conclusions: The EGSnrc default of using averaged M and N-shell binding energies has an observable effect on the HVL and RDD of a low energy X-ray source with high-Z target. For accurate modeling of this class of devices, explicit atomic transitions should be included.

4.3 Introduction

After the creation of a vacancy, an atomic ion will relax back to its ground state, whereby an electron from a higher atomic shell will make a transition to fill the vacancy. The energy difference between the initial and final electronic states is emitted via characteristic X-rays, and/or Auger, Coster-Kronig, or super Coster-Kronig electrons. In EGSnrc, atomic relaxations are modeled to include fluorescence from K, L, M, and N-shell transitions, as well as Auger and Coster-Kronig electrons. While the K and L-shells are considered explicitly, by default the transitions to and from M and N shells are treated in an average way [107]. This approach is justified by the fact that the energy difference between the average and explicit M and N-shell binding energies is relatively small (ex. for lead, the weighted average M-shell energy is 3.1 keV, while explicit M_I and M_V binding energies are 3.8 keV and 2.5 keV, respectively).

While the dosimetric effect of atomic relaxations in megavoltage photon beam simulations is minimal, they are important for accurate calculations of kilovoltage photon beams [137, 138]. There has been interest in using miniature x-ray sources for intraoperative radiotherapy [38, 99]. These devices operate at 50 kVp and have thin ($\sim \mu$m), high-Z targets, which leads to a significant contribution of characterstic X-rays to the source spectrum. Accurate modelling of atomic relaxations for these sources is therefore critical.

As of release V4-2.4.0 (March 2013), EGSnrc has included an option to perform a more complete algorithm of all atomic transitions available in the Livermore Evaluated Atomic Data Library (EADL) [124] compilation. In this algorithm, M and N-subshell binding energies are considered explicitly. This study investigates the effect of enabling this option on the half-value layer (HVL) and relative depth dose curve (RDD) of a 50 kVp X-ray tube with a thin gold target (The INTRABEAM system, Carl Zeiss, Germany).

4.4 Methods

4.4.1 In-Air: Photon fluence spectra and HVL

The INTRABEAM system (Carl Zeiss, Oberkochen, Germany), a 50 kVp miniature X-ray source with gold target, was modeled in EGSnrc using the egs++ geometry libraries. Source geometry and material specifications were taken from the literature [4, 5]. The emitted photon fluence spectra was calculated with the user code `cavity`. Fluence was scored across a circle of 1 cm diameter, situated 1 cm from the tip along the longitudinal axis of the source. The fluence was scored in 0.1 keV bins from 1 keV to 51 keV, and the photon and electron transport cutoffs were set to 1 keV. Simulations were performed both with and without M and N-shell averaging by setting the macro `$EADL_RELAX` to `.true.` in the `egsnrc.macros` file.

The source HVL was determined analytically from the simulated fluence spectra. First, photon fluence Φ in each energy bin i was converted to air-kerma by the relationship:

$$K_i = E_i \Phi_i \left(\frac{\mu_{en}}{\rho} \right)_{i,\mathrm{air}}, \tag{4.1}$$

where E is the photon bin energy, and $\left(\frac{\mu_{en}}{\rho} \right)_{\mathrm{air}}$ is the mass energy absorption coefficient for air. The air-kerma ratio was then calculated:

$$K_{\text{ratio}} = \frac{\sum_i K_i \exp(-\mu_{i,\text{att}} x_{\text{att}} - \mu_{i,\text{air}} x_{\text{air}})}{\sum_i K_i \exp(-\mu_{i,\text{air}} x_{\text{air}})}, \tag{4.2}$$

where μ_{att} and μ_{air} are the attenuation coefficients of the attenuator material and air, respectively. Similarly, x_{att} and x_{air} are the thicknesses of the attenuating material and air (source-to-detector distance). The attenuating material was chosen to be aluminum. All attenuation coefficients were obtained from the NIST XCOM database [116]. The HVL was determined to be the thickness of alumimum required such that $K_{\text{ratio}} = 0.5$. The uncertainty in HVL was estimated by error propagation of the statistical uncertainty of Φ_i across equation (6.12).

4.4.2 In-Water: Relative depth dose

Using the same source model as in Section 4.4.1, the `egs_chamber` user code was used to calculate an RDD curve in a cubic water phantom ($30 \times 30 \times 30$ cm^3). Dose was scored in a small cylindrical voxel of water ($r = 1.5$ mm, $h = 1$ mm), oriented along the source longitudinal axis. To create the RDD, the voxel was translated in 0.5 mm steps along this axis away from the source. To increase the efficiency of the simulation, all particles leaving the INTRABEAM source were written to a phase space file. This phase space file was then used as the particle source during the calculation of the RDD.

4.5 Results

4.5.1 In-Air: Photon fluence spectra and HVL

The photon fluence spectra calculated with and without M and N-shell averaging are presented in Figure 4.1. The effect of enabling all atomic transitions is evident with the introduction of new fluorescence peaks, which correspond to L-lines of gold. Interestingly, with explicit atomic transitions enabled, the KL_{II} and KL_{III} lines of chromimum (5.400 and 5.409 keV, respectively) were shifted to 5.368 and 5.377 keV, respectively. Due to the finite binning resolution, this energy difference of $\sim$0.03 keV appears as a 0.1 keV peak shift. This result suggests that in addition to including all atomic transitions, the EADL relaxation data also include updated K and L binding energies and transition probabilities. It was confirmed that the EADL binding energies differ somewhat from the EGSnrc default values (ex. 0.5% for tungsten). For this reason, the original relaxation implementation is left as the default until further testing can be done.[1] The KM-lines of chromium (5.97 keV) and nickel (8.27 keV), and the KL line of nickel (7.46 keV) were unchanged after enabling EADL relaxation data. It is worth mentioning that the atomic transition probabilities contained in the EADL are not without their uncertainties. While K-shell data is considered to be known to within 1%, L-shell data is uncertain by up to 20%, with even larger uncertainties for the higher shells. [124, 139]

The HVLs calculated with and without M and N-shell averaging were 0.0723 ± 0.0003 mm Al and 0.0750 ± 0.0001 mm Al, respectively. This represents a statistically significant increase of HVL by 0.0027 mm Al, or 4%, by including all M and N-shell transitions.

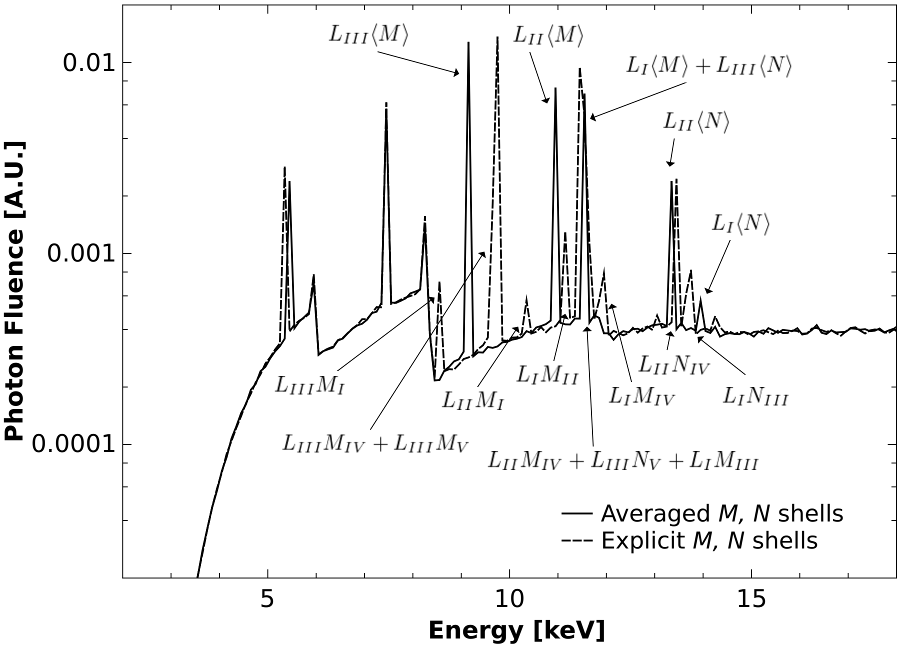

Figure 4.1 50 kVp photon fluence spectra from a thin gold target, calculated with and without M and N-shell averaging. The energy range of the x-axis was limited to focus on the gold L-shell fluorescence photons.

4.5.2 In-Water: Relative depth dose

The relative depth dose curves calculated with and without explicit atomic transitions are presented in Figure 4.2 (a). The curves were normalised by setting the the voxel dose at 3 mm depth in water

---

[1] Ernesto Mainegra-Hing, Personal Communication (25 Jan 2016)

to unity. Enabling complete atomic transitions leads to a decrease in relative dose, as shown in Figure 4.2 (b). The local percent difference in dose between the two curves increases as a function of depth in water, and can be as large as 9% at 20 mm. When looking at the unnormalised depth dose curves (Figure 4.2 (c)), it can be seen that the largest percent difference in absolute dose occurs at shallow depths, with good agreement at greater depths (Figure 4.2 (d)). The behaviour of the RDDs is contrary to what one would expect from the in-air result; where explicit treatment of the *M* and *N*-shells lead to an increase in HVL. This indicates an increase of photon effective energy (9.13 vs 9.02 keV), and suggests a more penetrating beam. However, for the same spectrum the RDD in water appears to be less penetrating.

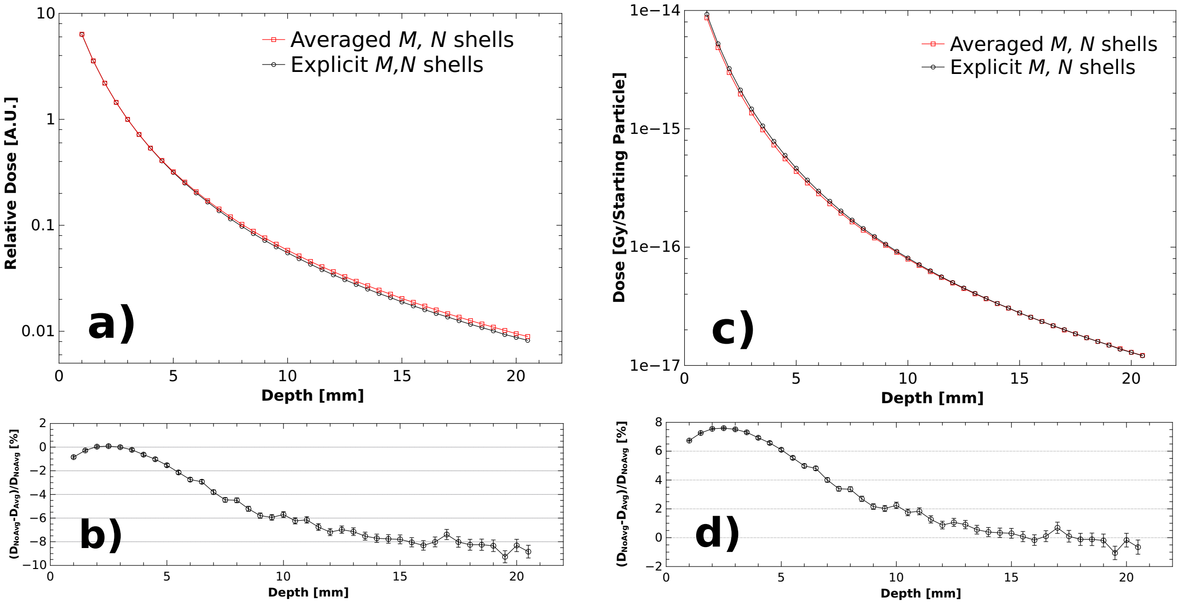

Figure 4.2 a) The effect of *M* and *N*-shell averaging on RDD. Curves were normalised to dose at 3 mm depth from source. b) Local percent difference between RDDs in a). c) The effect of *M* and *N*-shell averaging on absolute depth dose. d) Percent difference between depth dose curves in c). All error bars are estimated by the MC statistical uncertainty.

One feature of the percent difference curve in Figure 4.2 (b) is a local maximum near 2.5 mm depth. The relative increase in percent difference from 1 to 2.5 mm indicates that the RDD for *M* and *N*-shell averaging drops more steeply than the explicit atomic transitions RDD in this region. An explanation for this observation is that as the photons leave the source and pass through water, the low-energy portion of the spectrum is promptly attenuated (see Figure 4.3). If we only consider the photon fluence spectrum in the energy range containing characteristic

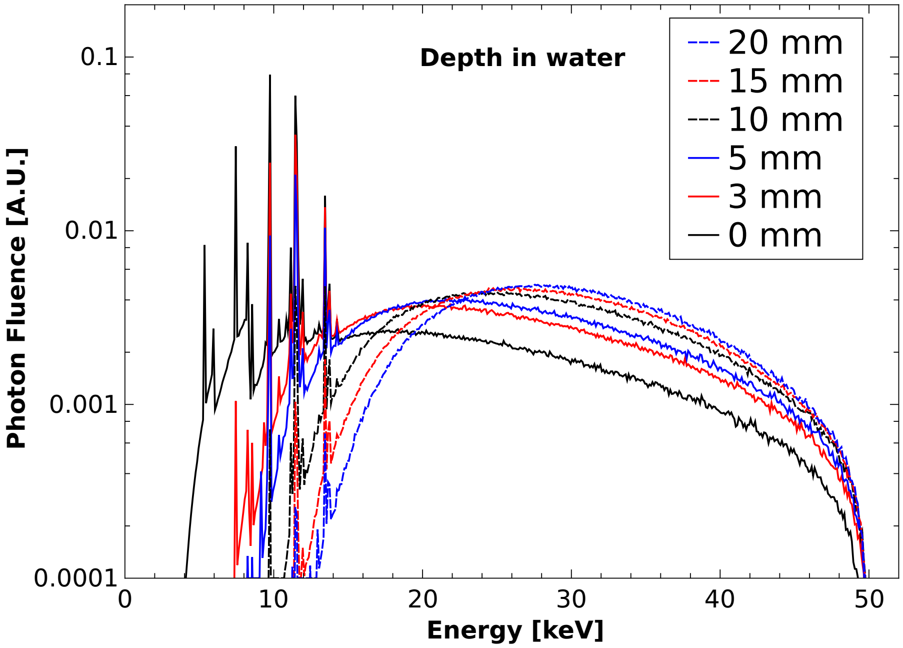

Figure 4.3 Normalised 50 kVp photon fluence spectra at various depths in water. Fluence was scored across a circular plane ($r = 0.5$ cm).

X-rays (below 15 keV), the spectrum with explicit transitions has a higher average energy than the spectrum without (9.90 vs 9.74 keV, respectively). As lower energy photons are attenuated more aggressively due to the photoelectric effect ($\sigma_{photo} \propto 1/E^3$), photon beam hardening occurs more rapidly as a function of depth in water for the averaged M, N-shell spectrum. Beam hardening is manifested in the RDD as curvature, and it is this larger RDD curvature of the averaged M, N-shell spectrum compared to the explicit atomic transitions spectrum that leads to a decrease in the relative depth dose. This result should act to remind us that HVL is not a unique beam quality indentifier for kilovoltage photon beams.

4.6 Discussion

For both in-air and in-water investigations, the uncertainty analysis was limited to the MC statistics of the calculated quantity (i.e. photon fluence, dose). For an absolute calculation of these quantities, such as for comparison with a different technique measuring the same quantity, a more complete estimation of uncertainty would be necessary. In-air, this would include the effect of energy bin width on photon fluence spectrum and attenuation coefficients, as well as the attenuation coefficient uncertainties. In-water, the effect of volume averaging and the influence of using a phase-space source in place of the full source model would need to be accounted for. However, for the purpose of studying the systematic effect of using explicit versus averaged M and N-shell transitions, a simple statistical estimate of uncertainty is adequate, as the effect will manifest in the same fashion.

Electronic brachytherapy with miniature kV X-ray sources has become increasingly popular worldwide [140]. MC simulations are involved in the development of treatment planning systems and dosimetry for these devices. The results of this study suggest that for accurate modelling of these devices, explicit atomic transitions should be included. The treatment of atomic transitions is also important for comparison between MC particle transport codes. It has been reported that spectral discrepancies have been observed in the modelling of an electronic brachytherapy source depending on the MC code (and code version) used, due in part to the number of explicit subshells considered [79, 141]. As well as low-energy x-ray sources, M and N-shell averaging would also affect the modelling of dose enhancement with gold nanoparticles, as the emission of Auger electrons and characteristic X-rays is one of the primary mechanisms for enhancing dose to surrounding tissue [142].

4.7 Conclusions

While the averaging of M and N-shell transitions during atomic relaxations in EGSnrc has long been considered benign for most applications in radiotherapy modelling, in simulations of a low-energy kV x-ray source with a thin, high-Z target, averaging has a considerable effect. A 4% increase of HVL is reported when accounting for explicit M and N-shell transitions from a 50 kVp X-ray source with a gold target. In water, the local percent difference between depth dose curves with and without M and N-shell averaging can be as large as 9% (Figure 4.2 (Bottom)). These results highlight the importance of including all explicit atomic transitions for accurate dosimetric calculations of low energy X-ray sources with high-Z targets.

4.8 Acknowledgments

We would like to thank Marc-Andre Renaud and Aidan Marchildon for adding phase space writing capability to egs++, and Ernesto Mainegra-Hing for providing details on the inclusion of EADL data in EGSnrc. P.W. acknowledges partial support by the CREATE Medical Physics Research

Training Network grant of the Natural Sciences and Engineering Research Council (Grant number: 432290).

5

Determination of absorbed dose to water from a miniature kilovoltage X-ray source using a parallel-plate ionization chamber

Peter G. F. Watson, Marija Popovic and Jan Seuntjens

Article published in: *Physics in Medicine and Biology* [48]

5.1 Preface

Here, a new dosimetry formalism for calculating the absorbed dose to water from the INTRABEAM is proposed. This formalism uses a chamber conversion factor, C_Q, which was calculated using the MC model of the INTRABEAM discussed in Chapters 3 and 4. This formalism is a direct determination of the dosimeter proportionality factor (f_Q), and does not require any of the assumptions of cavity theory.

5.2 Abstract

Electronic brachytherapy sources are widely accepted as alternatives to radionuclide-based systems. Yet, formal dosimetry standards for these devices to independently complement the dose protocol provided by the manufacturer are lacking. This article presents a formalism for calculating and independently verifying the absorbed dose to water from a kV x-ray source (The INTRABEAM System) measured in a water phantom with an ionization chamber calibrated in terms of air-kerma. This formalism uses a Monte Carlo (MC) calculated chamber conversion factor, C_Q, to convert air-kerma in a reference beam to absorbed dose to water in the measurement beam. In this work C_Q was determined for a PTW 34013 parallel-plate ionization chamber. Our results show that C_Q was sensitive to the chamber plate separation tolerance, with differences of up to 15%. C_Q was also found to have a depth dependence which varied with chamber plate separation (0 to 10% variation for the smallest and largest cavity height, over 3 to 30 mm depth). However for all chamber dimensions investigated, C_Q was found to be significantly larger than the manufacturer reported value, suggesting that the manufacturer recommended method of dose calculation could be underestimating the dose to water.

5.3 Introduction

Intraoperative radiation therapy (IORT) is a method of treating cancer where high doses of radiation are delivered to a surgical cavity and surrounding tissue during surgical intervention. To minimize the dose to healthy tissues beyond the target, a radiation beam with limited penetration depth is desired. Historically, IORT has been performed using electron accelerators (Shipley *et al.* 1984 [143], Merrick *et al.* 1997 [144]) or using kV photon-emitting radioactive sources (Nag *et al.* 1999 [145], Harrison *et al.* 1999 [146]). In the latter category, miniature kV x-ray generators have become available in recent years for this purpose (ex. The INTRABEAM system (Carl Zeiss Meditec AG, Jena, Germany), Xoft Axxent (iCAD Inc., Nashua, NH)). These devices offer a number of advantages over radioactive sources, such as portability, and reduced regulatory and shielding requirements.

The dosimetry of miniature kV x-ray sources is an area of active research. In 2014, a calibration primary standard for miniature kV x-ray tubes was established at the National Institute of Standards and Technology (NIST, USA), reporting the air-kerma rate at 50 cm in air (Seltzer *et al.* 2014 [78], Hiatt *et al.* 2016 [141]). From the air-kerma rate, the absorbed dose to water at a reference point can then be calculated using a modified version of the TG-43 protocol (DeWerd *et* *al.* 2015 [80]). To date, this standard has only been developed for the Xoft Axxent source. The calibration of the Zeiss INTRABEAM system is performed by the manufacturer, using their own absorbed dose "protocol", discussed further in section 5.3.1. A primary standard for realizing the absorbed dose to water for miniature kV x-ray sources has been under development at the National Metrology Institute of Germany (PTB, Germany), however this work is ongoing (Schneider and Šolc 2017 [84]).

This report proposes a methodology to accurately and independently verify the manufacturer reported absorbed dose to water from a miniature x-ray source, as measured in a water phantom with an air-filled ionization chamber. This method is based on the Monte Carlo (MC) calculation of ionization chamber response in the relevant photon beam quality. The formalism developed here provides a consistent approach in the calibration of different miniature x-ray sources, allowing for meaningful comparison between their dosimetry and dose accumulation from different radiation modalities (i.e. external beam radiotherapy).

5.3.1 The INTRABEAM system: source description, dosimetry, and QA

One of the most prevalent miniature x-ray systems is the INTRABEAM system (Carl Zeiss Meditec AG, Jena, Germany), which produces 50 $\mathrm{kV_p}$ x-rays in an approximately isotropic spatial distribution (Beatty *et al.* 1996 [39], Dinsmore *et al.* 1996 [38]). The x-ray generator accelerates electrons to 50 keV, where they are then drifted down an evacuated hollow cylindrical probe (100 mm length, 3.2 mm diameter) to strike a thin gold target, wherein bremsstrahlung and fluorescent photons are produced.

The factory calibration of the INTRABEAM system is performed in water using a soft x-ray ionization chamber (PTW 23342, Physikalisch Technische Werkstätte, Freiburg) calibrated in terms of exposure, and converted to absorbed dose to water with a conversion factor ($f = 0.881$ cGy/R). The dose at a reference depth is then related to a measurement made in air with the user's PTW 23342 chamber mounted in a QA tool (termed PAICH (Probe Adjuster/Ionization Chamber Holder)), allowing for daily output verification (Hensley 2017 [31]). Any small differences in daily output are accounted for by adjusting the treatment time (Schneider *et al.* 2014 [100]). While this QA system ensures that dose delivered by the INTRABEAM is reproducible, it does not provide a measure of absolute dose. For this purpose, Zeiss offers a special glass-walled water phantom with a PTW 34013 ionization chamber for measuring isotropy and depth dose curves. However, measurements in this water phantom require a depth-dependent correction function to compare with the calibration dose data (Carl Zeiss 2013 [103]). There is limited information available on this correction function, and it is not clear which (if any) of these measured doses is performed with reference to an absorbed dose standard (Hensley 2017 [31]). In this work, we investigate the measurement of absorbed dose to water using the Zeiss water phantom.

5.3.2 Zeiss water phantom dosimetry protocol

The Zeiss INTRABEAM water phantom is a self-shielded water tank in which the INTRABEAM source probe can be mounted and precisely positioned. The source is mounted on a 3-dimensional translational stage which can be positioned to within 0.1 mm (Carl Zeiss 2012 [147]). Measurements are performed with a PTW 34013 ionization chamber, situated at a fixed position in the water phantom inside one of two Solid Water$^{\text{TM}}$ waterproof holders (one for isotropy, one for depth dose measurements). A depth-dose curve can be generated by translating the source longitudinally away from the ionization chamber, and recording the collected charge at set depths.

To calculate dose to water, Zeiss provides their own dosimetry protocol. For the chamber charge reading at a depth z, dose to water $D_W(z)$ is calculated by:

$$D_W(z) = M(z) N_K k_Q k_{K_a \to D_W}, \tag{5.1}$$

where $M(z)$ is the measured charge (corrected for temperature and pressure), N_K is the ionization chamber calibration coefficient (calibrated in a T30 reference x-ray beam (HVL = 0.37 mm Al)), k_Q is the conversion factor from T30 to INTRABEAM beam quality (INTRABEAM is assumed to have the same beam quality as T30, i.e. $k_Q = 1$), and $k_{K_a \to D_W}$ is the conversion factor from air-kerma to dose to water for the chamber in a T30 beam ($k_{K_a \to D_W} = 1.054$) (Carl Zeiss 2012 [147]).

An important assumption in Eq.(5.1) is that the beam quality of INTRABEAM is considered the same as a T30 kV reference beam (HVL = 0.37 mm Al). However, it is well known that the HVL of the INTRABEAM source changes dramatically as a function of depth in water due to significant beam hardening (Beatty *et al.* 1996 [39], Armoogum *et al.* 2007 [135], Avanzo *et al.* 2012 [136], Watson and Seuntjens 2016 [6]). Figure 5.1 shows that the INTRABEAM HVL can vary from 0.08 mm Al to over 1.2 mm Al from the source surface to 20 mm depth in water. For reference, the ratio of mass energy absorption coefficients $(\bar{\mu}_{en}/\rho)_{water}/(\bar{\mu}_{en}/\rho)_{air}$ varies by up to 2.5% across this range of beam qualities.

Acknowledging this beam hardening, Eq.(5.1) then implicitly implies that the factors k_Q and $k_{K_a \to D_W}$ are relatively insensitive to the beam quality variations. To validate this assumption, we have proposed a dosimetry formalism based on the explicit MC calculation of the ionization chamber response for comparison.

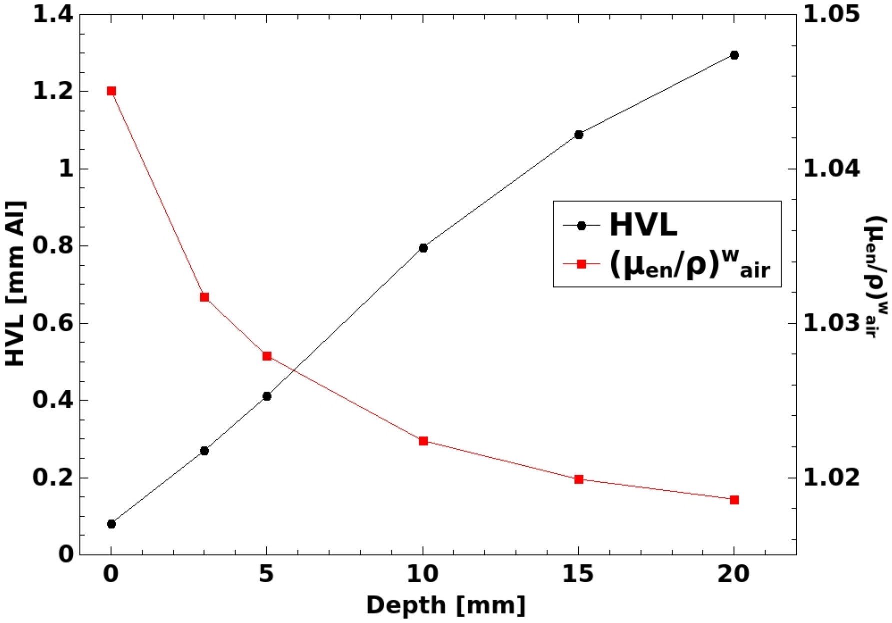

Figure 5.1 (Left axis) The HVL of the INTRABEAM source as a function of depth in water. (Right axis) The corresponding $(\bar{\mu}_{en}/\rho)_{water}/(\bar{\mu}_{en}/\rho)_{air}$ for the INTRABEAM photon spectra as a function of depth in water. Results were calculated using the EGSnrc model described in section 5.4.1

5.3.3 Proposed absorbed dose formalism

An absorbed dose formalism inspired by the work of Sarfehnia *et al.* (2010) [61] on Ir-192 dosimetry was derived for calculating dose to water with an ionization chamber calibrated in terms of air-kerma. During an air-kerma in air calibration with a reference beam of quality Q_0, the relationship between the chamber cavity absorbed dose calibration coefficient, N_{gas} and the air-kerma calibration coefficient N_K is:

$$\left(\frac{N_{\text{gas}}}{N_K}\right)^{Q_0} = \left[\frac{D_{\text{gas}}}{K_a}\right]^{Q_0}, \tag{5.2}$$

where D_{gas} is the dose scored in the chamber collecting volume, and K_a is the air-kerma in air at a point in the plane corresponding to the chamber effective point of measurement (POM).

Similarly, during measurements with a miniature X-ray source of beam quality Q in a water phantom, the relationship between chamber N_{gas} and $N_{D,w}^{Q}$ is:

$$\left(\frac{N_{\text{gas}}}{N_{D,w}}\right)^{Q} = \left[\frac{D_{\text{gas}}}{D_w}\right]^{Q}, \tag{5.3}$$

where now D_{gas} is the dose scored in the chamber collecting volume with the chamber in its waterproof holder, surrounded by water, and D_w is the dose to a point in water corresponding to the chamber effective POM. If we assume that N_{gas} is constant between beam qualities Q_0 and Q (this assumption is explored in the appendix), then by combining Eq.(5.2) and Eq.(5.3), we have an expression for the chamber absorbed dose to water calibration factor in beam quality Q, $N_{D,w}^{Q}$, in terms of $N_K^{Q_0}$:

$$\begin{aligned} N_{D,w}^{Q} &= \left[\frac{D_{\text{gas}}}{K_a}\right]^{Q_0}\left[\frac{D_w}{D_{\text{gas}}}\right]^{Q} N_K^{Q_0}, && (5.4)\\ &= C_Q N_K^{Q_0}. && (5.5)\end{aligned}$$

Here, C_Q represents the ionization chamber conversion factor from air-kerma in a reference beam Q_0 to absorbed dose to water for measurement beam Q, and is the product of two ratios which can be calculated by MC methods:

$$C_Q = \left[\frac{D_{\text{gas}}}{K_a}\right]^{Q_0}\left[\frac{D_w}{D_{\text{gas}}}\right]^{Q}. \tag{5.6}$$

From the definition of $N_{D,w}^{Q}$ (Andreo *et al.* 2000, Almond *et al.* 1999), the absorbed dose to water is then

$$D_W(z) = M(z)N_{D,w}^{Q} = M(z)C_Q N_K. \tag{5.7}$$

When compared directly with Eq.(5.1), we see that C_Q replaces the product of $k_Q k_{K_a \to D_W}$.

5.4 Materials and methods

5.4.1 Monte Carlo Simulations

An MC model of the INTRABEAM source and a parallel-plate ionization chamber (PTW 34013) has been developed. As MC ionization chamber response calculations are dependent on the accuracy of both the source and the detector models (Seuntjens *et al.* 2002 [148]), the INTRABEAM source model described here has been compared with measurements in-air (half-value layer) and in-water (percent depth dose), and the PTW 34013 chamber model with beam quality conversion factors reported by the calibration standard laboratory (PTW-Freiburg). The effect of the chamber plate separation tolerance has also been investigated.

Half-value layer and photon spectra

All MC simulations were performed using the EGSnrc particle transport code, Version 4-2.4.0 (Kawrakow *et al.* 2015 [107]) with the egs++ class library (Kawrakow *et al.* 2017 [128]). In addition to the default EGSnrc transport parameters, Rayleigh scattering was turned on and electron impact ionization using the cross sections of Bote and Salvat (2008) [133] was included. Bremsstrahlung events were modeled using NIST cross section data, and photon cross sections were calculated from the XCOM database (Berger *et al.* 2013 [116]) (excluding Compton events, where the EGSnrc default of relativistic impulse approximation with binding effects and Doppler broadening was used). Photons and electrons were transported down to 1 keV. Atomic relaxations were included, and were modeled with explicit M- and N-sub shell binding energies (Watson and Seuntjens 2016 [6]). Statistical uncertainties are reported as the standard error (1σ).

The INTRABEAM source was modeled based on the geometry and material specifications reported in two publications: the original paper of Yanch and Harte (1996) [4], and the more recent work of Nwankwo *et al.* (2013) [5]. The probe bodies of these two sources are quite similar; they both consist of an evacuated hollow nickel cylinder 3.2 mm in diameter (7.4 cm vs 9 cm long, respectively), with an inner diameter of 2.2 mm. The distal 1.6 cm end of the tube is beryllium in the place of nickel. The tip of the probe is hemispherical and contains a gold x-ray target, on which 50 keV electrons are incident. The outer surface of the probe is coated with thin layers of biocompatible materials. Table 5.1 lists the differences in gold target thickness, and biocompatible layer thicknesses and compositions between the two sources. The particle source used in simulations was a circular ($r = 1.1$ mm) parallel beam of monoenergetic 50 keV electrons.

The EGSnrc user code `cavity` was used to calculate the emitted source photon fluence spectrum, scored across a 1 cm diameter circular region situated 13 cm from the probe tip (the position of the ionization chamber during measurements) along the longitudinal axis of the source. This code makes use of a variance reduction technique called *forced detection*, where contributions from photons aimed at the scoring region are counted before they even cross the plane, while accounting for attenuation through any materials in their path. The fluence was scored in 0.1 keV bins from 1 to 51 keV. A cylindrical lead collimator present during the half-value layer (HVL)

Table 5.1 Comparison of INTRABEAM source parameters used in Monte Carlo simulations. Specifications taken from Yanch and Harte (1996) and Nwankwo *et al.* (2013).

Materials		Yanch and Harte [μm]		Nwankwo *et al.* [μm]
Target	Au	0.5		1.0
Body	Be	500.0		500.0
Biocompatible Layers	Ni	3.4	NiO	2.5
	Rh	0.4	Ni	2.5
	TiN	1.0	CrN	2.5

measurements was also included in the simulation, as it was found that fluorescence photons originating from the collimator had an effect on the fluence spectrum.

The source HVL was determined analytically from the simulated fluence spectra. Photon fluence Φ in each energy bin i was converted to air-kerma by the relationship:

$$K_i = E_i \Phi_i \left(\frac{\mu_{en}}{\rho}\right)_{i,\text{air}}, \tag{5.8}$$

where E is the photon bin energy, and $\left(\frac{\mu_{en}}{\rho}\right)_{\text{air}}$ is the mass energy absorption coefficient for air. The air-kerma ratio for an attenuated beam was then calculated, accounting for transmission through air and the ionization chamber entrance foil (PTW 23342):

$$K_{\text{ratio}} = \frac{\sum_i K_i \exp(-\mu_{i,\text{att}} x_{\text{att}} - \mu_{i,\text{air}} x_{\text{air}} - \mu_{i,\text{foil}} x_{\text{foil}})}{\sum_i K_i \exp(-\mu_{i,\text{air}} x_{\text{air}} - \mu_{i,\text{foil}} x_{\text{foil}})}, \tag{5.9}$$

where μ_{att}, μ_{foil} and μ_{air} are the attenuation coefficients of the attenuator material (aluminium), chamber entrance foil (polyethylene) and air, respectively. Similarly, x_{att}, x_{foil} and x_{air} are the thicknesses of the attenuating material, chamber entrance foil (0.03 mm per manufacturer specifications) and air (source-to-detector distance). All attenuation coefficients were obtained from the NIST XCOM database (Berger *et al.* 2013 [116]). The HVL is then the thickness of aluminium required to attenuate air-kerma by one half; $K_{\text{ratio}} = 0.5$. The uncertainty in simulated HVL was estimated by error propagation of the statistical uncertainty of Φ_i, and the uncertainty of the XCOM attenuation coefficients, taken to be 2% (Hubbell 1999 [130]), across Eq.(6.12).

Percent depth dose curve

To validate the INTRABEAM model in water, depth dose calculations in a water phantom were simulated using a modified version of the user code `egs_chamber`. The same INTRABEAM source model as described in Section 5.4.1 was used, situated with the probe tip at the center of a cubic water phantom ($30 \times 30 \times 30$ cm^3). Dose was scored to the air cavity of a PTW 34013 parallel-plate ionization chamber, which was modeled according to design specifications provided by the manufacturer. A waterproof chamber holder composed of Solid Water$^{\mathrm{TM}}$ present during measurements was also included in the model. To create the depth dose curve, the chamber was translated in 0.5 mm increments along the longitudinal axis of the source. The effective point of measurement (POM) of the chamber was defined to be the inside of the chamber entrance foil, as specified by Zeiss.

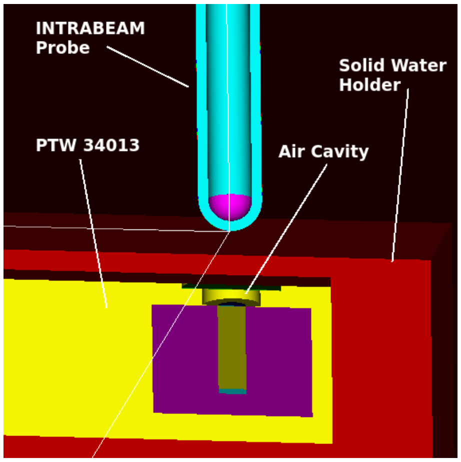

Figure 5.2 Rendering of INTRABEAM source with PTW 34013 ionization chamber inside its waterproof holder.

The `egs_chamber` user code (Wulff *et al.* 2008 [149]) features a number of variance reduction techniques (VRTs), two of which were employed:

- Intermediate phase-space storage across a region encompassing all ionization chamber positions, and
- Photon cross-section enhancement in and around the ionization chamber geometry.

In addition to the aforementioned VRTs, uniform bremsstrahlung splitting (where N photons are generated at each bremsstrahlung interaction) was implemented in `egs_chamber` to increase the simulation efficiency of the INTRABEAM x-ray source (Mainegra-Hing and Kawrakow 2006 [150]). Shortly after implementation, however, it was noted that interactions by fluorescent photons lead to large fluctuations in variance due to their relative weight compared to split bremsstrahlung photons. To remedy this, a uniform fluorescence splitting routine was implemented so that split bremsstrahlung and fluorescent events had identical weights. To further increase efficiency, electrons were only transported while inside the INTRABEAM source probe or ionization chamber/waterproof chamber holder geometry.

Ionization chamber beam quality conversion factor

To decouple the validation of the PTW 34013 ionization chamber model from the INTRABEAM source model, we simulated the chamber k_Q factor in various reference kilovoltage photon beam qualities as provided by the calibration service at the National Metrology Institute of Germany (PTB, Germany). The calculated k_Q values could then be compared with those reported on the chamber calibration certificate from PTW. Here, k_Q for beam quality Q (normalised to T30 beam quality) is defined as:

$$
\begin{aligned}
k_Q &= \frac{N_K^Q}{N_K^{T30}}, &\quad (5.10)\\
&= \left[\frac{D_{\text{gas}}}{K_a}\right]^{T30}\left[\frac{K_a}{D_{\text{gas}}}\right]^{Q} &\quad (5.11)
\end{aligned}
$$

where D_{gas} is the dose scored in the chamber collecting volume, and K_a is the air-kerma at a plane corresponding to the chamber effective POM. To calculate these values, an EGSnrc simulation was created to reproduce the geometry during chamber calibration as specified on the calibration certificate. A source-to-detector distance of 50 cm, with a circularly collimated photon beam 3 cm in diameter at 50 cm was used. The photon source spectra were T-series reference kilovoltage x-ray spectra, measured at PTB (figure 5.3). The air-kerma, K_a, crossing a circular plane ($r = 0.5$ cm) corresponding to the position of the entrance window of the ionization chamber during calibration was scored using `cavity`. The dose to the chamber air cavity, D_{gas}, was calculated using `egs_chamber`, using the same geometry as the air-kerma calculation, only with a full model of the PTW 34013 ionization chamber present.

Incidentally, the provided T-series spectra were measured at a source-to-detector distance of 30 cm rather than 50 cm. To account for the additional air attenuation and scatter in the spectra from traversing an extra 20 cm in air, our simulation geometry consisted of 30 cm of vacuum and

20 cm of air from the photon source to the detector. Downstream from the detector, a 1 m thick slab of air was placed to account for any air backscatter.

When first modeling the PTW 34013 ionization chamber, it was noted that the manufacturer reported tolerance on the plate separation of the chamber cylindrical air cavity appeared to be significant. To assess the effect of this cavity height variation, three models of the chamber were used to calculate D_{gas}; two modeled with the maximum/minimum height tolerance (hereby referred to as *thick* and *thin*, respectively), and one with the nominal height. The exact dimensions of the cavity are not included in this report as they are proprietary information. Due to the fact that this chamber is not guarded, the collector diameter is not known accurately enough to determine the plate separation from a capacitance measurement.

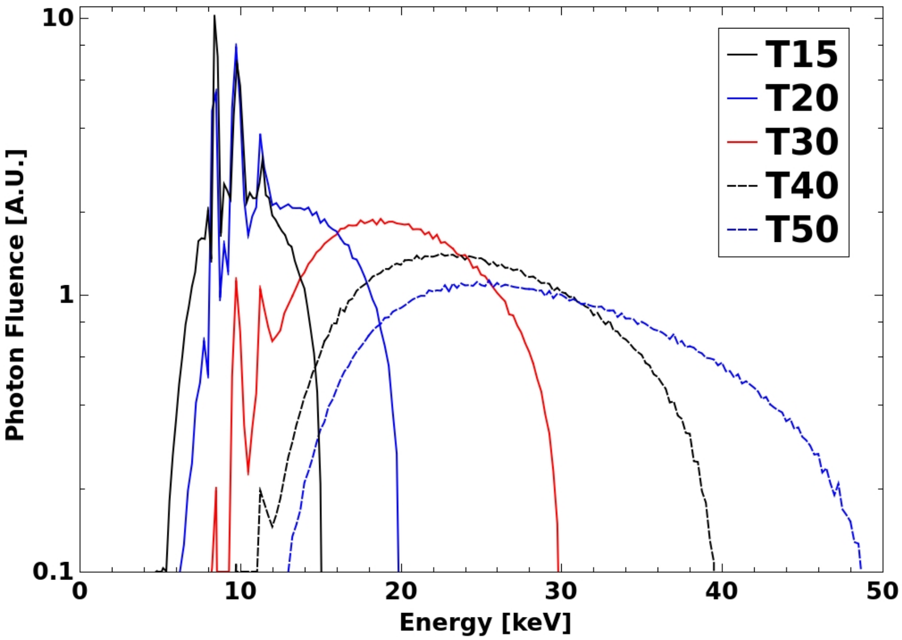

Figure 5.3 T-series kV reference photon beam spectra provided at PTB. These spectra were measured in air at 30 cm source-to-detector distance. Courtesy of Ludwig Büermann.

5.4.2 Measurements

HVL

Attenuation measurements of the INTRABEAM source were performed by placing various thicknesses of high purity aluminium foils in between the source and a PTW 23342 soft x-ray parallel-plate ionization chamber during irradiation. As the INTRABEAM is a nearly isotropic source, beam collimation was performed by placing a cylindrical lead collimator (1 mm lead sheet wrapped around a hollow polyethylene cylinder used to protect source during transportation, 16 cm length and 3.5 cm diameter) around the source. The aluminium attenuators (0.05 to 0.3 mm thick) were positioned at the exit of the collimator, 8 cm from the source. The PTW 23342 chamber was positioned in line with the source probe and center of the collimator using a laser ruler. Due to the small collecting volume of the ionization chamber (0.02 cm^3) and relatively low source output, the source-to-chamber distance of 1 m as recommended by TG-61 (Ma *et al.* 2001 [54]) was found to give an insufficient signal during irradiation. A suitable signal was obtained by placing the chamber 13 cm from the source.

An attenuation curve was calculated by measuring the collected charge during a 60 s irradiation, normalised to the reading with no aluminium attenuator present. Measurements were repeated three times for each thickness of aluminium, and the mean value μ and standard deviation σ were calculated. To minimize systematic effects in source output, the attenuation measurements were performed in random order (i.e. not monotonically increasing/decreasing thicknesses).

The HVL was determined by fitting a function of the form $f(x) = ae^{-bx} + ce^{-dx}$ to the attenuation curve, and solving for the thickness which attenuated the open beam signal by half. This was done in MATLAB R2013b (The MathWorks, Inc., Natick, MA) using the function `fit`, with $1/\sigma^2$ as weights. The 95% confidence interval of the fitted curve at the HVL was estimated by the function `predint` for a new observation at a single predictor value. The total uncertainty in the HVL measurement was estimated to be the quadrature sum of the fitted confidence interval and the quoted tolerance of the aluminium foil thickness (assuming rectangular distribution).

Percent depth dose curve

Percent depth dose (PDD) curve measurements were made in a Zeiss water phantom with a PTW 34013 parallel-plate ionization chamber connected to a UNIDOS electrometer. To determine the source-to-detector distance (defined as the distance from the probe tip to the chamber entrance foil) the probe tip was precisely positioned in the X, Y, and Z directions following the zeroing procedure recommended in the water phantom manual (Carl Zeiss 2012 [147]). Measurements were performed by recording the collected charge during a 60 s irradiation at depths ranging from 2 mm to 20 mm in increments of 0.5 mm to 1 mm. Measurements were repeated three times for each depth in water, and the mean value and standard deviation were calculated.

5.4.3 Determination of absorbed dose to water

Ratio of $[D_{\mathbf{gas}}/K_a]$

The geometry of the ionization chamber calibration set-up at PTW was reproduced as previously described in Section 5.4.1. The air-kerma at the chamber entrance window, K_a, and dose to the chamber air cavity, D_{gas}, were calculated for a variety of T-series reference kilovoltage photon spectra offered at PTW (traceable to PTB, see figure 5.3). From these results, the ratio of $[D_{\text{gas}}/K_a]$ was computed.

Ratio of $[D_w/D_{\mathbf{gas}}]$

As in Section 5.4.1, the INTRABEAM source was modeled in `egs_chamber` and positioned with the source tip at the center of a cubic water phantom ($30 \times 30 \times 30$ cm^3). The dose to a small volume of water, D_w, was calculated for incremental distances away from the source (position referenced to centroid of volume). For a depth dose curve, the size of an appropriately "small" volume of water is dependent on the curvature (i.e., the second order derivative) of the depth dose curve (Kawrakow 2006 [151]). An infinitesimally small volume would naturally satisfy this criteria, however, for efficient MC scoring statistics it is advantageous to make the "small" volume as large as possible. We evaluated a variety of cylindrical water voxel sizes, ranging from 0.1 to 1 mm in diameter & height. It was found that in the calculation of depth dose, beyond a depth of 3 mm in water there was convergence between all voxel dimensions investigated to within statistical uncertainties. A cylindrical water voxel of 0.4×0.4 mm^2 (diameter × height) was ultimately chosen as the optimal dimension to satisfy "'smallness" and sufficient statistics.

To calculate D_{gas}, dose was scored to the air cavity of a PTW 34013 parallel-plate ionization chamber (inside waterproof chamber holder) placed in the water phantom with the INTRABEAM source. The chamber was translated in 0.5 mm increments along the longitudinal axis, away from the source. The chamber effective POM was taken to be the inside of the entrance foil, as recommended by Zeiss. The effect of shifting the POM to the chamber air cavity centroid (as recommended by TG-61 (Ma *et al.* 2001 [54])) was investigated.

5.5 Results

5.5.1 MC model validation

Half-value layer and photon spectra

The simulated INTRABEAM 50 kV_p photon spectra are shown in figure 5.4 for both source models listed in table 5.1. These spectra qualitatively agree with previously published simulation results using ITS (Yanch and Harte 1996 [4]) and GEANT4 (Nwankwo *et al.* 2013 [5]); and spectral measurements (Ebert and Carruthers 2003 [152], Yanch and Harte 1996 [4]). The fluorescent lines at 2.8 and 20.2 keV in the Yanch and Harte spectra are due to the presence of rhodium, and the peaks at 4.5 and 4.9 keV are from titanium not present in the Nwankwo *et al.* source. Likewise, the lines at 5.4 and 5.9 keV in the Nwankwo *et al.* source are from its chromium content. The shared peaks in both spectra are K-lines of nickel (7.5 and 8.3 keV) and L-lines of gold. The variation in the bremsstrahlung portion of the spectra is due to the difference in gold target thickness between the two source models.

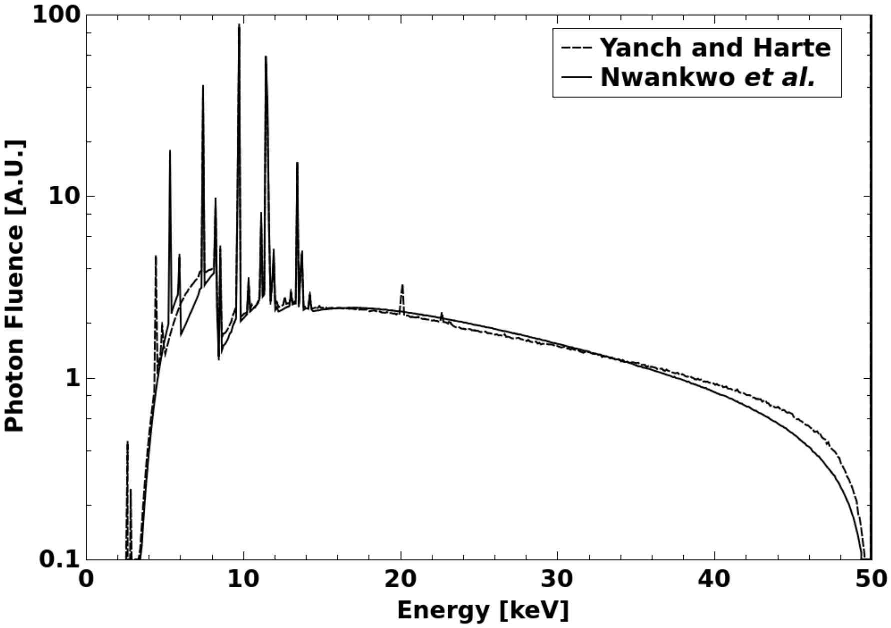

Figure 5.4 Simulated INTRABEAM 50 kV_p photon spectra in air for source model parameters taken from Yanch and Harte (see table 5.1) and Nwankwo *et al.*. Spectra are normalised to the area under the curve.

The HVLs calculated from the simulated spectra using Eq.(6.12) were 0.0720±0.0006 mm Al and 0.0722±0.0005 mm Al for the Nwankwo *et al.* and Yanch and Harte sources, respectively. As can be seen, there is excellent agreement between the two HVLs despite the differences in the source model materials and geometries. The source HVL determined via the measured attenuation curve was 0.078±0.016 mm Al (0.006 mm Al from fit confidence, 0.014 mm Al from foil thickness tolerance). This value agrees with our simulation results well within uncertainty. Compared with previously reported source HVLs (0.10 mm Al (Beatty *et al.* 1996 [39]) and 0.11 mm Al (Armoogum *et al.* 2007 [135])), our measured value is somewhat smaller, however these earlier measurements were performed with an uncollimated broad beam, leading to a larger contribution from scatter.

Percentage depth dose curve

The simulated percentage depth dose curves for the INTRABEAM sources were calculated for the PTW 34013 ionization chamber, normalised to a depth of 5 mm. Figure 5.5 shows the measured PDD along with simulated results for both a bare ionization chamber and chamber inside the Zeiss water phantom waterproof holder (the actual measurement condition). As can be seen, there is good agreement between the PDDs of the Yanch and Harte, and Nwankwo *et al.* sources. The simulated PDDs agree well with measurement also, with differences less than 2.4% beyond 5 mm depth observed. The inclusion of the waterproof holder in the MC models was found to improve the agreement with the measured data. For the remainder of this work, the INTRABEAM source model parameters as described by Nwankwo *et al.* were used for calculations.

Ionization chamber beam quality correction factor

The PTW 34013 ionization chamber beam quality correction factor, k_Q, was calculated according to Eq.(5.11) for T15, T20, T40, and T50 reference kV photon spectra. The investigated chamber cavity plate separation tolerance lead to slightly different values of k_Q, differing by up to 2.5% in the T15 beam quality. Figure 5.6 plots the simulated k_Q values for the chamber along with values reported in the calibration certificates for two separate PTW 34013 ionization chambers (SN000235 and SN000429). At T15 beam quality, the two measured k_Q values span the range of our simulation results, to within the reported 2% uncertainty. However, at T50 beam quality we see an increasing trend in k_Q for all of our simulated values when compared to measurement, with differences as large as 3%. A similar discrepancy between measured and simulated k_Q values

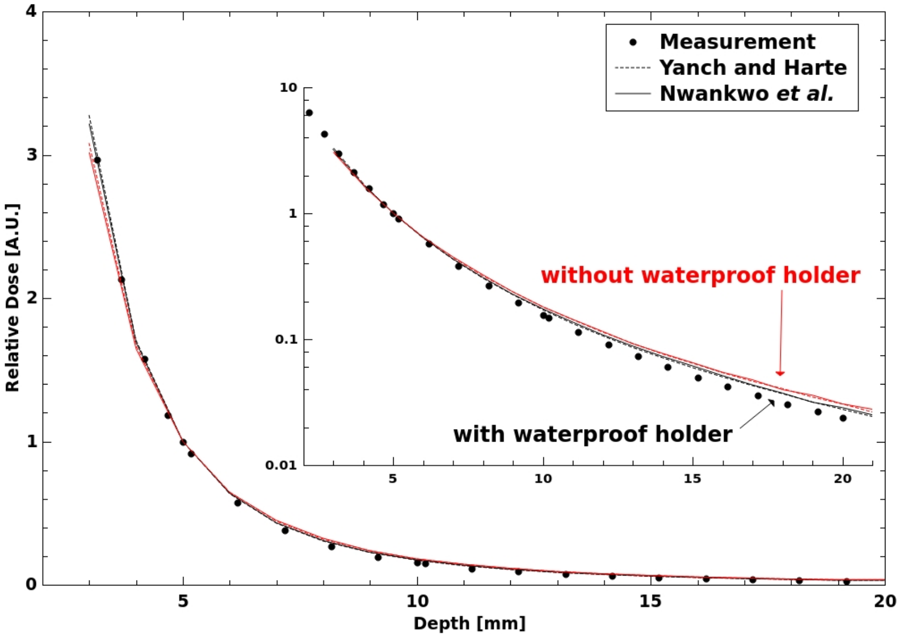

Figure 5.5 Measured and simulated percentage depth dose curves in water for the Zeiss INTRABEAM, normalised at 5 mm depth (inset shows log scale). The simulated PDDs were calculated with both the Yanch and Harte, and Nwankwo *et al.* source models. The effect of the presence of the waterproof chamber holder can be seen.

for the PTW 34013 ionization chamber was reported by Pike (2012)[1] [153], who found a 4.5% difference between the measured and EGSnrc calculated k_Q values at similar beam qualities. They attributed this discrepancy to difficulties in modeling the chamber and large measurement uncertainties.

5.5.2 Determination of absorbed dose to water

Ratio of $[D_{\mathbf{gas}}/K_a]$

The ratio $[D_{\text{gas}}/K_a]$ is shown in figure 5.7. The variation of this ratio as a function of photon beam quality is essentially the chamber energy dependence, which was found to be dependent on the chamber cavity height (variation of 2.2% for “thin” cavity versus 5.4% for “thick” across beam qualities investigated). The ratio was shown to decrease with an increase in mean photon energy,

---

[1] Pike used UW30-M (HVL = 0.36 mm Al) and UW50-M (HVL = 1.02 mm Al) beams, compare with T30 (HVL = 0.37 mm Al) and T50 (HVL = 1.00 mm Al).

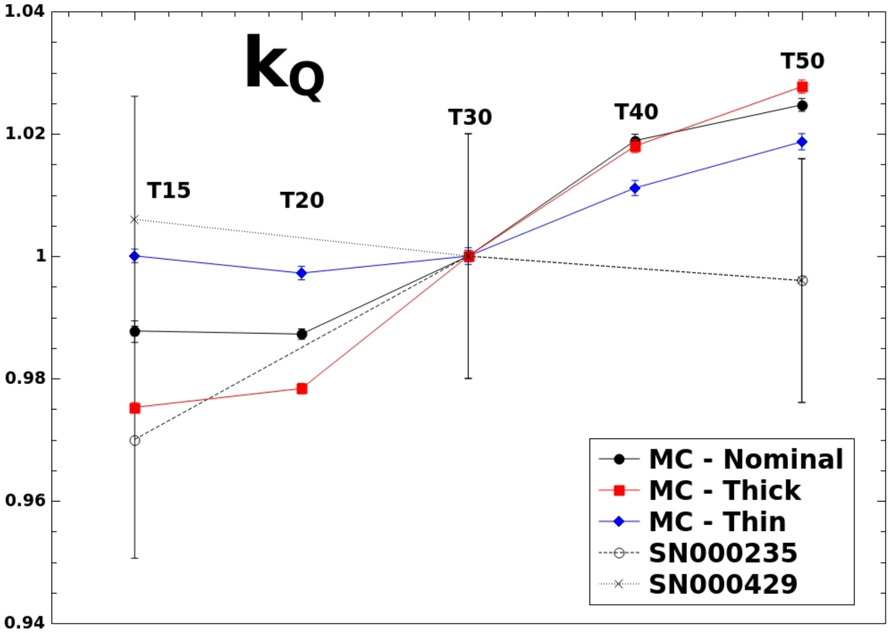

Figure 5.6 Simulated and measured PTW 34013 ionization chamber k_Q values in T-series kV reference beams. Measured values were taken from the calibration certificates (PTW, Germany) of two individual chambers (SN000235 and SN000429). Measurement uncertainty was reported as 2%.

which can be attributed to a reduction in contribution to D_{gas} from photo/auger electrons off of the aluminium collecting electrode, and an increase in the range of secondary electrons which are able to leave the air cavity before depositing all their energy. As the chamber cavity height was increased (the “thin” vs “thick” chamber models), the ratio was found to decrease, most likely due to the influence of scattered photons.

Ratio of $[D_w/D_{\text{gas}}]$

The ratio of $[D_w/D_{\text{gas}}]$ as a function of distance away from the source is shown in figure 5.8 (top). As in-air, D_{gas} was found to increase as cavity height decreases, however the effect was much more dramatic with up to a 23% difference between tolerance extremes at 3 mm depth. This enhancement in sensitivity to chamber cavity dimension is due to the significant dose volume averaging for the larger cavity, particularly in close proximity to the source where dose gradient is steepest (∼40%/mm). The chamber cavity height was also found to affect the depth dependence

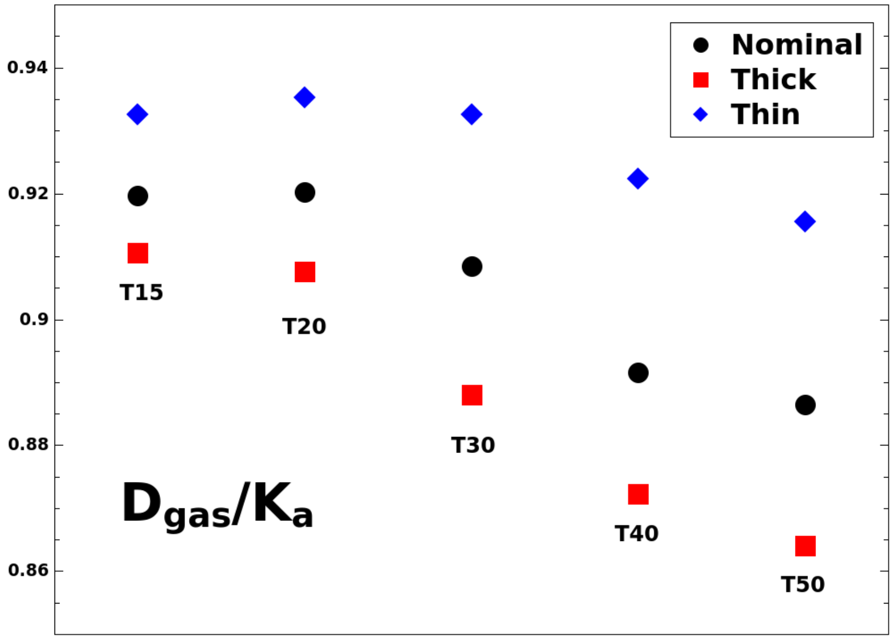

Figure 5.7 Ratio of $[D_{\text{gas}}/K_a]$ for PTW 34013 ionization chamber in kV reference beam qualities.

of the dose ratio. The thin cavity exhibited virtually no variation in $[D_w/D_{\text{gas}}]$ with depth (within $\pm 2\%$ for depth ≤ 20 mm), while the thick cavity ratio decreased by over 10% from 3 to 30 mm.

The effect of shifting the chamber effective POM to the centroid of the cavity on $[D_w/D_{\text{gas}}]$ was investigated, as presented in figure 5.8 (bottom). By using the center of the cavity as POM, the large variation in $[D_w/D_{\text{gas}}]$ seen in figure 5.8 (top) due to cavity dimension tolerance is greatly mitigated, with the curves crossing over near 5.5 mm depth. However, the depth dependence of the dose ratio is much larger, varying by more than 20% from 3 to 17 mm.

It is worth mentioning that while we reference the outer surface of the INTRABEAM probe tip as $z = 0$, the true photon source position exists somewhere on the gold target, approximately 0.8 mm into the source probe (Schneider 2017 [154]). While the position of this effective photon source is important for certain calculations (i.e. applying an inverse square correction), it is implicitly accounted for in our formalism, as our INTRABEAM model starts with electrons striking the gold target and not merely a photon point source.

The sensitivity of $[D_w/D_{\text{gas}}]$ to the choice of INTRABEAM source model was investigated by repeating the calculations of section 5.4.3 with the source model based on the specifications of Yanch and Harte (see figure 5.9). It was determined that there were no statistically significant differences in absorbed dose ratios between these two source geometries.

Chamber conversion factor C_Q

The ionization chamber conversion factor, C_Q, was calculated according to Eq.(5.6) using the T30 reference beam value of $[D_{\text{gas}}/K_a]$. The results, shown in figure 5.10 (top), reveal that the effect of chamber cavity height tolerance on D_{gas} is partially canceled out due to the different dose gradients and scatter conditions between the in-air and in-water simulations. At 3 mm depth in water, a 15% difference is observed in C_Q between the thinnest and thickest cavity tolerances. This difference decreases with increasing depth in water, with some convergence within statistical uncertainties beyond 20 mm. However, for all cavity dimensions investigated C_Q was larger than the manufacturer reported value of 1.054, suggesting a significant underestimation of absorbed dose to water using the Zeiss method of Eq.(5.1) and emphasizing the need for independent international recommendations.

Figure 5.10 (bottom) shows the effect of defining the center of the chamber cavity as the effective POM on C_Q. As with the ratio of $[D_w/D_{\text{gas}}]$ (see figure 5.8 (bottom)), there exists a larger depth dependence of C_Q with this POM. However, beyond 10 mm depth there appears to be a convergence for all chamber cavity dimensions toward a value in good agreement with the reported quantity of 1.054. This would seem to be coincidental however, as the manufacturer prescribes the chamber entrance foil as the point of measurement, not the cavity midpoint.

5.6 Discussion

Our results suggest that by using the cavity midpoint of the PTW 34013 ionization chamber as the effective POM, we can mitigate the variance in C_Q introduced by the cavity dimension tolerance of the chamber (at the expense of increasing the depth dependence of C_Q close to the source probe). However, we encounter a circular dilemma in that due to the large uncertainty in cavity height, we cannot accurately determine the cavity midpoint. As well, the geometry and construction of the PTW 34013 chamber cavity is neither an ideal cylinder nor ideal parallel-plate capacitor (unguarded), severely limiting a capacitive measurement of electrode separation/cavity height. As such, the entrance foil remains the most practical reference point for this ionization chamber. We are not the first to report difficulties with this chamber. Issues with modeling and performing measurements with the PTW 34013 in the context of electronic brachytherapy have been previously reported (Rivard *et al.* 2006 [99], Pike 2012 [153], Fulkerson *et al.* 2014 [155]). It is recommended that alternative soft x-ray ionization chambers with desirable qualities such as a more precise knowledge of dimensions, inclusion of a guard ring, and waterproof construction (i.e. Exradin A20) be investigated and considered for use.

While this report focuses on the dosimetry of the Zeiss INTRABEAM, the proposed dose formalism of Eq.(5.7) is generalizable and can be applied to any kilovoltage x-ray source and ionization chamber calibrated in terms of air-kerma. It only requires a validated MC model of the photon source in question and ionization chamber to calculate C_Q. Provided with the appropriate spectra, the ratio of $[D_{\text{gas}}/K_a]$ can be calculated for any kV reference beam, allowing for ionization chamber calibration at various ionizing radiation standards laboratories.

5.7 Conclusion

A formalism for calculating the absorbed dose to water from an x-ray source with an ionization chamber calibrated in terms of air-kerma has been proposed. This formalism relies on a MC-derived chamber conversion factor, C_Q, which is calculated with knowledge of the reference and measurement photon beam qualities, and detailed ionization chamber geometry and materials. In this report we investigated the measurement of dose to water for the INTRABEAM source with a PTW 34013 parallel-plate ionization chamber in a water phantom.

Our results show that the cavity dimension tolerance of the PTW 34013 chamber has a significant effect on the value of C_Q, with differences of up to 15% at 3 mm depth in water. The depth dependence of C_Q was also found to vary with chamber cavity height, with insignificant variation for the smallest plate separation, to $\sim$10% variation over 3 to 30 mm depth for the largest separation. For all chamber dimensions investigated, C_Q was found to be larger than the manufacturer reported value of $k_{K_a \to D_W} = 1.054$, suggesting that the recommended method of dose calculation could be underestimating the dose to water by as much as 23% (largest chamber plate separation at 3 mm depth).

It was found that by shifting the chamber effective POM to the cavity midpoint rather than the inside of the entrance foil, the effect of the cavity dimension tolerance on C_Q was greatly reduced. This shifted POM also leads to a C_Q which coincidentally agreed well with the manufacturer reported value (beyond a depth of 10 mm). However, due to the large uncertainty in plate separation, the cavity midpoint cannot accurately be determined, rendering this POM impractical. It is recommended that another soft x-ray ionization chamber with more precise geometry knowledge be investigated for this purpose.

5.8 Acknowledgments

P.W. would like to thank J. Würfel of PTW for providing details of the PTW 34013 chamber, M. Benker of Carl Zeiss for details on the INTRABEAM water phantom, and L. Büermann of PTB for the T-series spectra. P.W. would also like to thank M.A. Chamberland and the authors of `egs_brachy` for their assistance in implementing uniform fluorescence splitting in `egs_chamber`. M.A. Renaud provided indispensable help with editing the `egs_chamber` code. P.W. acknowledges partial support by the CREATE Medical Physics Research Training Network grant of the Natural Sciences and Engineering Research Council (Grant No. 432290).

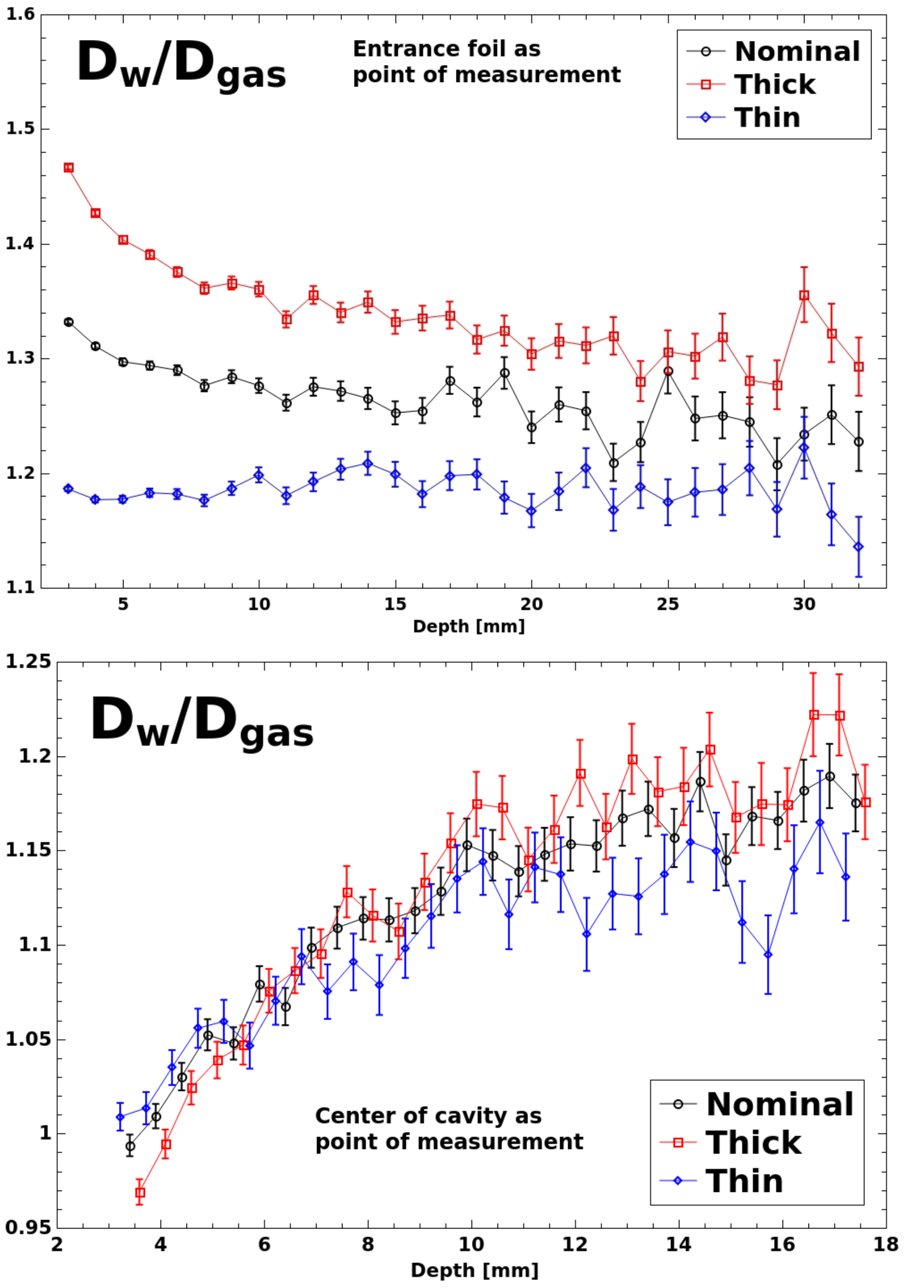

Figure 5.8 (Top) Ratio of $[D_w/D_{\text{gas}}]$ for PTW 34013 ionization chamber with INTRABEAM source in water. The chamber effective point of measurement was defined as the inside of the entrance foil, or (Bottom) the air cavity centroid.

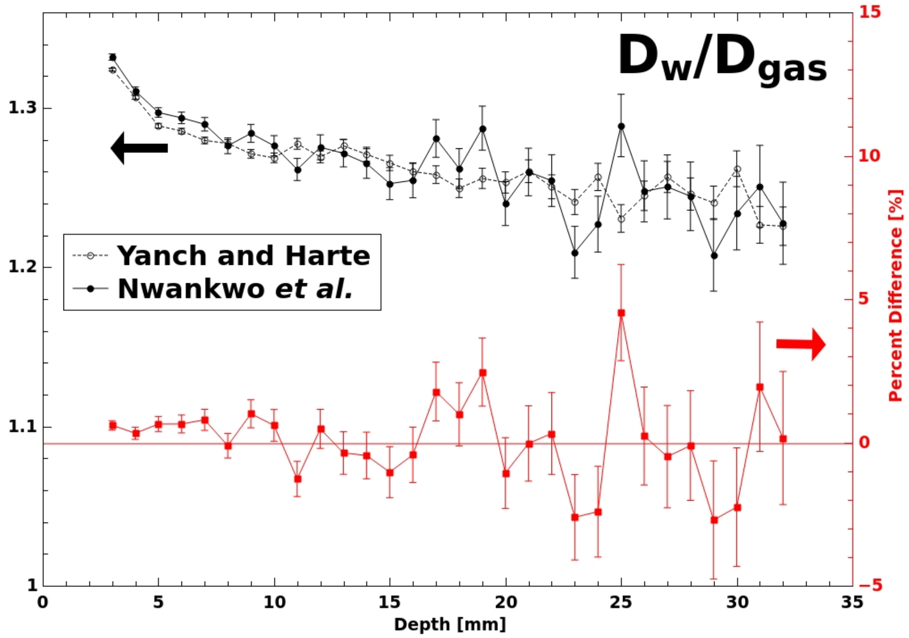

Figure 5.9 Comparison of the ratio of $[D_w/D_{\text{gas}}]$ calculated with the Yanch and Harte, and Nwankwo *et al.* INTRABEAM source models for a PTW 34013 chamber with nominal plate separation. Both curves agree well within uncertainties.

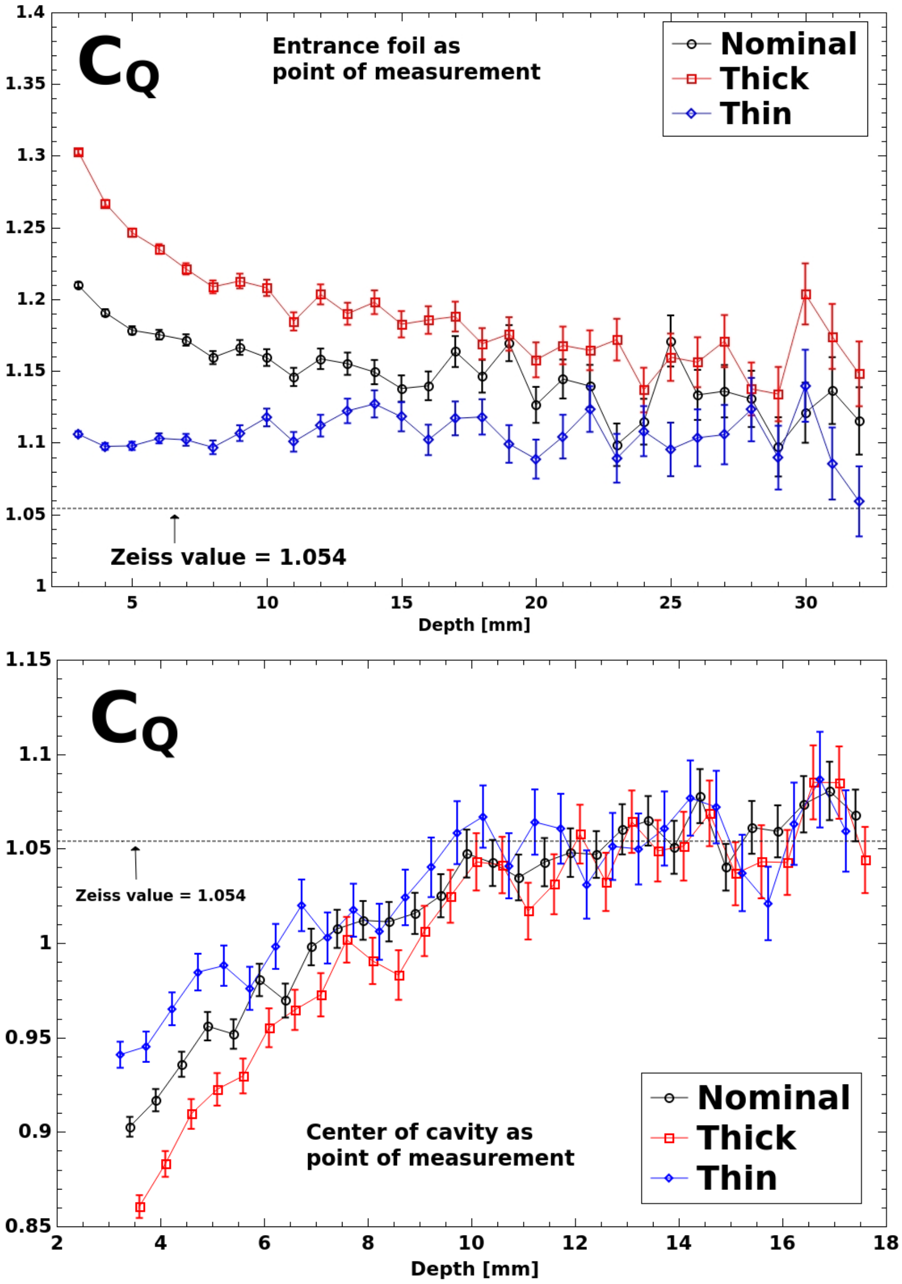

Figure 5.10 (Top) INTRABEAM ionization chamber conversion factor C_Q for PTW 34013 chamber calibrated in T30 kV reference beam as a function of depth in water, with the effective point of measurement defined as the inside of the chamber entrance foil, or (bottom) the air cavity centroid.

5.9 Appendix

5.1.1 N_{gas} and $(W/e)_{\text{air}}$ for kV photon beams

For an air-filled ionization chamber cavity, the gas calibration factor is given by:

$$N_{\text{gas}} = \frac{(W/e)_{\text{air}}}{m}, \tag{5.12}$$

where $(W/e)_{\text{air}}$ is the mean energy required for an electron to create an ion pair in dry air, and m is the cavity air mass. For initial electron energies larger than 10 keV, $(W/e)_{\text{air}}$ (and hence N_{gas}) is assumed to be constant, with a value of 33.97±0.05 J/C (CCEMRI 1985 [51]). However, it is known that below 10 keV a significant fraction of the initial electron energy becomes lost through non-ionizing processes, and $(W/e)_{\text{air}}$ diverges from the recommended value. To account for this energy dependence when calculating the number of ion pairs created in air starting from an initial photon, ICRU Report 90 (ICRU 2016 [52]) defines a correction factor, k_w:

$$k_w = \frac{N_{ip}^{33.97}}{N_{ip}^{W}}, \tag{5.13}$$

where $N_{ip}^{33.97}$ is the number of ion pairs created using $(W/e)_{\text{air}} = 33.97$ J/C, and N_{ip}^{W} is the number of ion pairs created using a fitted function of $(W/e)_{\text{air}}$ according to the model of Buhr *et al.* (2012) [53]. To calculate k_w, the MC particle transport code PENELOPE (Salvat 2015 [156]) was used to simulate the spectrum of first-generation electrons set in motion by photons, including Auger electrons. This correction can be as large as 5.5% at 1 keV ($k_w = 1.055$).

It is also important to note that the definition of N_{gas} in (5.12) does not account for the initial ion pair set in motion by an incident photon (since $(W/e)_{\text{air}}$ is defined for an initial electron). ICRU Report 90 provides an initial ion pair correction factor, k_{ii}:

$$k_{ii} = \frac{N_{ip}^{W}}{N_e + N_{ip}^{W}}, \tag{5.14}$$

where N_{ip}^{W} is the number of ion pairs created as defined in (5.13), and N_e is the total number of electrons set in motion. Again, PENELOPE was used for this calculation, taking into account fluorescent yields and atomic relaxation. At low photon energies, this correction becomes quite large ($k_{ii} = 0.932$ at 1 keV).

With these two correction factors, we can define an effective $(W/e)_{\text{air}}$ for monoenergetic photon beams applied to measurement with an air-filled ionization chamber:

$$(W/e)_{\text{eff}} = k_{ii}k_w(W/e)_{\text{air}}, \tag{5.15}$$

where $(W/e)_{\text{air}}$ is the accepted value of 33.97 J/C. Using $(W/e)_{\text{eff}}$ in place of $(W/e)_{\text{air}}$ in Eq.(5.12), the definition of N_{gas} for a monoenergetic photon beam becomes:

$$N_{\text{gas}} = \frac{k_{ii}k_w(W/e)_{\text{air}}}{m}. \tag{5.16}$$

Fortunately, the combined product of k_w and k_{ii} yields some cancellation, reducing the overall energy dependence correction to N_{gas} (see figure 5.11).

5.1.2 Methods and materials

To validate our assumption that N_{gas} can be considered a constant between photon beam qualities Q and Q_0, the weighted average of $k_{ii}k_w$ was calculated for Q and Q_0 photon fluence spectra, and its variation assessed. Here, the relevant beam qualities are the reference beam used to calibrate the ionization chamber (i.e. T30), and the beam quality of the measurement beam (i.e. INTRABEAM at depth in water). Using our EGSnrc source model, INTRABEAM photon fluence spectra were scored at various depths in water. To investigate the sensitivity of $k_{ii}k_w$ to the photon spectra perturbation due to the presence of the ionization chamber, spectra were also scored across the midpoint of the air cavity of a PTW 34014 ionization chamber, for the same depth in water (for example, figure 5.11 shows the two spectra at 1 mm depth in water). Similarly, the photon fluence spectra from a T30 reference beam in air for calibration conditions (see section 5.4.1) were calculated with and without ionization chamber. The tabulated values of $k_{ii}k_w$ were taken from ICRU Report 90, and the weighted average value was calculated for each spectrum.

5.1.3 Results and discussion

The average $k_{ii}k_w$ weighted by photon fluence spectra for all beam qualities investigated is displayed in table 5.2. In all cases, $k_{ii}k_w$ was found to vary by less than 0.1%. Our assumption that N_{gas} is constant is valid to within 0.08% for an ionization chamber (PTW 34013) calibrated in a T30 beam and performing measurements from an INTRABEAM source in water. The fluence perturbation due to the presence of the ionization chamber had a negligible effect on $k_{ii}k_w$, with the

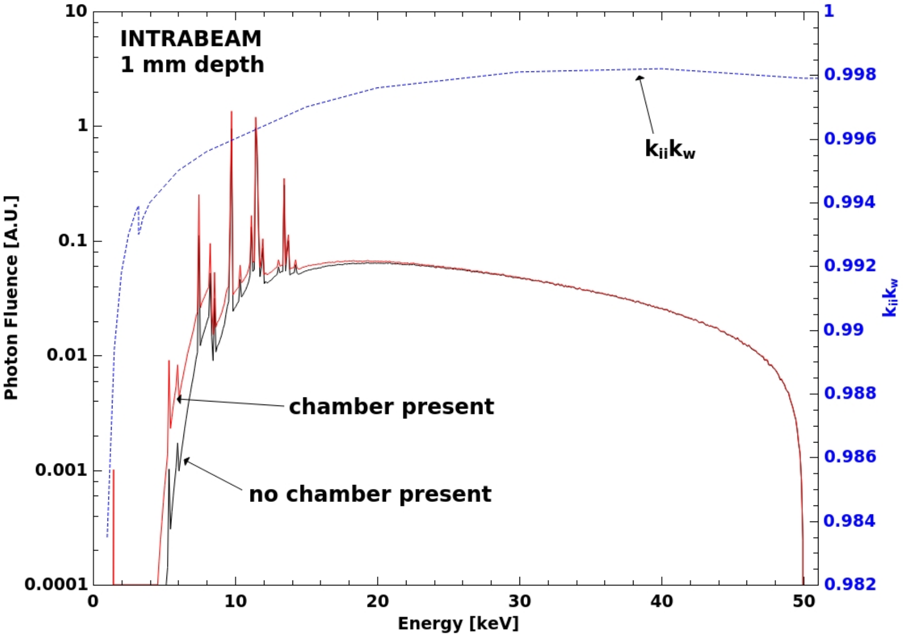

Figure 5.11 (Dashed line) The combined values of the initial ion correction factor, k_{ii}, and $(W/e)_{\text{air}}$ energy dependence correction factor, k_w, taken from ICRU Report 90. (Solid lines) Photon fluence spectra from the INTRABEAM source at 1 mm depth in water, both with and without the presence of an air-filled ionization chamber (PTW 34013). Here, we use the photon fluence spectra to calculate the weighted average of $k_{ii}k_w$ to assess its variation with the relevant photon beam qualities

largest effect (0.02%) occurring at 1 mm depth in water (difference in attenuation of fluorescence photons due to air cavity).

Even in the extreme case of performing measurements in an MV photon beam ($k_{ii}k_w \approx 1$), the assumption of constant N_{gas} still holds to within 0.3%. From figure 5.11, it can be seen that the deviation of $k_{ii}k_w$ from unity is relatively small (<0.5%) for photons above 6 keV, however below this energy the correction becomes as large as 2%. Thus, unless the reference (or measurement) beam spectra contains a significant amount of photons below 6 keV, we can assume that N_{gas} is a constant to within 0.5%.

Table 5.2 Average of $k_{ii}k_w$ weighted by photon fluence spectrum. Values are shown both with and without the presence of a PTW 34013 ionization chamber. Uncertainties on the values were calculated to be at the fifth decimal place.

	$k_{ii}k_w$	
Beam Quality	No Chamber	Chamber
T30	0.9974	0.9974
INTRABEAM 1 mm depth	0.9974	0.9972
INTRABEAM 5 mm depth	0.9977	0.9977
INTRABEAM 10 mm depth	0.9979	0.9978
INTRABEAM 20 mm depth	0.9980	0.9980

6

An investigation into the INTRABEAM miniature X-ray source dosimetry using ionization chamber and radiochromic film measurements

Peter G. F. Watson, Hamed Bekerat, Pavlos Papaconstadopoulos, Stephen Davis and Jan Seuntjens

Article published in: *Medical Physics* [49]

6.1 Preface

In this chapter, the C_Q dose formalism proposed in Chapter 5 is applied to determine the absorbed dose to water from an INTRABEAM source from ionization chamber measurements in a water phantom. These results are compared with the dose calculation following the manufacturer recommended formula stated in the water phantom manual, and the “corrected” formula to be consistent with the TARGIT protocol dose calibration. The dose determinations from ionization chamber measurements were then compared with the results of radiochromic film measurements.

6.2 Abstract

Purpose: Intraoperative radiotherapy using The INTRABEAM System (Carl Zeiss Meditec AG, Jena, Germany), a miniature low-energy X-ray source, has proven to be an effective modality in the treatment of breast cancer. However, some uncertainties remain in its dosimetry. In this work, we investigated the INTRABEAM system dosimetry by performing ionization chamber and radiochromic film measurements of absorbed dose in a water phantom.

Methods: Ionization chamber measurements were performed with a PTW 34013 parallel-plate soft X-ray chamber at source to detector distances of 5 mm to 30 mm in a water phantom. The absorbed dose to water was calculated using i) the dose formula consistent with the TARGIT breast protocol (TARGIT), ii) the formula recommended by the manufacturer (Zeiss), and iii) the recently proposed C_Q formalism of Watson *et al.* [48]. EBT3 Gafchromic film measurements were made at the same depths in water. To account for the energy dependence of EBT3 film, multiple dose response calibration curves were employed across a range of photon beam qualities relevant to the INTRABEAM spectrum in water.

Results: At all depths investigated, the TARGIT dose was significantly lower than that measured by the Zeiss and C_Q methods, as well as film. These dose differences ranged from 14% to as large as 80%. In general, the doses measured by film, and the Zeiss and C_Q methods were in good agreement to within measurement uncertainties (5-6%).

Conclusions: These results suggest that the TARGIT dose underestimates the physical dose to water from the INTRABEAM source. Understanding the correlation between the TARGIT and physical dose is important for any studies wishing to make dosimetric comparisons between the INTRABEAM and other radiation emitting devices.

6.3 Introduction

Miniature kilovoltage x-ray systems, such as the INTRABEAM system (Carl Zeiss Meditec AG, Jena, Germany) and the Xoft Axxent (iCAD Inc., Nashua, NH), have become a popular alternative to photon-emitting radioactive sources for use in intraoperative radiation therapy (IORT) [140]. As electronic devices, kV x-ray systems avoid the risks and regulations of radioactive materials, offering a number of benefits such as ease of transport to and from the operating room. These systems use low-energy photons (50 kVp) which deliver a very localised dose distribution with a steep dose gradient, offering the ability to spare healthy tissues. There may also be a biological benefit to using photons in this energy range due to their increased relative biological effectiveness [157–160].

In the TARGIT-A clinical trial, the outcomes of breast cancer patients receiving IORT performed with the INTRABEAM source (20 Gy delivered to the surgical margin) following lumpectomy were compared with those receiving whole breast irradiation. The five year rate of local cancer recurrence was found to be larger in the IORT group (3.3% vs 1.3%), however this difference was within the non-inferiority criteria of the study (non-inferiority margin of 2.5%) [161, 33] and may be a preferred treatment option for some patients. However, while treatments with INTRABEAM have shown to be safe and effective, some uncertainties remain in its dosimetry [31]. Accurate and precise knowledge of the absorbed dose delivered in radiation therapy is essential for achieving optimal treatment outcomes. As such, it is the goal of the radiation therapy process to deliver the prescribed dose as accurately as reasonably achievable [47]. Accurate dosimetry is also necessary for meaningful comparisons of patient outcomes with other radiation therapy treatments. In the case of breast IORT, accurate dosimetry is crucial for fair comparisons between INTRABEAM and other miniature kV systems (such as the Xoft Axxent) or external beam radiation therapy.

6.3.1 INTRABEAM Dosimetry

Manufacturer Calibration

At the time of writing, no absorbed dose to water primary standard has been established for the INTRABEAM, although an effort is underway at the National Metrology Institute of Germany (PTB). The system calibration is performed by the manufacturer using a soft x-ray ionization chamber (PTW 23342, Physikalisch Technische Werkstätte, Freiburg) in water. This chamber is calibrated in terms of exposure, and measurements are converted to absorbed dose to water using a factor of $f = 0.881$ cGy/R, based on data from ICRU Report 17 for 20 keV monoenergetic photons [101]. The absorbed dose rate to water is measured for a range of depths in water, generating a calibration depth dose curve which is used for calculating treatment delivery time. This method of calibration was established prior to the start of the TARGIT-A trial (pre-2000), and has been maintained to ensure consistency in the delivered prescription doses despite the development of improved kilovoltage dosimetry protocols [102] (i.e. AAPM TG-61 [54] or IAEA TRS 398 [55]).

Zeiss Water Phantom Dosimetry

To verify the manufacturer-provided calibration depth dose curve, Zeiss supplies a special water phantom consisting of a 3-dimensional translational stage for precise source positioning, and a PTW 34013 soft x-ray ionization chamber (0.005 cm^3). To calculate the dose to water using this phantom, the following equation is recommended in the water phantom user manual [102]:

$$D_W^{Zeiss}(z) = M(z) N_k k_Q k_{K_a \to D_W}, \tag{6.1}$$

where $M(z)$ is the measured charge (corrected for temperature and pressure variation), N_k is the ionization chamber air-kerma calibration coefficient, k_Q is the conversion factor from reference to INTRABEAM beam quality, and $k_{K_a \to D_W}$ is the chamber conversion factor from air-kerma to dose to water in a reference beam. Unfortunately, the authors were unable to find any information on how this conversion factor was determined. It is assumed that the INTRABEAM spectrum is equivalent to a T30 reference beam ($k_Q = 1$), and that k_Q is independent of distance from the source in water. In this work, we refer to the dose calculated by Eq.(6.1) as the “Zeiss” dose.

To compare with the calibration depth dose data, the water phantom manual states that the Zeiss dose must first be multiplied by a depth-dependent conversion factor, $f'(z)$, to calculate the so-called TARGIT dose,

$$D_W^{TARGIT}(z) = f'(z) \cdot D_W^{Zeiss}(z). \tag{6.2}$$

The specific values of $f'(z)$ are given in the user’s source acceptance report, and can vary from 0.5 to 0.9. It is stated in the water phantom manual that the dose conversion factor is intended to account for the differences in measurement conditions between the manufacturer source calibration and the Zeiss water phantom. These differences are explained to be: the change in effective point of measurement between the ionization chamber models used (PTW 23342 and 34013); different designs of waterproof holders for the two ionization chamber models; and different chamber calibration schemes (PTW 23342 in terms of exposure with $f = 0.881$ cGy/R, and PTW 34013 in air kerma with $k_{K_a \to D_W}$, presumably calculated with updated mass-energy absorption coefficients and $(W/e)_{\text{air}}$) [103].

The necessity for a conversion factor ($f'(z)$) to relate the TARGIT dose with the water phantom Zeiss dose is problematic, as by definition the absorbed dose to water should be independent of the experimental measurement setup. It is not clear if the physical dose is described by the TARGIT dose, the Zeiss dose, or neither.

Both the TARGIT and Zeiss dose protocols do not account for the variation in $(\bar{\mu}_{en}/\rho)^{w}_{air}$ (and hence f) due to the photon fluence spectrum hardening as a function of depth in water. Ebert and Carruthers [152] reported this variation to be 2.6% over a distance of 2 cm from the source in water, and as large as 5% at a depth of 10 cm. Watson *et al.* [48] found a similar relative difference in $(\bar{\mu}_{en}/\rho)^{w}_{air}$ of 2.5% over 2 cm in water, however their absolute values do not agree with Ebert and Carruthers (1.045 to 1.018 versus 0.9 to 0.876, respectively). The measured and simulated half value layers (HVL) for the INTRABEAM across this depth ranges from 0.1 to 2 mm Al [136, 48], which corresponds to mass energy absorption coefficient ratios of 1.044 to 1.018, as taken from TG-61, corroborating the results of Watson *et al.*

Independent Dose Measurements: Ionization Chamber

A number of studies have been published which investigate the dosimetry of the INTRABEAM system. The source calibration using the IPEMB code of practice for low-energy x-rays [89] was investigated by Eaton and Duck [41]. In their paper they determined chamber correction factors (k_{ch}), however they did not make any absolute dose comparisons between the IPEMB and the TARGIT or Zeiss dose. Siochi [162] performed an in-air TG-61 [54] based calibration with spherical applicators. Excellent agreement (percent difference of $<1\%$) was found with the Zeiss dose, however an uncertainty analysis of the TG-61 calibration was not performed.

Watson *et al.* investigated the Zeiss dose protocol in Eq.(6.1) by determining a Monte Carlo (MC) calculated chamber conversion factor (C_Q) for a PTW 34013 chamber, equivalent to the product of $k_Q k_{K_a \to D_W}$. They found that the Zeiss dose consistently underestimated the absorbed dose to water, with differences of up to 23%. This result implies that the TARGIT dose even further underestimates the physical dose, since the conversion factor $f'(z)$ is less than unity for all depths. Watson *et al.* determined that the chamber conversion factor was sensitive to the plate separation tolerance of the PTW 34013 chamber, leading to a potential variation in measured dose as large as 15%.

Independent Dose Measurements: Radiochromic Film

Radiochromic films, such as Gafchromic models, have been used in previous studies to investigate the relative and absolute dosimetry of the INTRABEAM system [41, 163, 164]. Accurate dosimetry with these films is challenging, as they are known to have an energy dependent response at low photon energies [64, 165, 166]. Eaton and Duck reported differences of up to 6.9% between percent depth dose curves measured with an ionization chamber and Gafchromic EBT film [41], and up to 8.8% local difference ($<$ 10 mm from applicator surface) and 4.8% absolute ($>$ 10 mm from applicator surface) difference from the manufacturer (i.e. TARGIT) depth dose curve. They attributed these differences to other experimental uncertainties, such as positioning, rather than film energy dependence.

Ebert *et al.* [163] investigated the response of three types of radiochromic film (EBT, XR-QA and XR-RV2) for doses delivered with the source in water, at depths of 5 mm, 15 mm and 30 mm. They reported significant dose response differences with depth in water for all film types which they attributed to film energy dependence due to beam hardening, and suggested that these films are unsuitable for INTRABEAM quantitative dosimetry.

6.3.2 Purpose

This work investigates the accuracy of the TARGIT (Eq.(6.2)) and Zeiss (Eq.(6.1)) dose determinations in describing the physical absorbed dose to water by comparing them with different determination methods. Two independent methods were also used to measure the absorbed dose to water from an INTRABEAM system in a water phantom. 1) Using a PTW 34013 ionization chamber, we calculated the absorbed dose using the recent C_Q formalism of Watson *et al.* [48] 2) EBT3 Gafchromic films were used to determine absorbed dose. To account for the film energy dependence, multiple dose response calibration curves were investigated across a range of photon beam qualities relevant to the source spectrum in water.

6.4 Materials and Methods

Measurements were performed by irradiating a PTW 34013 ionization chamber or EBT3 Gafchromic film at a predetermined distance from an INTRABEAM source (5 mm to 30 mm in increments of 5 mm) for a constant amount of time (30 s at 5 mm depth, 180 s for all other depths). These time durations were selected to deliver a measurable amount of dose to the point of measurement without signal saturation (between 0.5 to 12 Gy), while providing a long enough irradiation to minimize the effect of timer error. All measurements were performed on the same day with the same source (S/N 507299). The irradiation time was manually controlled.

6.4.1 Ionization Chamber Measurements

Experimental Setup

Ionization chamber measurements were performed in the self-shielded water phantom provided by Zeiss. This phantom features a 3-dimensional translational stage for mounting and positioning the source, with a reported accuracy of 0.1 mm [102]. Inside the phantom are two fixed waterproof chamber covers (one for isotropy, one for depth dose measurements) designed to hold a PTW 34013 parallel-plate ionization chamber.

A PTW 34013 ionization chamber was placed into the waterproof holder intended for depth dose measurements, and allowed to equilibrate to the water temperature. The chamber was connected to a UNIDOS E electrometer, and operated at a voltage of 400 V. The minimum distance from the probe tip to the reference point of the ionization chamber, z_0, was determined by the following equation:

$$z_0 = x_H + x_{air} + x_{IC}, \tag{6.3}$$

where x_H is the thickness of the waterproof chamber holder wall (printed on the chamber holder, in our case $x_H = 1.018$ mm), x_{air} is the air gap between the upper surface of the chamber housing and the inside of the chamber holder wall (reported as $x_{air} = 0.5$ mm), and x_{IC} is the distance from the chamber reference point to the upper surface of the chamber housing (reported as $x_{IC} = 0.155$ mm on the chamber calibration certificate). Thus, from our value of $z_0 = 1.673$ mm, the Z position of the water phantom translational stage could be calculated to obtain the measurement depths of 5 to 30 mm (in increments of 5 mm). The chamber was irradiated and the measured charge was recorded, corrected for temperature and pressure variations. Measurements were repeated three times for each depth, and the average and standard deviation of the mean were calculated.

Ion Collection Efficiency and Polarity Correction

In the definition of Eq.(6.1), no mention is made of an ion recombination correction (P_{ion}) or polarity correction (P_{pol}) [102]. To verify whether these two corrections can be neglected for the PTW 34013 chamber and INTRABEAM source, P_{ion} and P_{pol} were determined. Here, we use the TG-61 definitions of

$$P_{\text{ion}} = \frac{1-(V_H/V_L)^2}{M_H/M_L-(V_H/V_L)^2}, \tag{6.4}$$

where M_H is the signal from the chamber at normal operation voltage V_H, and M_L is the signal at voltage V_L ($V_L/V_H \leq 0.5$), and

$$P_{\text{pol}} = \left| \frac{M^+ - M^-}{2M} \right|, \tag{6.5}$$

where M^+ and M^- are the readings at positive and negative bias, and the denominator M is the reading at the bias used for reference measurements.

Timer Error

When performing dose measurements with the INTRABEAM, there is a “ramp up” of the output immediately after starting an irradiation, and a corresponding “ramp down” after stopping. This effect is analogous to the timer error of cobalt teletherapy machines, and has been previously reported [135]. To quantify this effect, we calculated the timer error following the approach of Orton and Seibert [167] by performing n multiple exposures of duration t/n (cumulative chamber reading $R_{n(t/n)}$), and a single exposure of duration t (reading R_t). The timer error is then:

$$e = \left[\frac{R_{n(t/n)} - R_t}{nR_t - R_{n(t/n)}} \right] t. \tag{6.6}$$

The standard deviation of the error is given by:

$$\sigma_e = e\sqrt{2\sigma_R^2}/(R_{n(t/n)} - R_t), \tag{6.7}$$

where σ_R is the standard deviation of the multiple exposure readings.

Absorbed Dose Calculations

Three methods were used to calculate the absorbed dose to water from the measured ionization chamber charge signal: the formula recommended by water phantom manual (the “Zeiss” dose) of Eq.(6.1); the “TARGIT” dose as defined by Eq.(6.2); and the “C_Q” dose formalism of Watson *et al.* [48] The absorbed dose to water calculated with the C_Q formalism is given by:

$$D_W^{C_Q}(z) = M(z)C_Q(z)N_k, \tag{6.8}$$

where $M(z)$ and N_k are the same corrected measured charge and ionization chamber calibration coefficient as in Eq.(6.1), and $C_Q(z)$ is the ionization chamber conversion factor from air-kerma in a reference beam to dose to water for the source beam quality.

The depth-dependent values of C_Q for the PTW 34013 chamber were calculated using the EGSnrc MC code [107], and the results have statistical fluctuations which increase as a function of depth in water. This is because the number of transported particles (number of starting particles = 1.5×10^8) decreases with depth due to attenuation and scattering. While these fluctuations can be reduced by simply simulating more particles, this is time and resource consuming. Alternatively, these fluctuations can be smoothed by fitting a curve to C_Q, assuming a functional relationship with depth in water. From the definition of C_Q, we see it is proportional to the ratio of D_w/D_{gas}. To first order, this ratio is equal to the ratio of the average mass energy absorption coefficients of water to air, $(\bar{\mu}_{en}/\rho)^{w}_{\text{air}}$, assuming a large air cavity. The behaviour of $(\bar{\mu}_{en}/\rho)^{w}_{\text{air}}$ as a function of photon energy in the kinematic region relevant to the INTRABEAM spectra is smoothly varying without inflection points [168] (the reader is directed to Ref. [48], figure 1). Based on this, a function of the form $f(x) = ae^{-bx} + ce^{-dx}$ was fit to the C_Q data. This was performed with MATLAB R2015b (The MathWorks, Inc., Natick, MA) using the `fit` function (linear least squares method), with a weighing of $1/\sigma_i^2$ for each $C_{Q,i}$ (where σ_i is the statistical uncertainty). The 68.3% (1σ) simultaneous confidence interval (confidence for all predictor values) on the fitted function was calculated. Fig. 6.1 shows the MC-calculated C_Q values (taken from Ref. [48]), along with the fitted curves (solid lines) and confidence intervals (dashed lines), for three variations of the PTW 34013 ionization chamber featuring differing parallel-plate separations (the nominal separation, and the reported tolerance maximum ("thick") and minimum ("thin") separation). The exact dimensions of the cavity are not included in this report as they are proprietary information. For the calculation of dose in Eq.(6.8), the nominal C_Q curve was used, and the thick and thin C_Q curves were used to estimate the chamber model geometry uncertainty, discussed in section 6.4.1.

Dose Uncertainty Calculations

The estimation and propagation of uncertainty in the dose measurements was performed as outlined in the BIPM Guide to the Expression of Uncertainty in Measurement [169]. The uncertainty on the dose calculated using the Zeiss method (Eq.(6.1)) was determined by:

$$\sigma_{\text{Zeiss}} = \sqrt{\sigma_{rep}^2 + \sigma_{\text{pos}}^2 + \sigma_{k_Q k_{K_a \to D_W}}^2} \tag{6.9}$$

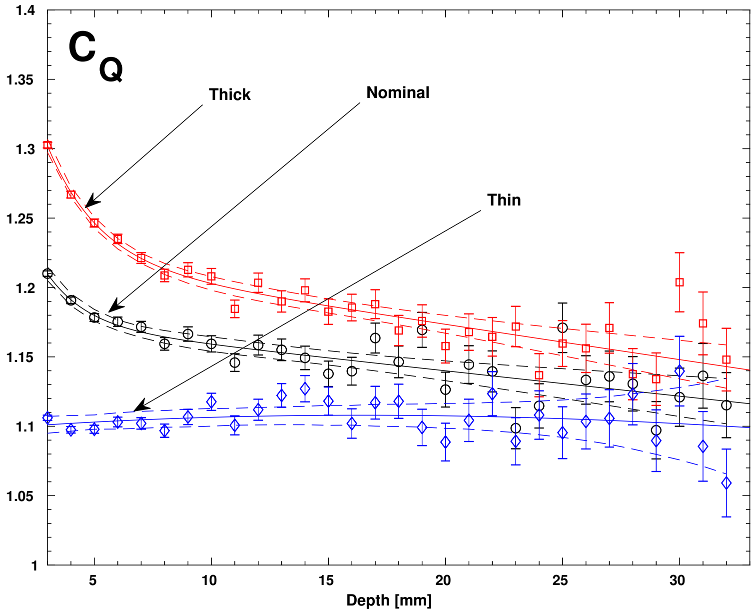

Figure 6.1 Fitted functions (solid lines) and confidence intervals (dashed lines) to the INTRABEAM ionization chamber conversion factor C_Q for a PTW 34013 chamber as a function of depth in water. Thick, thin and nominal refer to the modeled chamber plate separation.

where σ_{rep} is the standard deviation of the mean from the three ionization chamber charge readings, σ_{pos} is the dose uncertainty due to chamber positioning error and $\sigma_{k_Q k_{K_a \to D_W}}$ is the relative uncertainty on the product of N_k, k_Q and $k_{K_a \to D_W}$. At all depths investigated, σ_{rep} was less than 0.3%. The positioning dose uncertainty was determined by measuring the dose rate at ±0.1 mm at each measurement depth. This uncertainty ranged from 5.2% at 5 mm to 1.0% at 30 mm depth. The ionization chamber calibration certificate reports that $\sigma_{k_Q k_{K_a \to D_W}}$ is 4% with a coverage factor of two (k=2). According to the calibration certificate, this uncertainty was calculated according to ISO GUM from the partial uncertainties arising from the standard used, the calibration procedure, the environmental conditions and the short time effects of the object of measurement. Thus for k=1, $\sigma_{k_Q k_{K_a \to D_W}}$ was taken to be 2%. The combined uncertainty (k=1) is listed in table 6.1.

The TARGIT dose uncertainty in Eq.(6.2) was estimated by:

$$\sigma_{TARGIT} = \sqrt{\sigma^2_{\text{Zeiss}} + \sigma^2_{f'}}, \tag{6.10}$$

Table 6.1 Uncertainty budget in calculating absorbed dose to water with an ionization chamber using the Zeiss method. All values are in percent.

Source of Uncertainty	Depth in water					
	5 mm	10 mm	15 mm	20 mm	25 mm	30 mm
σ_{rep}	0.27	0.11	0.08	0.04	0.05	0.16
σ_{pos}	5.2	2.6	1.8	1.4	1.1	1.0
$\sigma_{k_Q k_{K_a \to D_W}}$	2.0	2.0	2.0	2.0	2.0	2.0
$\sigma_{\text{Zeiss}}(k=1)$	5.6	3.3	2.7	2.4	2.3	2.2

Table 6.2 Uncertainty budget in calculating absorbed dose to water with an ionization chamber using the TARGIT method. All values are in percent.

Source of Uncertainty	Depth in water					
	5 mm	10 mm	15 mm	20 mm	25 mm	30 mm
$\sigma_{\text{Zeiss}}(k=1)$	5.6	3.3	2.7	2.4	2.3	2.2
$\sigma_{f'}$	5.1	5.1	5.1	5.1	5.1	5.1
$\sigma_{TARGIT}(k=1)$	7.6	6.1	5.8	5.7	5.6	5.6

where σ_{Zeiss} is as defined in Eq.(6.9), and $\sigma_{f'}$ is the uncertainty on the correction function $f'(z)$, reported to be 5.1% in our source acceptance test report. The combined uncertainty (k=1) is listed in table 6.2.

The C_Q dose uncertainty is given by:

$$\sigma_{C_Q} = \sqrt{\sigma_{\text{rep}}^2 + \sigma_{\text{pos}}^2 + \sigma_{\text{fit}}^2 + \sigma_{\text{geom}}^2}, \tag{6.11}$$

where σ_{rep} and σ_{pos} are the same as in Eq.(6.9), σ_{fit} is the 68.3% confidence interval (1 σ) on the functional fit of C_Q, and σ_{geom} is the chamber cavity geometry uncertainty (due to plate separation tolerance) of C_Q. Assuming a rectangular distribution of chamber plate separations during manufacturing, σ_{geom} was estimated from the fits of C_Q for the thick and thin chamber models as: $\sigma_{\text{geom}} = 100 \cdot (C_Q^{thick} - C_Q^{thin})/(\sqrt{12} \cdot C_Q^{nominal})$. Table 6.3 lists the C_Q uncertainty budget for each measurement depth.

Table 6.3 Uncertainty budget in calculating absorbed dose to water with an ionization chamber using the C_Q method. All values are in percent.

Source of Uncertainty	Depth in water					
	5 mm	10 mm	15 mm	20 mm	25 mm	30 mm
σ_{rep}	0.27	0.11	0.08	0.04	0.05	0.16
σ_{pos}	5.2	2.6	1.8	1.4	1.1	1.0
σ_{fit}	0.36	0.45	0.45	0.63	0.95	1.3
σ_{geom}	3.5	2.4	2.0	1.7	1.4	1.2
$\sigma_{C_Q}(k=1)$	6.3	3.6	2.7	2.2	2.0	2.0

Table 6.4 Orthovoltage beam qualities used to calibrate EBT3 films.

Nominal energy	Add. filtration	HVL [mm Al]	E_{eff} [keV]
50 kVp	–	0.120	10.72
50 kVp	0.5 mm Al + 5.75 mm PMMA	0.816*	20.64
70 kVp	–	1.26	24.07
80 kVp	–	2.18	29.51

*At 23 cm SDD

6.4.2 Film Measurements

EBT3 Film Calibration

In this work, the recommendations of Devic *et al.*[60] were followed for the radiochromic film dosimetry. A Gulmay orthovoltage x-ray unit was used to irradiate the films to generate net optical density (ΔnetOD) to absorbed dose to water (to a small volume in air) calibration curves. Tube potentials of 50, 70, and 80 kVp (with a 5 cm circular applicator) were used to calibrate films, as listed in table 6.4. An additional beam quality at 50 kVp was created by placing filtration (0.5 mm Al and 5.75 mm PMMA) at the exit of the applicator.

Prior to film irradiation, half-value layer (HVL) measurements were performed for each beam quality listed in table 6.4, following the guidelines of the AAPM TG-61 dosimetry protocol [54]. The HVL was measured at 40 cm source-to-detector distance (SDD). An SDD of 40 cm was also used for the position of reference dosimetry and film irradiations, with exception to the filtered 50 kVp measurements which were performed at 23 cm. In that case, a reduced SDD was necessary to obtain a reasonable dose rate due to the signal attenuation from the additional filtration.

Due to the different photon spectrum attenuation through air, one cannot assume that the HVL measured at 40 cm SDD will be representative of the HVL at 23 cm. The SpekCalc [170] calculated spectrum of the 50 kVp beam was obtained from Bekerat *et al.* [64] to estimate the effect of SDD on the HVL. This spectrum was used as input in an EGSnrc simulation to calculate the photon fluence spectra at 23 cm and 40 cm SDD in air. The user code `cavity` was used to model a circularly collimated photon source (5 cm diameter at 20 cm to match applicator), with 0.5 mm Al and 5.75 mm PMMA filtration, enveloped in a 1 m^3 box of air. The photon fluence spectra was scored across a 1 cm diameter circular plane positioned at 23 cm and 40 cm from the source. From the spectra, the HVL was determined analytically by solving the following equation:

$$0.5 = \frac{\sum_i E_i \Phi_i \left(\frac{\mu_{en}}{\rho}\right)_{i,\mathrm{air}} e^{-\mu_{i,\mathrm{Al}} x_{\mathrm{Al}}}}{\sum_i E_i \Phi_i \left(\frac{\mu_{en}}{\rho}\right)_{i,\mathrm{air}}}, \tag{6.12}$$

where x_{Al} is the HVL in thickness of aluminium, $\mu_{i,\mathrm{Al}}$ is the attenuation coefficient of aluminum for energy bin i, E_i is the photon bin energy, and $\left(\frac{\mu_{en}}{\rho}\right)_{i,\mathrm{air}}$ is the mass energy absorption coefficient for air. Attenuation coefficients were taken from the NIST XCOM database [171]. The simulated HVL at 40 cm was calculated to be 0.846 mm Al, and 0.828 mm Al at 23 cm, for a ΔHVL of -0.018 mm Al, or approximately 2%. A second 50 kVp source spectrum with slightly different inherent filtration obtained from Bekerat *et al.* was also investigated by the preceding method, with similar results (ΔHVL = -0.022 mm Al). Based on this outcome, we estimated that the filtered 50 kVp HVL at 23 cm would be 0.02 mm Al less than that measured at 40 cm.

Next, reference dosimetry was performed free in air with an ionization chamber positioned along the central axis of the beam. Two types of ionization chambers were used: a PTW 23342 parallel-plate chamber was used for tube potentials of 50 and 70 kVp, and a Farmer type NE 2577C thimble chamber for the tube potential of 80 kVp. The thimble chamber was not used to calibrate the lower energy beams as its energy response was shown to vary greatly (up to 23%) at these beam qualities [64]. The air-kerma calibration coefficient of these chambers (N_k) was measured by the National Research Council of Canada (NRCC) in beam qualities of 50 kVp (two filtrations, HVL=0.17 mm Al and 0.32 mm Al) for the PTW 23342, and 80 kVp (HVL=1.82 mm Al) and 120 kVp (HVL=3.03 mm Al) for the NE 2577C. These qualities are similar to those used for the film calibration (listed in table 6.4). The calibration values of N_k were interpolated as a function of HVL to the appropriate beam qualities, and assumed to have a 1 σ variation of 2% (uncertainty estimate taken from TG-61 [54]).

The absorbed dose to water was calculated for a given number of monitor units (MU) as recommended by TG-61:

$$D_\mathrm{w} = MN_k P_\mathrm{stem,air} \left[\left(\frac{\bar{\mu}_\mathrm{en}}{\rho} \right)^w_\mathrm{air} \right]_\mathrm{air}, \tag{6.13}$$

where M is the chamber reading (corrected for temperature, pressure, ion recombination and polarity effect), $P_\mathrm{stem,air}$ is the chamber stem correction factor (assumed to be unity [172]), and $[(\bar{\mu}_\mathrm{en}/\rho)^w_\mathrm{air}]_\mathrm{air}$ is the mass energy absorption coefficient ratio of water to air averaged over photon spectrum in air (taken from Table IV in TG-61). From Eq.(6.13), the output for each beam quality was measured in dose (Gy) per MU.

The uncertainty in the delivered absorbed dose was estimated as:

$$\sigma_\mathrm{cal} = \sqrt{\sigma^2_{N_k} + \sigma^2_\mathrm{diff} + \sigma^2_{\mu_{en}} + \sigma^2_\mathrm{pos}}, \tag{6.14}$$

where σ_{N_k} is the uncertainty in N_k reported by the calibration standards laboratory (0.7%), σ_diff accounts for N_k variation due to the difference in beam quality between calibration and measurement conditions (2%), $\sigma_{\mu_{en}}$ is the uncertainty in tabulated TG-61 $[(\bar{\mu}_\mathrm{en}/\rho)^w_\mathrm{air}]_\mathrm{air}$ values (1.5%), and σ_pos is the uncertainty due to chamber positioning error ($\pm$ 1 mm $\rightarrow$ 0.5% or 0.87% for 40 or 23 cm SDD, respectively). This lead to a combined uncertainty (k=1) of $\sigma_\mathrm{cal} = 2.7\%$ for the filtered 50 kVp, and $\sigma_\mathrm{cal} = 2.6\%$ for all other beam qualities.

After reference dosimetry had been completed, 6.7×4.0 cm^2 pieces of Gafchromic EBT3 film (lot number 04201601) were irradiated to dose levels of 0 to 17 or 20 Gy for each beam quality. The films were irradiated in air, suspended by two pieces of nylon monofilament at the same SDD as reference dosimetry measurements (40 or 23 cm). Post irradiation, the films were left to self-develop for 24 hours in a black envelope.

The films were scanned both prior to and post irradiation on an Epson 10000XL flatbed document scanner (Epson Seiko Corporation, Nagano, Japan) in transmission mode with a resolution of 127 dpi (0.2 mm/pixel). Care was taken to maintain the orientation of the films on the scanner bed for the pre-and post-irradiation scans. The scanned image data was saved in 48-bit RGB TIFF format, and a blank scan was performed to identify defective pixels. A background "dark" scan was omitted from the film analysis as it was found to have negligible effect on the results while increasing noise.

The image analysis was performed using MATLAB R2015b (The MathWorks, Inc., Natick, MA) similar to the work of Papaconstadopoulos *et al.* [173]. Analysis was performed using red channel data as it has shown to have higher sensitivity and low uncertainty in the dose range investigated, in particular below 4 Gy [173, 174]. The pre- and post- irradiated film images were rotated and coregistered to ensure coincidence of the region-of-interest (ROI). A Wiener filter (5×5 pixels) was applied to the image to remove noise due to the scanner. A list of defective pixels was generated from the blank scan, where any pixel with a value less than 95% of the maximum was classified as defective and ignored in further processing. For every film, five ROIs (0.5×0.5 cm^2) were randomly selected and used to calculate a mean pixel value and standard deviation. From these five measurements, the weighted mean, M (weighted by the inverse of ROI standard deviation) was calculated.

The netOD for each film was then calculated as:

$$\text{netOD} = \log_{10}\left(\frac{M_{irr}}{M_{unirr}}\right), \tag{6.15}$$

where M_{unirr} and M_{irr} are the weighted mean of the pre-and post-irradiated film, respectively. To account for film darkening due to environmental and temporal effects, the netOD of the 0 Gy film was subtracted:

$$\Delta\text{netOD} = \text{netOD} - \text{netOD}_{0\text{Gy}}. \tag{6.16}$$

The netOD uncertainty, $\delta\Delta$netOD, was calculated by error propagation across Eq.(6.16) as described by [175].

The relationship between film response (ΔnetOD) and dose (D) was determined by fitting a polynomial function:

$$D = p \cdot \Delta\text{netOD} + q \cdot \Delta\text{netOD}^n, \tag{6.17}$$

where p, q and n are free parameters. The MATLAB function `fit` (linear least squares) was used, with $1/\delta\Delta\text{netOD}^2$ as weights. The uncertainty in dose was estimated by error propagation across Eq.(6.17),

$$\delta D = \sqrt{\left(\frac{dD}{dp}\right)^2 \delta p^2 + \left(\frac{dD}{dq}\right)^2 \delta q^2 + \left(\frac{dD}{d\Delta\text{netOD}}\right)^2 \delta\Delta\text{netOD}^2}, \tag{6.18}$$

where δp and δq are the one sigma confidence intervals of p and q. In this work, n was determined manually such that dose error (the difference between dose calculated with Eq.(6.17) and the actual delivered dose) was minimized, while also giving a valid dose uncertainty estimate ($\sim$67% of dose error data points are encapsulated by the estimated uncertainty).

INTRABEAM Film Irradiations

Film from the same batch used during calibration were cut into 5×4 cm^2 pieces and scanned prior to irradiation. To fix the position of the films in the water phantom, a custom PMMA film holder was constructed containing two arms with a series of machined grooves spaced 5 mm apart. Along each groove, two strands of nylon monofilament were strung between which the pieces of film could be held in place. Films were installed in the holder and then submerged into the water phantom. The film installed in the top-most groove of the film holder was not used for dosimetry, but to aid in positioning the source probe (defining a depth of 0 mm). The films were arranged into two experimental configurations: A) one film was placed at 5 mm depth and irradiated for 30 s, and B) films were placed every 5 mm from 10 mm to 30 mm and irradiated for 180 s. A control film which was submerged in water for the same duration of time as the other films but not irradiated was kept for analysis, however water immersion for this short length of time was not expected to have any effect on the films [176]. Post-irradiation, the films were placed on a paper towel and exposed to the open air for 2 hours to dry any residual water droplets, then allowed to self-develop for 24 hours in a black envelope before scanning. To assess the reproducibility of the measurements, the film irradiations were repeated for three sets of films.

Film Dose Evaluation

The image analysis was again performed with MATLAB R2015b. For each film, the netOD was calculated in a 2.57×2.57 mm^2 square ROI (equivalent square of the PTW 34013 entrance window size, $r = 1.45$ mm) in the center of the radiation field (i.e. position of ionization chamber). Using Eq.(6.16), the ΔnetOD was calculated by subtracting the control film netOD to account for the effect of environmental factors, including submersion in water. The film dose could then be determined using Eq.(6.17). The dose uncertainty was calculated as:

$$\sigma_{\text{film,cal}} = \sqrt{\sigma_D^2 + \sigma_{\text{cal}}^2}, \tag{6.19}$$

where $\sigma_D = 100 * \delta D / D$ (the fitted dose and dose uncertainty in Eq.(6.17) and (6.18)), and σ_{cal} is the absorbed dose calibration uncertainty of Eq.(6.14).

The following methodology was used to account for the film energy response on the dose measurement. Using a previously published EGSnrc model of the INTRABEAM source [6, 48], the source photon fluence spectra was simulated at various depths in water. From the spectra, the

Table 6.5 HVL of INTRABEAM source at various depths in water. Results were calculated from simulated spectra.

Depth in water	HVL [mm Al]
5 mm	0.476
10 mm	0.850
15 mm	1.14
20 mm	1.34
25 mm	1.52
30 mm	1.65

HVL as a function of depth in water was calculated using Eq.(6.12). The resulting HVLs are listed in table 6.5.

For a measurement at a given depth in water, the film dose and uncertainty were calculated using Eqs.(6.17) and (6.19) from two sets of calibration data (see table 6.4): the HVLs immediately above and below the measurement HVL listed in table 6.5. The dose (and dose uncertainty) at the source beam quality was estimated by linearly interpolating between these two results as a function of HVL. This procedure was repeated for the three measurements at each depth, and the mean dose and standard deviation were calculated. By using this method, the film energy dependence is taken into account through the measured calibration curves, rather than relying on assumptions about the radiochromic film intrinsic energy dependence.

Film Holder Correction Factor

To account for the dose perturbation at the point of measurement due to the presence of other pieces of film, the film holder body, and the ionization chamber holders (permanently fixed in the water phantom), a film holder correction factor was defined:

$$k_{\text{Film Holder}}(z) = \frac{D_{\text{w}}(z)}{D_{\text{holder}}(z)}, \tag{6.20}$$

where $D_{\text{holder}}(z)$ and $D_{\text{w}}(z)$ are the dose to water at depth z with and without the presence of the films, film holder and chamber holders, respectively. The corrected dose to water would then be $D_{corr} = k_{\text{Film Holder}}D$, where D is the measured film dose from Eq.(6.17).

The film holder correction factor was calculated using the same EGSnrc model of the INTRABEAM source as in Section 6.4.2. The dose to a cylindrical water volume ($r = 5$ mm, $h = 1$ mm) centered at each measurement depth was scored. Figure 6.2 shows the geometry used in the simulation to calculate $D_{\text{holder}}(z)$, with the film at each measurement depth replaced with water. When calculating $D_{\text{w}}(z)$ all media other than the source probe were set to water. To simplify the simulation geometry, the films were modeled as homogeneous slabs, while in reality they are made up of an active layer sandwiched between two polyester layers. Table 6.6 lists the overall elemental composition of EBT3 film used in the simulation [177].

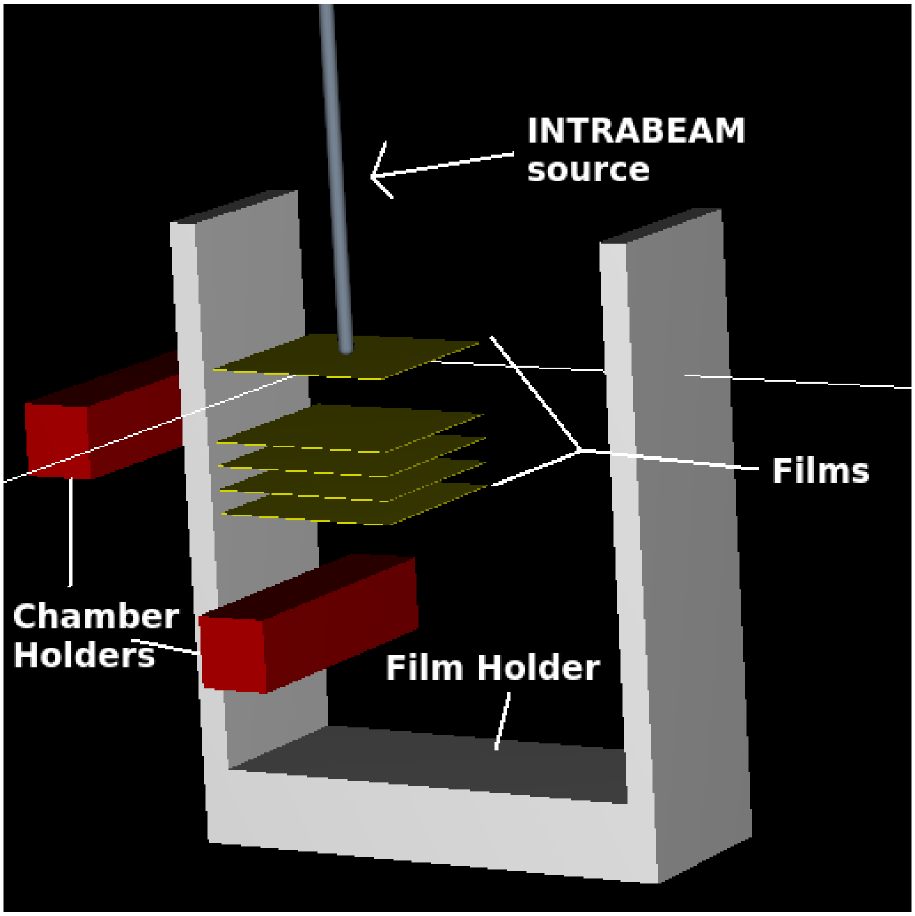

Figure 6.2 Rendering of experimental setup during film irradiations in water with the INTRABEAM. This geometry was used to calculate the film holder correction factor.

Film Dose Uncertainty

The overall uncertainty in the film dose measurement was estimated by:

$$\sigma_{\text{film}} = \sqrt{\sigma^2_{\text{film,avg}} + \sigma^2_{\text{rep}} + \sigma^2_{\text{pos}}} \tag{6.21}$$

Table 6.6 Overall elemental composition of EBT3 Gafchromic film in atomic percent. The effective atomic number and density are also listed.

H	Li	C	O	Al	Z_{eff}	Density (g/cm^3)
38.4	0.1	43.7	17.7	0.2	6.71	1.335

Table 6.7 Uncertainty budget in calculating absorbed dose to water with film. All values are in percent.

Source of Uncertainty	Depth in water					
	5 mm	10 mm	15 mm	20 mm	25 mm	30 mm
$\sigma_{\text{film,avg}}$	3.3	3.6	4.1	4.5	4.6	4.9
σ_{rep}	1.3	1.5	1.4	1.2	1.6	2.6
σ_{pos}	5.2	2.6	1.8	1.4	1.1	1.0
$\sigma_{\text{film}}(k=1)$	6.3	4.7	4.7	4.8	5.0	5.6

where $\sigma_{\text{film,avg}}$ is the average interpolated uncertainty ($\sigma_{\text{film,cal}}$ of Eq.(6.19)) of the three film measurements. σ_{rep} is the standard deviation of the mean of the three film dose measurements, and σ_{pos} is the uncertainty due to film positioning error.

The uncertainty due to film positioning error was calculated by first estimating the positioning error inherent to the PMMA film holder due to the play in the machined grooves (width of 0.73 mm) and two strands of nylon monofilament (diameter of 0.284 mm each). This gives a conservative positioning error of ±0.1 mm, coincidentally the same positioning accuracy of the ionization chamber measurements. Table 6.7 lists the uncertainty budget for estimating σ_{film} at each measurement depth, which was found to range from 6.3 to 4.7%. The average interpolated film dose uncertainty, $\sigma_{\text{film,cal}}$, was found to increase with depth (i.e. with lower absorbed dose), which lead to some compensation with the position uncertainty, σ_{pos}, which decreased with depth.

6.5 Results

6.5.1 Ion Collection Efficiency and Polarity Correction

P_{ion} was determined according to Eq.(6.4) to be 1.003 at a measurement depth of 5 mm, corresponding to a dose rate of ~20 Gy/min. A second set of measurements performed at 10 mm depth (dose rate of ~4 Gy/min) also yielded $P_{\text{ion}} = 1.003$, suggesting that this correction is independent of depth in water beyond 5 mm for the INTRABEAM. Using Eq.(6.5), P_{pol} was found to be 1.005. These correction factors were found to be just as significant as the temperature and pressure correction (P_{TP}=1.004), and were used in the calculation of all further ionization chamber measurements.

6.5.2 Timer Error

A set of measurements were performed at 10 mm depth in water, consisting of three measurements of 60 seconds duration and one of 180 seconds. The timer error was found to be 0.014 ± 0.12 seconds. The uncertainty in estimating the timer error was much larger than the error itself owing to $(R_{n(t/n)} - R_t)$ being much smaller than σ_R.

6.5.3 EBT3 Film Calibration

The fitted film calibration curves for the beam qualities listed in table 6.4 are shown in figure 6.3. The curves for the 50 kVp + filtration, 70 kVp and 80 kVp beams (E_{eff} = 20.64, 24.07 and 29.51 keV) were found to agree with each other to within 4%. However, the difference between the filtered and unfiltered 50 kVp curves (E_{eff} = 20.64 and 10.72 keV, respectively) was as large as 20%. These results are consistent with the findings of Bekerat *et al.* [64], who investigated the energy dependence of an EBT3 film prototype containing aluminum. The formulation of the film active layer used in this experiment contained 1.6% aluminum in atomic percent [177].

6.5.4 Film Holder Correction Factor

The film holder correction factor defined in Eq.(6.20) was calculated. To distinguish the contribution to $k_{\text{Film Holder}}(z)$ from the holders and from the film pieces themselves, $k_{\text{Film Holder}}(z)$ was calculated with and without the presence of films. The results are shown in figure 6.4. When considering the holders only, the correction is a 0.5 to 0.7% effect, slightly increasing with depth. This depth dependence can be explained by the increased backscatter off of the base of the film holder and the lower ionization chamber holder.

When the films are included in the simulation, the correction increases from 0.8 to 1.1%. Interestingly, from the definition of $k_{\text{Film Holder}}(z)$ this result implies that the measured dose is larger when the films are present in the radiation field, despite the density of EBT3 film being larger than water (1.335 g/cm^3) [64]. Figure 6.4(bottom) compares the attenuation coefficients (calculated with XCOM [171]) of EBT3 against water. Above 21 keV EBT3 is more attenuating

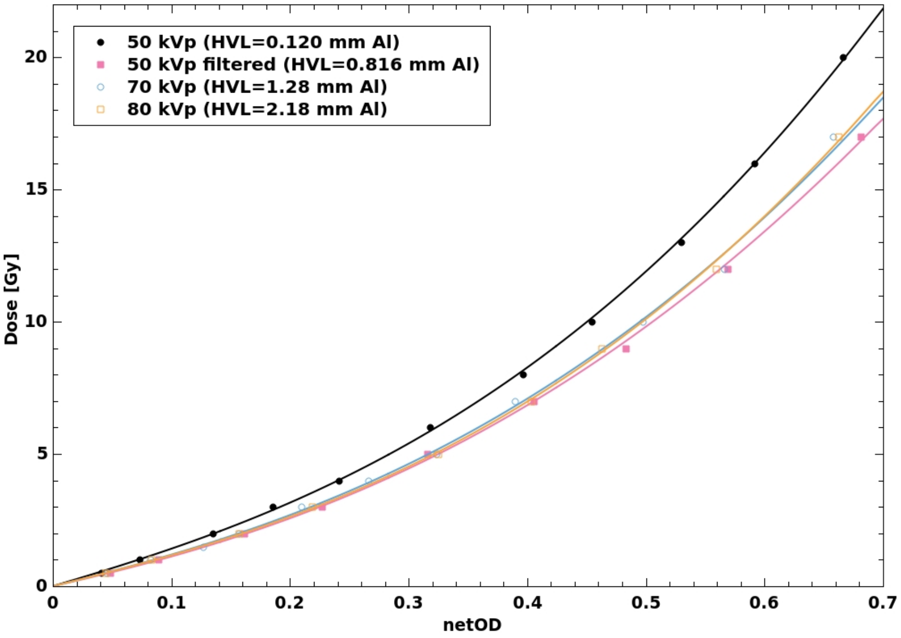

Figure 6.3 Calibration curves for EBT3 Gafchromic film (red channel) for a range of kV photon beam qualities.

than water, suggesting that the contribution from Compton scattering (proportional to material density) dominates at this energy. Below 21 keV, we see EBT3 is less attenuating than water. This can be explained by the increasing contribution from the photoelectric effect at lower photon energies ($\propto 1/E^3$) which is also proportional to Z^4. Since the effective atomic number of EBT3 is less than that of water (6.71 vs 7.42, respectively), its photoelectric attenuation coefficient is less.

6.5.5 Absorbed Dose Measurements

The depth-dose measurements as calculated by the TARGIT method of Eq.(6.2) were compared with the data provided in the source calibration file, and are shown in table 6.8. The measured values were found to agree with the calibration data to within the measurement uncertainty listed in table 6.2. The ionization chamber and film absorbed dose to water measurements are shown in figure 6.5. While the previously reported differences between the Zeiss and C_Q doses are present [48], the dose measured by the film was generally in good agreement with both methods considering the measurement uncertainties (5-6 %). At 5 and 10 mm depths in water the film dose agreed more closely with the Zeiss dose (percent difference of 1-5 %). Beyond this depth however,

Table 6.8 The depth dose rate as reported by the calibration file (calib) and as measured by the TARGIT method for INTRABEAM source XRS S/N 507299. The percent error from the calibration data was found to be within the measurement uncertainty (see table 6.2)

	Dose Rate [Gy/min]		
Depth in water [mm]	Calib	TARGIT	% Diff
5	13.24	13.93	5.2
10	2.594	2.674	3.1
15	0.9518	0.9805	3.0
20	0.4610	0.4730	2.6
25	0.2611	0.2657	1.8
30	0.1594	0.1629	2.2

the agreement was best with the C_Q dose (differences of 1-9 %). From these results, it is difficult to make any definitive statement on whether the Zeiss or C_Q ionization chamber dose calculation is more accurate relative to the film dose measurements. At all depths investigated the TARGIT dose was consistently and significantly the lowest. The percent difference from the TARGIT dose for the film, Zeiss, and C_Q dose is plotted in figure 6.6. The measured EBT3 dose was 31 to 59% greater than the TARGIT dose, while the C_Q dose was up to 80% larger (at 5 mm depth). These large discrepancies suggest that the TARGIT dose severely underestimates the physical dose to water.

6.6 Discussion

The results of this study demonstrate that the doses delivered by the INTRABEAM according to the manufacturer dose calibration file (and as measured by the TARGIT method), are in actuality significantly larger. Due to the depth dependence of the TARGIT conversion function $f'(z)$, this dose discrepancy can vary wildly depending on the depth of prescription. For example, a prescribed TARGIT dose of 20 Gy at a depth of 30 mm in water would correspond to a physical dose of 23–26 Gy (based on the ionization chamber and film results summarised in figure 6.6), while the same prescription at 5 mm would correspond to 31–36 Gy. This has implications for INTRABEAM treatments following the TARGIT-A trial protocol, where IORT was performed using an appropriately sized spherical applicator (with available radii of 7.5 mm to 25 mm) surgically placed in the tumour bed, with a prescription dose of 20 Gy to the applicator surface. Our results suggest that depending on the size of spherical applicator chosen, patients would receive differing doses. For reference, the average applicator radius used in the TARGIT-A trial was 17.5–20.0 mm [178].

While our results investigated the dosimetry for the bare source (i.e. no applicator), one could estimate the effect of the presence of a spherical applicator. The depth dose measurements shown in figure 6.5 can be determined for each spherical applicator by multiplying the dose by the applicator transfer function, defined as:

$$\mathrm{TF}_{\mathrm{app}}(z) = \frac{\dot{D}_{\mathrm{app}}(z)}{\dot{D}_{\mathrm{no\ app}}(z)}, \tag{6.22}$$

where $\dot{D}_{\mathrm{app}}(z)$ and $\dot{D}_{\mathrm{no\ app}}(z)$ are the dose rate at depth z, with and without the applicator present. The individual applicator transfer functions are provided with the source calibration file, and can also be measured by the user. Our measurement at 5 mm depth would not be relevant as the smallest applicator currently offered has a radius of 7.5 mm.

The transfer function definition of Eq.(6.22) implicitly assumes that $k_{K_a \to D_W}$, k_Q and $f'(z)$ are insensitive to the differences in beam quality between the bare source and inclusion of a spherical applicator. To estimate how spherical applicator beam quality affects C_Q, one can look at the variation in C_Q between the depth of an applicator's radii and the depth of equivalent bare source HVL. Spherical applicator HVL measurements have been reported in literature, ranging from 1.10–1.30 mm Al for applicator radii of 0.75–1.5 cm [41], and 0.85–1.09 [41] or 0.80–1.23 [136] mm Al for radii of 1.75–2.5 cm. For the larger applicators (r=1.75–2.5 cm), their HVLs of 0.8 to 1.2 mm Al correspond to the beam quality of the bare source at a shallower depth in water ($\sim$1–1.7 cm, see table 6.5), while the smaller applicator (r=0.75–1.5 cm) HVLs of 1.1 to 1.3 mm Al are similar to the bare source at greater depth ($\sim$1.5–2 cm). This difference in behaviour is due to the inclusion of an aluminum filter for applicators with radii less than 1.5 cm. From figure 6.1, the change in C_Q from spherical applicator beam quality differences is less than 3%.

Similarly, the effect of spherical applicator beam quality on the film measurements can be predicted by the change in film energy response between applicator radius and the depth of equivalent bare source HVL. Our results show that EBT3 film is energy independent to within 4% for HVL=0.816 to 2.18 mm Al, thus spherical applicators would have little effect on film measurements at 10 mm depth in water and greater. Accounting for these variations introduced into the C_Q and measurements, and noting that the transfer function is multiplicative, the percent error from the TARGIT dose shown in figure 6.6 would be relatively unchanged with the presence of a spherical applicator.

In our experience, the source dose rate could vary by 2–3% when measured on different dates. A large part of this variation can be accounted for by the dose uncertainty due to positioning error, as the source must be re-installed in the water phantom at the start of each measurement run. While our measurement method used a fixed irradiation time (thus, the measured dose was susceptible to daily dose rate variations), differences in daily dose rate are accounted for during treatment and the total irradiation time is scaled accordingly. In terms of source-to-source variations, dose rate measurements performed with another INTRABEAM source were found to differ by 15% to 5% as a function of depth in water, corresponding to a relative difference (i.e. the difference in the PDDs) of up to 10%. This is similar to previously reported source-to-source output variations [135, 179]. However, while source output variations (both day-to-day and source-to-source) would change the absolute doses reported in this work, the relative differences between the dose determination methods (i.e TARGIT, Zeiss, C_Q, film) would be unaffected.

Here, we investigated the absorbed dose to water from the INTRABEAM measured in a homogeneous water phantom. However, it is known that for low-energy photon sources water is not perfectly tissue equivalent, and tissue composition and inhomogeneities will have an impact on patient dose metrics [180]. Ebert and Carruthers reported a reduction in dose (12 % to 4 % for 10 mm and 40 mm depth) when comparing INTRABEAM dose calculations in water to in breast tissue [152]. White *et al.* noted a reduction in dose volume histogram metrics when accounting for tissue inhomogeneities in breast irradiation with the Xoft Axxent, a 50 kVp miniature x-ray tube similar to the INTRABEAM [181]. In their investigations of the minimum dose to 90% of the planning treatment volume, White *et al.* found a decrease of 4% from a homogeneous water calculation (AAPM TG-43 [182]), and as large as 40 % when reporting the dose to medium rather than dose to water.

Conversely, the source low energy photon spectrum has been shown to have a greater relative biological impact than higher energy photon sources, indicating more biological damage for the same delivered dose. In experiments studying cell inactivation, Liu *et al.* found that the relative biological effectiveness (RBE) of 50 kVp x-rays from the INTRABEAM with 4 cm diameter spherical applicator was greater than that of 6 MV x-rays. They reported mean RBE values of 1.26 to 1.42 [158], which decreased with distance from the applicator surface. White *et al.* calculated the source 4 cm applicator spectrum RBE using an MC simulation of DNA double strand breaks as the biological damage indicator. Their results showed an RBE between 1.4 and 1.6 (compared to cobalt-60) at all distances, with variability depending on tissue type [159]. Using a multiscale methodology for simulating event-by-event electron spectra, Pater found the double strand break RBE of the bare source (0 to 2 cm in water) ranged from 1.14 to 1.16 [160]. This enhanced

RBE could help to compensate for the dose reduction seen when accounting for patient tissue composition.

Clinical treatments with the INTRABEAM system have proven to be safe and effective [161, 33]. It is not the intent of this work to recommend any changes to the INTRABEAM clinical prescription doses. However, our results show that the prescription dose underestimates the physical absorbed dose to water, which has profound implications for studies investigating the relationships between dose and therapeutic effect from INTRABEAM, or comparing INTRABEAM treatments with other radiation delivery methods. Relevant examples of comparing outcomes with other radiation treatment types include breast IORT treatments performed with the Xoft Axxent source [183, 184] (ClinicalTrials.gov Identifier: NCT01644669), or treatments combining INTRABEAM IORT with external beam radiotherapy (TARGIT-B trial, ClinicalTrials.gov Identifier: NCT01792726).

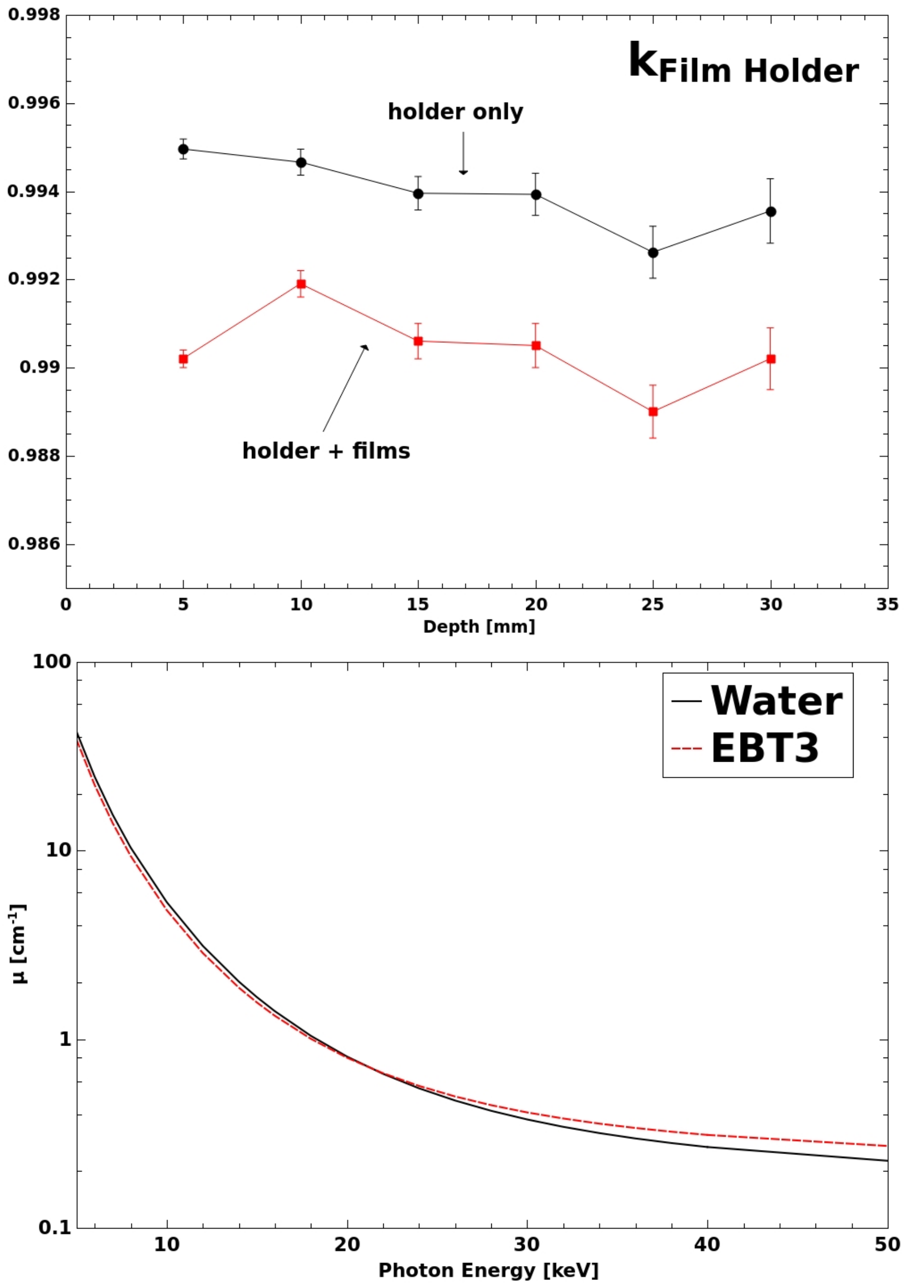

Figure 6.4 (Top) Film holder correction factor as a function of depth in water. (Bottom) Attenuation coefficient of water and EBT3 gafchromic film calculated with XCOM. The attenuation coefficient of EBT3 crosses that of water at around 21 keV due to competing effects of Compton scattering (proportional to electron density) and photoelectric effect (proportional to effective atomic number).

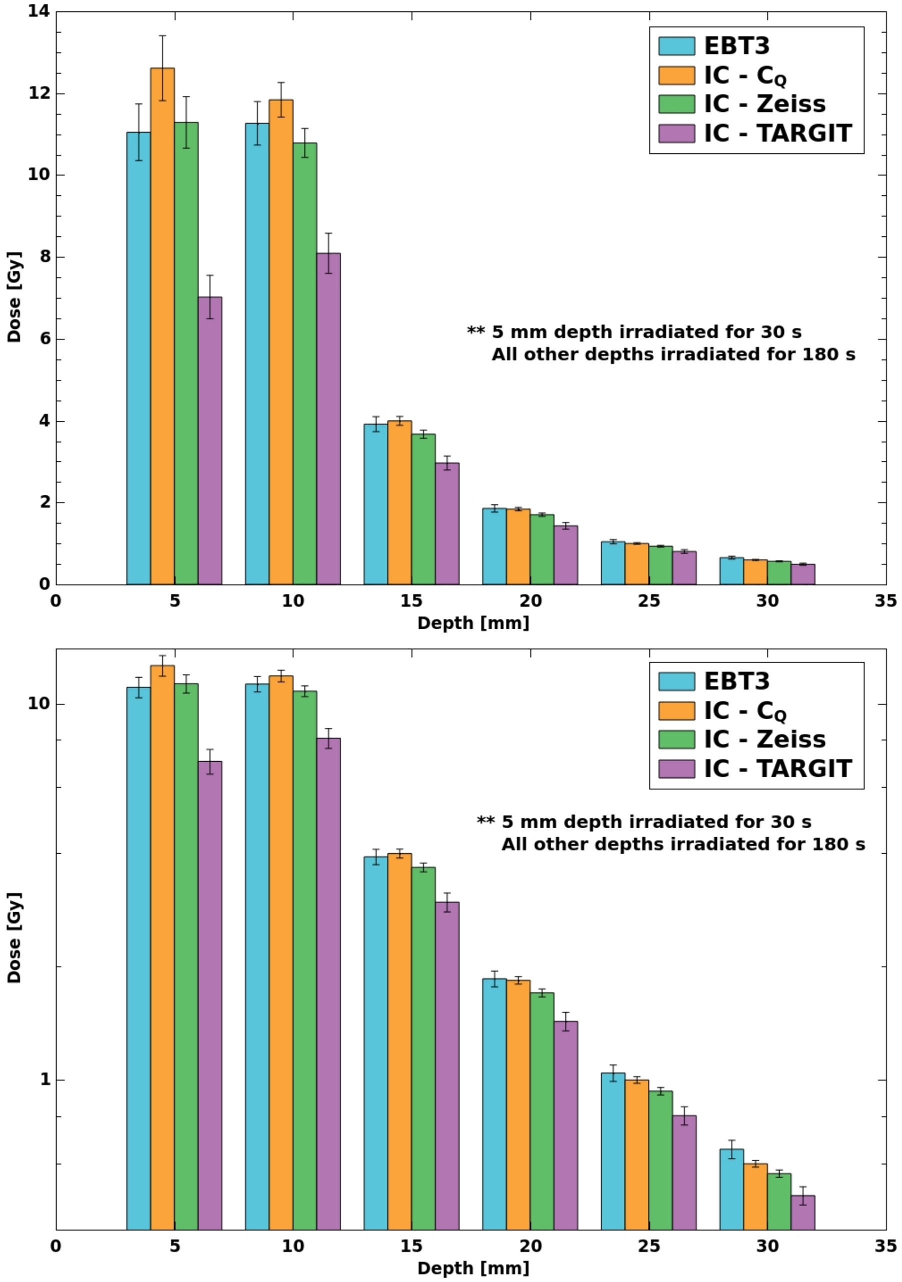

Figure 6.5 The absorbed dose to water as a function of depth, as determined with ionization chamber methods and film. Results are shown in a (top) linear and (bottom) log dose scale. At all depths, the lowest dose was measured by the TARGIT method.

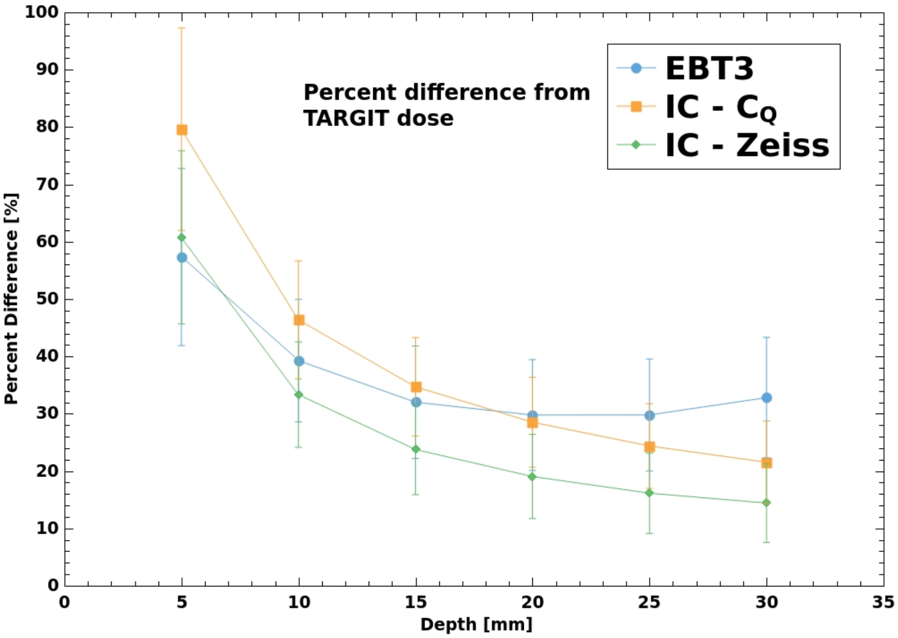

Figure 6.6 Percent difference of absorbed dose as measured with EBT3 film, and the C_Q and Zeiss ionization chamber methods compared to the TARGIT dose.

6.7 Conclusions

Accurate knowledge of the absorbed dose to water is crucial for achieving optimal treatment outcomes, and making meaningful comparisons between radiation modality treatments. The results of this work suggest that the dose delivered by the INTRABEAM system according to the TARGIT protocol severely underestimates the physical dose to water. The TARGIT dose was measured in a water phantom at depths of 5 mm to 30 mm and compared with two other ionization chamber-based dose calculations (the recommended water phantom dose formula (Zeiss), and the recent C_Q formalism of Watson *et al.* [48]), and EBT3 Gafchromic film measurements. Multiple dose response calibration curves across a range of relevant photon energies were employed to account for the energy dependence of EBT3 film. In general, the doses measured by film, and the Zeiss and C_Q methods agreed within measurement uncertainties (5-6%), while the TARGIT doses were significantly lower. The differences from the TARGIT dose ranged from 14% (Zeiss method at 30 mm depth) to as large as 80% (C_Q method at 5 mm depth). This correlation between the TARGIT dose and physical dose is important for any studies wishing to make dosimetric comparisons between the INTRABEAM and other radiation emitting devices.

6.8 Acknowledgments

The authors would like to thank J. Larkin for his professional expertise in constructing the film holder. T. Connell must also be thanked for their help with performing INTRABEAM measurements. Discussions with S. Devic offered great insight on absolute dosimetry with EBT3 films. P.W. acknowledges partial support by the CREATE Medical Physics Research Training Network grant of the Natural Sciences and Engineering Research Council (Grant No. 432290).

7

Conclusion

7.1 Summary

This work investigates the dosimetry of the INTRABEAM system, a miniature x-ray source used in IORT. An MC model of the source was created using the EGSnrc particle transport code based on published specifications (of the source probe) and specifications provided by the manufacturer (for the spherical applicators). The simulation results were validated with measurements of half-value layer performed in-air, and percent depth dose measurements in a water phantom. The effect of considering atomic relaxations with explicit $M-$ and $N-$subshells versus averaged shell energies on the simulation results was investigated, and was found to be appreciable in the determination of HVL and depth dose. The efficiency of using a phase space source of all particles leaving the surface of the INTRABEAM source probe, rather than a simulation starting with an electron source was also investigated.

A formalism relying on MC calculated dose ratios was proposed for calculating the absorbed dose to water from measurements performed in a water phantom with an air-kerma calibrated ionization chamber. When applied to the INTRABEAM source, it was found that the formalism systematically resulted in a larger dose (up to 23% greater) than the equation recommended by the manufacturer in the water phantom manual. It was also determined that the uncertainty in the plate separation of the ionization chamber used (PTW 34013) had a significant effect on the dose calculation.

The MC-derived formalism (C_Q) and manufacturer recommended (Zeiss) dose determinations were compared with the dose calculation used in the TARGIT protocol as a function of depth in water. Radiochromic film measurements of absorbed dose were also performed and compared. The dose determined by the C_Q, Zeiss, and film methods generally agreed considering measurement uncertainties (5-6%). The TARGIT dose was considerably less than the other methods by 14% to 80%, suggesting that the TARGIT dose underestimates the physical dose to water. The results presented in this work provide strong evidence that the doses delivered in breast IORT treatments following the TARGIT protocol were significantly greater than the prescription dose of 20 Gy, and varied with the size of spherical applicator used.

7.2 Future Research Directions

The work presented in this thesis provides a starting point for future investigations of the dosimetry of the INTRABEAM system and other electronic brachytherapy systems. Several possible research projects spawning from this work are listed below.

Dosimetric comparison of INTRABEAM and Xoft: Following the conclusions of this thesis, and considering that a clinical trial of breast IORT performed with the Xoft Axxent is currently underway, it would be beneficial to directly compare the absorbed dose delivered at clinically relevant depths (ex: the surface of a spherical applicator and 1 cm from the applicator surface) between the TARGIT-A and Xoft protocols. From the results and discussion outlined in Chapter 6, the absorbed dose at any distance from the surface of a given diameter INTRABEAM spherical applicator could be calculated from the measured bare probe dose (determined via C_Q method) and applicator transfer function. The absorbed dose delivered by the Xoft Axxent at the same depths could be calculated using published TG-43 data [99]. The calculated doses for the INTRABEAM and Xoft at the relevant depths in water could then be experimentally verified with EBT3 Gafchromic film measurements following the same procedure as in Chapter 6. This dosimetric information would greatly inform the discussions and conclusions of any studies wishing to compare the results of the TARGIT-A and Xoft trials.

Investigate the use of another ionization chamber for C_Q dose measurement: One of the conclusions of the study presented in Chapter 5 was that the uncertainty in the plate separation distance of the PTW 34013 chamber had a significant effect on the value of C_Q, which manifested as a component of measurement uncertainty (1.2% to 3.5%) using the C_Q method described in Chapter 6. This uncertainty could be greatly reduced by using a soft x-ray ionization chamber with more precisely known dimensions, for example an Exradin A20 (Standard Imaging) parallel plate chamber with an arguably better-defined effective point of measurement. The procedure for determining C_Q as described in Chapter 5 could be applied to this chamber, allowing for a more precise measurement of absorbed dose to water from the INTRABEAM in a water phantom.

Calculate TG-43 parameters for INTRABEAM: As discussed in Chapter 2, the current dosimetry formalism for brachytherapy sources is described by the AAPM TG-43 report [182, 97], and most commercial brachytherapy treatment planning software utilize this formalism. Using the EGSnrc source model presented in this work, it would be straightforward to calculate the TG-43 dosimetry parameters (i.e., the radial dose function $g_L(r)$ and anisotropy function $F(r,\theta)$) for the INTRABEAM source, similar to the approach taken by Rivard *et al.* for the Xoft Axxent[99]. The INTRABEAM MC model presented in this thesis investigated the dose along the source longitudinal axis only ($\theta = 180^\circ$), thus it would be necessary to validate the model dose distributions in 2D (r,θ) with experimental measurements prior to performing calculations of $F(r,\theta)$.

Patient-specific dose calculation and dose tracking, optimisation of combined IORT/EBRT treatment: One limitation of the TG-43 approach is that it treats the patient as a homogeneous volume of water, which can lead to dose calculation inaccuracies in regions with large tissue heterogeneity, particularly between soft tissue and bone [185]. These inaccuracies could be evaluated by performing patient-specific dose calculations using the INTRABEAM MC model (following validation in (r,θ)). The 3D patient dose distributions could be calculated using information from patient CT images (treatment planning CT and/or cone beam CT performed prior to IORT procedure), similar to the work of Bouzid *et al.* [186] and Schneider *et al.* [187], by associating voxel CT number to tissue type and electron density. From these dose distributions, the dose to the target tissues and organs at risk could be assessed and compared with TG-43 calculations.

The patient-specific MC-calculated doses would also be useful for investigating the cumulative dose to target tissues and organs at risk in treatments combining IORT with EBRT (such as in the TARGIT-B trial). This information would be valuable for studying correlations between patient toxicity and delivered dose. Using dose volume histogram constraints, one could investigate the dosimetric optimisation of combined IORT/EBRT treatments. The optimisation could also take into consideration the differences in radiobiological effects of the INTRABEAM 50 kVp spectrum and MV photons.

7.3 Outlook

The INTRABEAM miniature x-ray source offers potential benefits to breast cancer patients undergoing APBI with IORT compared with WBI. The findings of this thesis identify the limitations of the INTRABEAM system dosimetry, and propose a more accurate formalism for determining the absorbed dose to water. Improving the system dosimetry allows for greater confidence in the dose delivered to patients, and will help to encourage the investigation and adoption of INTRABEAM IORT at other cancer sites.

Bibliography

[1] F. Schneider, H. Fuchs, F. Lorenz, V. Steil, F. Ziglio, U. Kraus-Tiefenbacher, F. Lohr, and F. Wenz, "A novel device for intravaginal electronic brachytherapy," *International Journal of Radiation Oncology• Biology• Physics*, vol. 74, no. 4, pp. 1298–1305, 2009.

[2] A. Sethi, B. Emami, W. Small Jr, and T. O. Thomas, "intraoperative radiotherapy with intrabeam: Technical and dosimetric considerations," *Frontiers in oncology*, vol. 8, p. 74, 2018.

[3] D. R. Holmes, M. Baum, and D. Joseph, "The targit trial: targeted intraoperative radiation therapy versus conventional postoperative whole-breast radiotherapy after breast-conserving surgery for the management of early-stage invasive breast cancer (a trial update)," *The American Journal of Surgery*, vol. 194, no. 4, pp. 507–510, 2007.

[4] J. Yanch and K. Harte, "Monte carlo simulation of a miniature, radiosurgery x-ray tube using the its 3.0 coupled electron-photon transport code," *Med. Phys.*, vol. 23, no. 9, pp. 1551–1558, 1996.

[5] O. Nwankwo, S. Clausen, F. Schneider, and F. Wenz, "A virtual source model of a kilo-voltage radiotherapy device," *Phys. Med. Biol.*, vol. 58, no. 7, p. 2363, 2013.

[6] P. G. Watson and J. Seuntjens, "Effect of explicit m and n-shell atomic transitions on a low-energy x-ray source," *Medical physics*, vol. 43, no. 4, pp. 1760–1763, 2016.

[7] J. Ferlay, I. Soerjomataram, R. Dikshit, S. Eser, C. Mathers, M. Rebelo, D. M. Parkin, D. Forman, and F. Bray, "Cancer incidence and mortality worldwide: sources, methods and major patterns in globocan 2012," *International journal of cancer*, vol. 136, no. 5, 2015.

[8] C. C. S. A. C. on Cancer Statistics, "Canadian cancer statistics 2017." http://www.cancer.ca/Canadian-Cancer-Statistics-2017-EN.pdf, 2017. Accessed: 2018-04-11.

[9] R. Lakhtakia, "A brief history of breast cancer: Part i: Surgical domination reinvented," *Sultan Qaboos University Medical Journal*, vol. 14, no. 2, p. e166, 2014.

[10] W. S. Halsted, "I. the results of operations for the cure of cancer of the breast performed at the johns hopkins hospital from june, 1889, to january, 1894.," *Annals of Surgery*, vol. 20, no. 5, p. 497–555, 1894.

[11] B. Fisher, M. Bauer, R. Margolese, R. Poisson, Y. Pilch, C. Redmond, E. Fisher, N. Wolmark, M. Deutsch, E. Montague, *et al.*, "Five-year results of a randomized clinical trial comparing total mastectomy and segmental mastectomy with or without radiation in the treatment of breast cancer," *New England Journal of Medicine*, vol. 312, no. 11, pp. 665–673, 1985.

[12] B. Fisher, S. Anderson, J. Bryant, R. G. Margolese, M. Deutsch, E. R. Fisher, J.-H. Jeong, and N. Wolmark, "Twenty-year follow-up of a randomized trial comparing total mastectomy, lumpectomy, and lumpectomy plus irradiation for the treatment of invasive breast cancer," *New England Journal of Medicine*, vol. 347, no. 16, pp. 1233–1241, 2002.

[13] E. B. C. T. C. Group *et al.*, "Effect of radiotherapy after breast-conserving surgery on 10-year recurrence and 15-year breast cancer death: meta-analysis of individual patient data for 10 801 women in 17 randomised trials," *The Lancet*, vol. 378, no. 9804, pp. 1707–1716, 2011.

[14] R. Lakhtakia and I. Burney, "A brief history of breast cancer: Part iii-tumour biology lays the foundation for medical oncology," *Sultan Qaboos University Medical Journal*, vol. 15, no. 1, p. e34, 2015.

[15] W. F. Athas, M. Adams-Cameron, W. C. Hunt, A. Amir-Fazli, and C. R. Key, "Travel distance to radiation therapy and receipt of radiotherapy following breast-conserving surgery," *Journal of the National Cancer Institute*, vol. 92, no. 3, pp. 269–271, 2000.

[16] D. W. Arthur and F. A. Vicini, "Accelerated partial breast irradiation as a part of breast conservation therapy," *Journal of clinical oncology*, vol. 23, no. 8, pp. 1726–1735, 2005.

[17] R. Holland, S. H. Veling, M. Mravunac, and J. H. Hendriks, "Histologic multifocality of tis, t1–2 breast carcinomas implications for clinical trials of breast-conserving surgery," *Cancer*, vol. 56, no. 5, pp. 979–990, 1985.

[18] J. Vaidya, J. Vyas, R. Chinoy, N. Merchant, O. Sharma, and I. Mittra, "Multicentricity of breast cancer: whole-organ analysis and clinical implications," *British journal of cancer*, vol. 74, no. 5, p. 820, 1996.

[19] P. D. Beitsch, S. F. Shaitelman, and F. A. Vicini, "Accelerated partial breast irradiation," *Journal of surgical oncology*, vol. 103, no. 4, pp. 362–368, 2011.

[20] V. Strnad, O. J. Ott, G. Hildebrandt, D. Kauer-Dorner, H. Knauerhase, T. Major, J. Lyczek, J. L. Guinot, J. Dunst, C. G. Miguelez, *et al.*, "5-year results of accelerated partial breast irradiation using sole interstitial multicatheter brachytherapy versus whole-breast irradiation with boost after breast-conserving surgery for low-risk invasive and in-situ carcinoma of the female breast: a randomised, phase 3, non-inferiority trial," *The Lancet*, vol. 387, no. 10015, pp. 229–238, 2016.

[21] C. Polgár, O. J. Ott, G. Hildebrandt, D. Kauer-Dorner, H. Knauerhase, T. Major, J. Lyczek, J. L. Guinot, J. Dunst, C. G. Miguelez, *et al.*, "Late side-effects and cosmetic results of accelerated partial breast irradiation with interstitial brachytherapy versus whole-breast

irradiation after breast-conserving surgery for low-risk invasive and in-situ carcinoma of the female breast: 5-year results of a randomised, controlled, phase 3 trial," *The Lancet Oncology*, vol. 18, no. 2, pp. 259–268, 2017.

[22] C. Shah, F. Vicini, S. F. Shaitelman, J. Hepel, M. Keisch, D. Arthur, A. J. Khan, R. Kuske, R. Patel, and D. E. Wazer, "The american brachytherapy society consensus statement for accelerated partial-breast irradiation," *Brachytherapy*, vol. 17, no. 1, pp. 154–170, 2018.

[23] F. Vicini, P. Beitsch, C. Quiet, M. Gittleman, V. Zannis, R. Fine, P. Whitworth, H. Kuerer, B. Haffty, M. Keisch, *et al.*, "Five-year analysis of treatment efficacy and cosmesis by the american society of breast surgeons mammosite breast brachytherapy registry trial in patients treated with accelerated partial breast irradiation," *International Journal of Radiation Oncology• Biology• Physics*, vol. 79, no. 3, pp. 808–817, 2011.

[24] L. W. Cuttino, D. W. Arthur, F. Vicini, D. Todor, T. Julian, and N. Mukhopadhyay, "Long-term results from the contura multilumen balloon breast brachytherapy catheter phase 4 registry trial," *International Journal of Radiation Oncology• Biology• Physics*, vol. 90, no. 5, pp. 1025–1029, 2014.

[25] I. A. Olivotto, T. J. Whelan, S. Parpia, D.-H. Kim, T. Berrang, P. T. Truong, I. Kong, B. Cochrane, A. Nichol, I. Roy, *et al.*, "Interim cosmetic and toxicity results from rapid: a randomized trial of accelerated partial breast irradiation using three-dimensional conformal external beam radiation therapy," *Journal of Clinical Oncology*, vol. 31, no. 32, pp. 4038–4045, 2013.

[26] T. Julian, J. Costantino, F. Vicini, J. White, K. Winter, D. Arthur, R. Kuske, R. Rabinovitch, W. Curran, and N. Wolmark, "Early toxicity results with 3-d conformal external beam therapy (cebt) from the nsabp b-39/rtog 0413 accelerated partial breast irradiation (apbi) trial," *International Journal of Radiation Oncology• Biology• Physics*, vol. 81, no. 2, p. S7, 2011.

[27] E. A. Mellon, R. Sreeraman, B. J. Gebhardt, A. Mierzejewski, and C. R. Correa, "Impact of radiation treatment parameters and adjuvant systemic therapy on cosmetic outcomes after accelerated partial breast irradiation using 3-dimensional conformal radiation therapy technique," *Practical radiation oncology*, vol. 4, no. 3, pp. e159–e166, 2014.

[28] C. Shah, T. Lanni, J. B. Wilkinson, M. Jawad, J. Wobb, S. Berry, M. Wallace, P. Chen, and I. S. Grills, "Cost-effectiveness of 3-dimensional conformal radiotherapy and applicator-based brachytherapy in the delivery of accelerated partial breast irradiation," *American journal of clinical oncology*, vol. 37, no. 2, pp. 172–176, 2014.

[29] L. Livi, I. Meattini, L. Marrazzo, G. Simontacchi, S. Pallotta, C. Saieva, F. Paiar, V. Scotti, C. D. L. Cardillo, P. Bastiani, *et al.*, "Accelerated partial breast irradiation using intensity-modulated radiotherapy versus whole breast irradiation: 5-year survival analysis of a phase 3 randomised controlled trial," *European journal of cancer*, vol. 51, no. 4, pp. 451–463, 2015.

[30] C. E. Coles, C. L. Griffin, A. M. Kirby, J. Titley, R. K. Agrawal, A. Alhasso, I. S. Bhattacharya, A. M. Brunt, L. Ciurlionis, C. Chan, *et al.*, "Partial-breast radiotherapy after breast conservation surgery for patients with early breast cancer (uk import low trial): 5-year results from a multicentre, randomised, controlled, phase 3, non-inferiority trial," *The Lancet*, vol. 390, no. 10099, pp. 1048–1060, 2017.

[31] F. W. Hensley, "Present state and issues in iort physics," *Radiation Oncology*, vol. 12, no. 1, p. 37, 2017.

[32] U. Veronesi, R. Orecchia, P. Maisonneuve, G. Viale, N. Rotmensz, C. Sangalli, A. Luini, P. Veronesi, V. Galimberti, S. Zurrida, *et al.*, "Intraoperative radiotherapy versus external radiotherapy for early breast cancer (eliot): a randomised controlled equivalence trial," *The lancet oncology*, vol. 14, no. 13, pp. 1269–1277, 2013.

[33] J. S. Vaidya, F. Wenz, M. Bulsara, J. S. Tobias, D. J. Joseph, M. Keshtgar, H. L. Flyger, S. Massarut, M. Alvarado, C. Saunders, *et al.*, "Risk-adapted targeted intraoperative radiotherapy versus whole-breast radiotherapy for breast cancer: 5-year results for local control and overall survival from the targit-a randomised trial," *The Lancet*, vol. 383, no. 9917, pp. 603–613, 2014.

[34] J. S. Vaidya, M. Bulsara, F. Wenz, D. Joseph, C. Saunders, S. Massarut, H. Flyger, W. Eiermann, M. Alvarado, L. Esserman, *et al.*, "Pride, prejudice, or science: Attitudes towards the results of the targit-a trial of targeted intraoperative radiation therapy for breast cancer," *International Journal of Radiation Oncology• Biology• Physics*, vol. 92, no. 3, pp. 491–497, 2015.

[35] W. Small, T. O. Thomas, M. Alvarado, M. Baum, M. Bulsara, R. Diaz, E. Donnelly, S. Feldman, S. Grobmyer, R. Hoefer, *et al.*, "Commentary on" accelerated partial breast irradiation consensus statement: Update of an astro evidence-based consensus statement"," *Practical radiation oncology*, vol. 7, no. 3, pp. e159–e163, 2017.

[36] C. Shah, J. Wobb, and A. Khan, "Intraoperative radiation therapy in breast cancer: still not ready for prime time," *Annals of surgical oncology*, vol. 23, no. 6, pp. 1796–1798, 2016.

[37] R. M. Douglas, J. Beatty, K. Gall, R. F. Valenzuela, P. Biggs, P. Okunieff, and F. S. Pardo, "Dosimetric results from a feasibility study of a novel radiosurgical source for irradiation of intracranial metastases," *International Journal of Radiation Oncology* Biology* Physics*, vol. 36, no. 2, pp. 443–450, 1996.

[38] M. Dinsmore, K. Harte, A. Sliski, D. Smith, P. Nomikos, M. Dalterio, A. Boom, W. Leonard, P. Oettinger, and J. Yanch, "A new miniature x-ray source for interstitial radiosurgery: Device description," *Med. Phys.*, vol. 23, no. 1, pp. 45–52, 1996.

[39] J. Beatty, P. Biggs, K. Gall, P. Okunieff, F. Pardo, K. Harte, M. Dalterio, and A. Sliski, "A new miniature x-ray device for interstitial radiosurgery: Dosimetry," *Medical physics*, vol. 23, no. 1, pp. 53–62, 1996.

[40] T. Yasuda, J. Beatty, P. Biggs, and K. Gall, "Two-dimensional dose distribution of a miniature x-ray device for stereotactic radiosurgery," *Medical physics*, vol. 25, no. 7, pp. 1212–1216, 1998.

[41] D. Eaton and S. Duck, "Dosimetry measurements with an intra-operative x-ray device," *Physics in medicine and biology*, vol. 55, no. 12, p. N359, 2010.

[42] F. Schneider, F. Greineck, S. Clausen, S. Mai, U. Obertacke, T. Reis, and F. Wenz, "Development of a novel method for intraoperative radiotherapy during kyphoplasty for spinal metastases (kypho-iort)," *International Journal of Radiation Oncology• Biology• Physics*, vol. 81, no. 4, pp. 1114–1119, 2011.

[43] M. Goubert and L. Parent, "Dosimetric characterization of intrabeam® miniature accelerator flat and surface applicators for dermatologic applications," *Physica Medica: European Journal of Medical Physics*, vol. 31, no. 3, pp. 224–232, 2015.

[44] S. Guo, C. A. Reddy, M. Kolar, N. Woody, A. Mahadevan, F. C. Deibel, D. W. Dietz, F. H. Remzi, and J. H. Suh, "Intraoperative radiation therapy with the photon radiosurgery system in locally advanced and recurrent rectal cancer: retrospective review of the cleveland clinic experience," *Radiation oncology*, vol. 7, no. 1, p. 110, 2012.

[45] F. A. Giordano, S. Brehmer, Y. Abo-Madyan, G. Welzel, E. Sperk, A. Keller, F. Schneider, S. Clausen, C. Herskind, P. Schmiedek, *et al.*, "Intrago: intraoperative radiotherapy in glioblastoma multiforme–a phase i/ii dose escalation study," *BMC cancer*, vol. 14, no. 1, p. 992, 2014.

[46] F. A. Giordano, S. Brehmer, B. Mürle, G. Welzel, E. Sperk, A. Keller, Y. Abo-Madyan, E. Scherzinger, S. Clausen, F. Schneider, *et al.*, "Intraoperative radiotherapy in newly diagnosed glioblastoma (intrago): An open-label, dose-escalation phase i/ii trial," *Neurosurgery*.

[47] D. van der Merwe, J. Van Dyk, B. Healy, E. Zubizarreta, J. Izewska, B. Mijnheer, and A. Meghzifene, "Accuracy requirements and uncertainties in radiotherapy: a report of the international atomic energy agency," *Acta Oncologica*, vol. 56, no. 1, pp. 1–6, 2017.

[48] P. G. F. Watson, M. Popovic, and J. Seuntjens, "Determination of absorbed dose to water from a miniature kilovoltage x-ray source using a parallel-plate ionization chamber," *Physics in Medicine and Biology*, 2017.

[49] P. G. F. Watson, H. Bekerat, P. Papaconstadopoulos, S. Davis, and J. Seuntjens, "An investigation into the intrabeam miniature x-ray source dosimetry using ionization chamber and radiochromic film measurements," *Medical Physics*, vol. 45, no. 9, pp. 4274–4286.

[50] P. Andreo, D. Burns, A. Nahum, J. Seuntjens, and F. Attix, *Fundamentals of Ionizing Radiation Dosimetry*. Wiley, 2017.

[51] CCEMRI, "Report of the 11th session of the comit$\acute{e}$ consultatif pour les etalons de mesures des rayonnements ionisants (s$\grave{e}$vres: Bureau international des poids et mesures)."

[52] S. Seltzer, J. Fernández-Varea, P. Andreo, P. Bergstrom, D. Burns, I. K. Bronić, C. Ross, and F. Salvat, "Key data for ionizing-radiation dosimetry: measurement standards and applications, icru report 90," 2016.

[53] H. Buhr, L. Büermann, M. Gerlach, M. Krumrey, and H. Rabus, "Measurement of the mass energy-absorption coefficient of air for x-rays in the range from 3 to 60 kev," *Physics in Medicine & Biology*, vol. 57, no. 24, p. 8231, 2012.

[54] C.-M. Ma, C. Coffey, L. DeWerd, C. Liu, R. Nath, S. Seltzer, and J. Seuntjens, "Aapm protocol for 40–300 kv x-ray beam dosimetry in radiotherapy and radiobiology," *Medical physics*, vol. 28, no. 6, pp. 868–893, 2001.

[55] P. Andreo, D. Burns, K. Hohlfeld, M. S. Huq, T. Kanai, F. Laitano, V. Smyth, and S. Vynckier, "Iaea trs-398. absorbed dose determination in external beam radiotherapy: an international code of practice for dosimetry based on standards of absorbed dose to water," *International Atomic Energy Agency*, 2000.

[56] K. Rosser, "An alternative beam quality index for medium-energy x-ray dosimetry," *Physics in Medicine & Biology*, vol. 43, no. 3, p. 587, 1998.

[57] U. Chica, M. Anguiano, M. Vilches, and A. Lallena, "Quality indexes based on water measurements for low and medium energy x-ray beams: A theoretical study with penelope," *Medical physics*, vol. 41, no. 1, 2014.

[58] J. Boag, "Ionization chambers," *The dosimetry of ionizing radiation*, vol. 2, pp. 169–243, 1987.

[59] W. L. McLaughlin, C. Yun-Dong, C. G. Soares, A. Miller, G. Van Dyk, and D. F. Lewis, "Sensitometry of the response of a new radiochromic film dosimeter to gamma radiation and electron beams," *Nuclear Instruments and Methods in Physics Research Section A: Accelerators, Spectrometers, Detectors and Associated Equipment*, vol. 302, no. 1, pp. 165–176, 1991.

[60] S. Devic, N. Tomic, and D. Lewis, "Reference radiochromic film dosimetry: review of technical aspects," *Physica Medica*, vol. 32, no. 4, pp. 541–556, 2016.

[61] A. Sarfehnia, I. Kawrakow, and J. Seuntjens, "Direct measurement of absorbed dose to water in hdr i192r brachytherapy: Water calorimetry, ionization chamber, gafchromic film, and tg-43," *Medical physics*, vol. 37, no. 4, pp. 1924–1932, 2010.

[62] T. A. Brown, K. R. Hogstrom, D. Alvarez, K. L. Matthews, K. Ham, and J. P. Dugas, "Dose-response curve of ebt, ebt2, and ebt3 radiochromic films to synchrotron-produced monochromatic x-ray beams," *Medical physics*, vol. 39, no. 12, pp. 7412–7417, 2012.

[63] M. J. Butson, K. Peter, T. Cheung, and H. Alnawaf, "Energy response of the new ebt2 radiochromic film to x-ray radiation," *Radiation Measurements*, vol. 45, no. 7, pp. 836–839, 2010.

[64] H. Bekerat, S. Devic, F. DeBlois, K. Singh, A. Sarfehnia, J. Seuntjens, S. Shih, X. Yu, and D. Lewis, "Improving the energy response of external beam therapy (ebt) gafchromictm dosimetry films at low energies ($\leq$ 100 kev)," *Medical physics*, vol. 41, no. 2, 2014.

[65] G. Massillon-JL, I. D. Muñoz-Molina, and P. Díaz-Aguirre, "Optimum absorbed dose versus energy response of gafchromic ebt2 and ebt3 films exposed to 20–160 kv x-rays and 60co gamma," *Biomedical Physics & Engineering Express*, vol. 2, no. 4, p. 045005, 2016.

[66] S. C. Peet, R. Wilks, T. Kairn, J. V. Trapp, and S. B. Crowe, "Calibrating radiochromic film in beams of uncertain quality," *Medical physics*, vol. 43, no. 10, pp. 5647–5652, 2016.

[67] L. Spencer and F. Attix, "A theory of cavity ionization," *Radiation Research*, vol. 3, no. 3, pp. 239–254, 1955.

[68] A. Nahum, "Water/air mass stopping power ratios for megavoltage photon and electron beams," *Physics in Medicine & Biology*, vol. 23, no. 1, p. 24, 1978.

[69] T. Burlin, "A general theory of cavity ionisation," *The British journal of radiology*, vol. 39, no. 466, pp. 727–734, 1966.

[70] E. B. Podgorsak, "Review of radiation oncology physics: a handbook for teachers and students," *Vienna, Austria: IAE Agency*, 2003.

[71] J. Sempau, P. Andreo, J. Aldana, J. Mazurier, and F. Salvat, "Electron beam quality correction factors for plane-parallel ionization chambers: Monte carlo calculations using the penelope system," *Physics in Medicine & Biology*, vol. 49, no. 18, p. 4427, 2004.

[72] P. N. Mobit, A. E. Nahum, and P. Mayles, "An egs4 monte carlo examination of general cavity theory," *Physics in Medicine & Biology*, vol. 42, no. 7, p. 1319, 1997.

[73] S. M. Seltzer, P. J. Lamperti, R. Loevinger, M. G. Mitch, J. T. Weaver, and B. M. Coursey, "New national air-kerma-strength standards for 125i and 103pd brachytherapy seeds," *Journal of research of the National Institute of Standards and Technology*, vol. 108, no. 5, p. 337, 2003.

[74] J. Seuntjens, H. Thierens, and U. Schneider, "Correction factors for a cylindrical ionization chamber used in medium-energy x-ray beams," *Physics in Medicine & Biology*, vol. 38, no. 6, p. 805, 1993.

[75] L. De Prez and J. de Pooter, "The new nmi orthovolt x-rays absorbed dose to water primary standard based on water calorimetry," *Physics in Medicine & Biology*, vol. 53, no. 13, p. 3531, 2008.

[76] A. Krauss, L. Büermann, H.-M. Kramer, and H.-J. Selbach, "Calorimetric determination of the absorbed dose to water for medium-energy x-rays with generating voltages from 70 to 280 kv," *Physics in Medicine & Biology*, vol. 57, no. 19, p. 6245, 2012.

[77] B. Rapp, N. Perichon, M. Denoziere, J. Daures, A. Ostrowsky, and J. Bordy, "The lne-lnhb water calorimeter for primary measurement of absorbed dose at low depth in water: application to medium-energy x-rays," *Physics in Medicine & Biology*, vol. 58, no. 9, p. 2769, 2013.

[78] S. M. Seltzer, M. O'Brien, and M. G. Mitch, "New national air-kerma standard for low-energy electronic brachytherapy sources," *Journal of research of the National Institute of Standards and Technology*, vol. 119, p. 554, 2014.

[79] S. D. Davis, *Air-kerma strength determination of a miniature x-ray source for brachytherapy applications*. PhD thesis, University of Wisconsin-Madison, 2009.

[80] L. A. DeWerd, W. S. Culberson, J. A. Micka, and S. J. Simiele, "A modified dose calculation formalism for electronic brachytherapy sources," *Brachytherapy*, vol. 14, no. 3, pp. 405–408, 2015.

[81] "Emrp metrology for external radiotherapy." http://radiotherapy-emrp.eu/. Accessed: 2018-03-25.

[82] T. Schneider, "The ptb primary standard for the absorbed-dose to water for i-125 interstitial brachytherapy sources," *Metrologia*, vol. 49, no. 5, p. S198, 2012.

[83] T. Schneider, D. Radeck, and J. Šolc, "Development of a new primary standard for the realization of the absorbed dose to water for electronic brachytherapy x-ray sources," *Brachytherapy*, vol. 15, pp. S27–S28, 2016.

[84] S. T and Šolc J, "Realization of the absorbed dose to water for electronic brachytherapy x-ray sources," in *2nd Int. Conf. on Advances in Radiation Oncology*, (Vienna), p. 211, 2017.

[85] C.-m. Ma and A. Nahum, "Bragg-gray theory and ion chamber dosimetry for photon beams," *Physics in medicine & biology*, vol. 36, no. 4, p. 413, 1991.

[86] R. Hill, B. Healy, L. Holloway, Z. Kuncic, D. Thwaites, and C. Baldock, "Advances in kilovoltage x-ray beam dosimetry," *Physics in Medicine & Biology*, vol. 59, no. 6, p. R183, 2014.

[87] DIN, "Clinical dosimetry: Application of x rays with peak voltages between 10 and 100 kv in radiotherapy and soft tissue diagnostics. deutsche norm din 6809-4. deutsches institut fur normung, berlin (in german)."

[88] DIN, "Clinical dosimetry-part 5: Application of x rays with peak voltages between 100 and 400 kv in radiotherapy. deutsche norm din 6809-5. deutsches institut fur normung, berlin (in german)."

[89] S. Klevenhagen, R. Aukett, R. Harrison, C. Moretti, A. Nahum, K. Rosser, *et al.*, "The ipemb code of practice for the determination of absorbed dose for x-rays below 300 kv generating potential (0.035 mm al-4 mm cu hvl; 10-300 kv generating potential)," *Physics in medicine and biology*, vol. 41, no. 12, p. 2605, 1996.

[90] R. J. Aukett, J. E. Burns, A. G. Greener, R. M. Harrison, C. Moretti, A. E. Nahum, and K. E. Rosser, “Addendum to the ipemb code of practice for the determination of absorbed dose for x-rays below 300 kv generating potential (0.035 mm al–4 mm cu hvl),” *Physics in Medicine and Biology*, vol. 50, no. 12, p. 2739, 2005.

[91] T. Grimbergen, A. Aalbers, B. Mijnheer, J. Seuntjens, H. Thierens, J. Van Dam, F. Wittkämper, and J. Zoetelief, “Ncs - dosimetry of low and medium energy x rays, a code of practice for use in radiotherapy and radiobiology. report ncs-10, nederlandse commissie voor stralingsdosimetrie, amsterdam.”

[92] P. Andreo, J. Cunningham, K. Hohlfeld, and H. Svensson, “Iaea trs-277. absorbed dose determination in photon and electron beams: An international code of practice,” *International Atomic Energy Agency*, 1987.

[93] P. Andreo, J. Cunningham, K. Hohlfeld, and H. Svensson, “Iaea trs-277 2nd edn. absorbed dose determination in photon and electron beams: An international code of practice,” *International Atomic Energy Agency*, 1997.

[94] ICRU, “Dosimetry of beta rays and low-energy photons for brachytherapy with sealed sources. icru report 72. bethesda, md.”

[95] T. Sander, “Air kerma and absorbed dose standards for reference dosimetry in brachytherapy,” *The British journal of radiology*, vol. 87, no. 1041, p. 20140176, 2014.

[96] AAPM, “Specification of brachytherapy source strength. aapm report no. 21, american institute of physics, new york.”

[97] M. J. Rivard, B. M. Coursey, L. A. DeWerd, W. F. Hanson, M. Saiful Huq, G. S. Ibbott, M. G. Mitch, R. Nath, and J. F. Williamson, “Update of aapm task group no. 43 report: A revised aapm protocol for brachytherapy dose calculations,” *Medical physics*, vol. 31, no. 3, pp. 633–674, 2004.

[98] R. Nath, L. L. Anderson, G. Luxton, K. A. Weaver, J. F. Williamson, and A. S. Meigooni, “Dosimetry of interstitial brachytherapy sources: recommendations of the aapm radiation therapy committee task group no. 43,” *Medical physics*, vol. 22, no. 2, pp. 209–234, 1995.

[99] M. J. Rivard, S. D. Davis, L. A. DeWerd, T. W. Rusch, and S. Axelrod, “Calculated and measured brachytherapy dosimetry parameters in water for the xoft axxent x-ray source: An electronic brachytherapy sourcea),” *Med. Phys.*, vol. 33, no. 11, pp. 4020–4032, 2006.

[100] F. Schneider, S. Clausen, and D. J. Eaton, “Quality assurance and commissioning,” in *Targeted intraoperative radiotherapy in oncology*, pp. 31–36, Springer, 2014.

[101] I. C. on Radiation Units, *Radiation Dosimetry: X Rays Generated at Potentials of 5 to 150 KV.*, vol. 17. International Commission on Radiation Units and Measurements, 1970.

[102] C. Z. M. AG, “Intrabeam water phantom - instructions for use.” G-30-1767-en Version 5.0.

[103] C. Z. M. AG, “Acceptance test for intrabeam system.” SM-30-8023-A40-en Version 13.0.

[104] N. Metropolis, “Los alamos science,” *Special Issue*, vol. 125, 1987.

[105] N. Metropolis and S. Ulam, “The monte carlo method,” *Journal of the American statistical association*, vol. 44, no. 247, pp. 335–341, 1949.

[106] M. J. Berger, “Monte carlo calculation of the penetration and diffusion of fast charged particles,” tech. rep., 1963.

[107] I. Kawrakow, E. Mainegra-Hing, D. W. O. Rogers, F. Tessier, and B. R. B. Walters, “The EGSnrc code system: Monte Carlo simulation of electron and photon transport,” Tech. Rep. PIRS-701, National Research Council Canada, 2015.

[108] W. R. Nelson, D. W. Rogers, and H. Hirayama, “The egs4 code system,” tech. rep., 1985.

[109] F. Sauter, “Über den atomaren photoeffekt in der k-schale nach der relativistischen wellenmechanik diracs,” *Annalen der Physik*, vol. 403, no. 4, pp. 454–488, 1931.

[110] L. Brown and R. Feynman, “Radiative corrections to compton scattering,” *Physical Review*, vol. 85, no. 2, p. 231, 1952.

[111] J. H. Hubbell and I. Øverbø, “Relativistic atomic form factors and photon coherent scattering cross sections,” *Journal of Physical and Chemical Reference Data*, vol. 8, no. 1, pp. 69–106, 1979.

[112] V. Votruba, “V. votruba, bull. intern. acad. tcheque sci. 49, 19 (1948),” *Bull. Intern. Acad. Tschèque sci.*, vol. 49, p. 19, 1948.

[113] K. Mork, “Pair production by photons on electrons,” *Physical Review*, vol. 160, no. 5, p. 1065, 1967.

[114] E. Ali and D. Rogers, “Implementation of photonuclear attenuation in egsnrc,” *Report CLRP 12*, vol. 1, 2012.

[115] M. Chadwick, P. Oblozinsky, A. Blokhin, T. Fukahori, Y. Han, Y. Lee, M. Martins, S. Mughabghab, V. Varlamov, B. Yu, *et al.*, “Handbook on photonuclear data for applications: Cross sections and spectra,” *IAEA TECH-DOC*, vol. 1178, 2000.

[116] M. Berger, J. Hubbell, S. Seltzer, J. Chang, J. Coursey, R. Sukumar, D. Zucker, and K. Olsen, “Xcom: Photon cross sections database,” *NIST Standard Reference Database*, vol. 8, 2013.

[117] E. Ali, B. Spencer, M. McEwen, and D. Rogers, “Towards a quantitative, measurement-based estimate of the uncertainty in photon mass attenuation coefficients at radiation therapy energies,” *Physics in Medicine & Biology*, vol. 60, no. 4, p. 1641, 2015.

[118] D. E. Cullen, J. H. Hubbell, and L. Kissel, “Epdl97: the evaluated photo data library97 version,” tech. rep., Lawrence Livermore National Lab., CA (United States), 1997.

[119] L. Storm and H. I. Israel, “Photon cross sections from 1 kev to 100 mev for elements z= 1 to z= 100,” *Atomic Data and Nuclear Data Tables*, vol. 7, no. 6, pp. 565–681, 1970.

[120] L. Büermann, B. Grosswendt, H. Kramer, H. Selbach, M. Gerlach, M. Hoffmann, and M. Krumrey, “Measurement of the x-ray mass energy-absorption coefficient of air using 3 kev to 10 kev synchrotron radiation,” *Physics in Medicine & Biology*, vol. 51, no. 20, p. 5125, 2006.

[121] J. Hubbell, “Photon mass attenuation and energy-absorption coefficients,” *The International Journal of Applied Radiation and Isotopes*, vol. 33, no. 11, pp. 1269–1290, 1982.

[122] J. H. Scofield, “Theoretical photoionization cross sections from 1 to 1500 kev,” tech. rep., California Univ., 1973.

[123] L. Sabbatucci and F. Salvat, “Theory and calculation of the atomic photoeffect,” *Radiation Physics and Chemistry*, vol. 121, pp. 122–140, 2016.

[124] S. T. Perkins, D. Cullen, M. Chen, J. Rathkopf, J. Scofield, and J. Hubbell, “Tables and graphs of atomic subshell and relaxation data derived from the llnl evaluated atomic data library (eadl), z= 1–100,” tech. rep., Lawrence Livermore National Lab., CA (United States), 1991.

[125] H. Koch and J. Motz, “Bremsstrahlung cross-section formulas and related data,” *Reviews of modern physics*, vol. 31, no. 4, p. 920, 1959.

[126] S. M. Seltzer and M. J. Berger, “Bremsstrahlung energy spectra from electrons with kinetic energy 1 kev–10 gev incident on screened nuclei and orbital electrons of neutral atoms with z= 1–100,” *Atomic Data and Nuclear Data Tables*, vol. 35, no. 3, pp. 345–418, 1986.

[127] ICRU, “Stopping powers for electrons and positrons. icru report 37. washington, d.c..”

[128] I. Kawrakow, E. Mainegra-Hing, F. Tessier, and B. Walters, “The egsnrc c++ class library nrc report pirs-898 ottawa,” 2017.

[129] S. Agostinelli, J. Allison, K. a. Amako, J. Apostolakis, H. Araujo, P. Arce, M. Asai, D. Axen, S. Banerjee, G. . Barrand, *et al.*, “Geant4—a simulation toolkit,” *Nuclear instruments and methods in physics research section A: Accelerators, Spectrometers, Detectors and Associated Equipment*, vol. 506, no. 3, pp. 250–303, 2003.

[130] J. Hubbell, “Review of photon interaction cross section data in the medical and biological context,” *Physics in Medicine & Biology*, vol. 44, no. 1, p. R1, 1999.

[131] F. Verhaegen and J. Seuntjens, “Monte carlo modelling of external radiotherapy photon beams,” *Physics in medicine & biology*, vol. 48, no. 21, p. R107, 2003.

[132] I. Kawrakow and B. Walters, “Efficient photon beam dose calculations using dosxyznrc with beamnrc,” *Medical physics*, vol. 33, no. 8, pp. 3046–3056, 2006.

[133] D. Bote and F. Salvat, “Calculations of inner-shell ionization by electron impact with the distorted-wave and plane-wave born approximations,” *Physical Review A*, vol. 77, no. 4, p. 042701, 2008.

[134] C.-Y. Yi, K. J. Chun, S.-H. Hah, and H.-M. Kim, "Response characteristics of a cylindrical ionization chamber to the low-and medium-energy x-ray beams," *Journal of Nuclear Science and Technology*, vol. 45, no. sup5, pp. 317–320, 2008.

[135] K. S. Armoogum, J. M. Parry, S. K. Souliman, D. G. Sutton, and C. D. Mackay, "Functional intercomparison of intraoperative radiotherapy equipment–photon radiosurgery system," *Radiation Oncology*, vol. 2, no. 1, p. 11, 2007.

[136] M. Avanzo, A. Rink, A. Dassie, S. Massarut, M. Roncadin, E. Borsatti, and E. Capra, "In vivo dosimetry with radiochromic films in low-voltage intraoperative radiotherapy of the breast," *Medical physics*, vol. 39, no. 5, pp. 2359–2368, 2012.

[137] F. Verhaegen, A. Nahum, S. Van De Putte, and Y. Namito, "Monte carlo modelling of radiotherapy kv x-ray units," *Phys. Med. Biol.*, vol. 44, no. 7, p. 1767, 1999.

[138] F. Verhaegen, "Evaluation of the egsnrc monte carlo code for interface dosimetry near high-z media exposed to kilovolt and 60co photons," *Phys. Med. Biol.*, vol. 47, no. 10, p. 1691, 2002.

[139] J. Hubbell, P. Trehan, N. Singh, B. Chand, D. Mehta, M. Garg, R. Garg, S. Singh, and S. Puri, "A review, bibliography, and tabulation of k, l, and higher atomic shell x-ray fluorescence yields," *J. Phys. Chem. Ref. Data*, vol. 23, no. 2, pp. 339–364, 1994.

[140] D. Eaton, "Electronic brachytherapy - current status and future directions," *Br. Jour. Radiol.*, vol. 88, no. 1049, p. 20150002, 2015.

[141] J. R. Hiatt, M. J. Rivard, and H. G. Hughes, "Simulation evaluation of nist air-kerma rate calibration standard for electronic brachytherapy," *Medical Physics*, vol. 43, no. 3, pp. 1119–1129, 2016.

[142] J. F. Hainfeld, F. A. Dilmanian, D. N. Slatkin, and H. M. Smilowitz, "Radiotherapy enhancement with gold nanoparticles," *J. Pharm. Pharmacol.*, vol. 60, no. 8, pp. 977–986, 2008.

[143] W. U. Shipley, W. C. Wood, J. E. Tepper, A. L. Warshaw, E. L. Orlow, S. D. Kaufman, G. E. Battit, and G. L. Nardi, "Intraoperative electron beam irradiation for patients with unresectable pancreatic carcinoma.," *Annals of surgery*, vol. 200, no. 3, p. 289, 1984.

[144] H. Merrick III, J. Battle, B. Padgett, and R. Dobelbower Jr, "Iort for early breast cancer: A report on long-term results," in *Intraoperative Radiation Therapy in the Treatment of Cancer*, vol. 31, pp. 126–130, Karger Publishers, 1997.

[145] S. Nag, L. L. Gunderson, C. G. Willett, L. B. Harrison, and F. A. Calvo, "Intraoperative irradiation with electron-beam or high-dose-rate brachytherapy," in *Intraoperative irradiation*, pp. 111–130, Springer, 1999.

[146] L. B. Harrison, A. M. Cohen, and W. E. Enker, "High-dose-rate intraoperative irradiation (hdr-iort)," in *Intraoperative Irradiation*, pp. 105–110, Springer, 1999.

[147] C. Z. M. AG, “Intrabeam water phantom - instructions for use.” G-30-1767-en Version 4.0.

[148] J. Seuntjens, I. Kawrakow, J. Borg, F. Hobeila, and D. Rogers, “Calculated and measured air-kerma response of ionization chambers in low and medium energy photon beams,” in *Recent Developments in Accurate Radiation Dosimetry: Proc. Int. Workshop*, pp. 69–84, 2002.

[149] J. Wulff, K. Zink, and I. Kawrakow, “Efficiency improvements for ion chamber calculations in high energy photon beams,” *Medical physics*, vol. 35, no. 4, pp. 1328–1336, 2008.

[150] E. Mainegra-Hing and I. Kawrakow, “Efficient x-ray tube simulations,” *Medical physics*, vol. 33, no. 8, pp. 2683–2690, 2006.

[151] I. Kawrakow, “On the effective point of measurement in megavoltage photon beams,” *Med. Phys.*, vol. 33, no. 6, pp. 1829–1839, 2006.

[152] M. Ebert and B. Carruthers, “Dosimetric characteristics of a low-kv intra-operative x-ray source: Implications for use in a clinical trial for treatment of low-risk breast cancer,” *Medical physics*, vol. 30, no. 9, pp. 2424–2431, 2003.

[153] T. L. Pike, *A dosimetric characterization of an electronic brachytherapy source in terms of absorbed dose to water*. PhD thesis, The University of Wisconsin-Madison, 2012.

[154] S. T, “Towards reference dosimetry of electronic brachytherapy sources,” in *Int. Conf. on Metrology for Brachytherapy*, (Braunschweig), 2017.

[155] R. K. Fulkerson, J. A. Micka, and L. A. DeWerd, “Dosimetric characterization and output verification for conical brachytherapy surface applicators. part i. electronic brachytherapy source,” *Medical physics*, vol. 41, no. 2, 2014.

[156] F. Salvat, J. M. Fernández-Varea, and J. Sempau, “Penelope-2014: A code system for monte carlo simulation of electron and photon transport,” in *Organization for Economic Co-operation and Development, Issy-les-Moulineaux, France*, 2015.

[157] D. J. Brenner, C.-S. Leu, J. F. Beatty, and R. E. Shefer, “Clinical relative biological effectiveness of low-energy x-rays emitted by miniature x-ray devices,” *Physics in medicine and biology*, vol. 44, no. 2, p. 323, 1999.

[158] Q. Liu, F. Schneider, L. Ma, F. Wenz, and C. Herskind, “Relative biologic effectiveness (rbe) of 50 kv x-rays measured in a phantom for intraoperative tumor-bed irradiation,” *International Journal of Radiation Oncology• Biology• Physics*, vol. 85, no. 4, pp. 1127–1133, 2013.

[159] S. A. White, B. Reniers, E. E. De Jong, T. Rusch, and F. Verhaegen, “A comparison of the relative biological effectiveness of low energy electronic brachytherapy sources in breast tissue: a monte carlo study,” *Physics in medicine and biology*, vol. 61, no. 1, p. 383, 2015.

[160] P. Pater, *Numerical Models for Radiation-induced DNA Damage*. PhD thesis, McGill University, 2016.

[161] J. S. Vaidya, D. J. Joseph, J. S. Tobias, M. Bulsara, F. Wenz, C. Saunders, M. Alvarado, H. L. Flyger, S. Massarut, W. Eiermann, *et al.*, "Targeted intraoperative radiotherapy versus whole breast radiotherapy for breast cancer (targit-a trial): an international, prospective, randomised, non-inferiority phase 3 trial," *The Lancet*, vol. 376, no. 9735, pp. 91–102, 2010.

[162] R. Siochi, "Th-ab-201-02: A tg-61 calibration method for the zeiss intrabeam with spherical applicators," *Medical physics*, vol. 43, no. 6, pp. 3849–3849, 2016.

[163] M. A. Ebert, A. H. Asad, and S. A. Siddiqui, "Suitability of radiochromic films for dosimetry of low energy x-rays," *Journal of applied clinical medical physics*, vol. 10, no. 4, pp. 232–240, 2009.

[164] K. Armoogum and C. Watson, "A dosimetry intercomparison phantom for intraoperative radiotherapy," *Zeitschrift für Medizinische Physik*, vol. 18, no. 2, pp. 120–127, 2008.

[165] J. Sutherland and D. Rogers, "Monte carlo calculated absorbed-dose energy dependence of ebt and ebt2 film," *Medical physics*, vol. 37, no. 3, pp. 1110–1116, 2010.

[166] C. G. Hammer, B. S. Rosen, J. M. Fagerstrom, W. S. Culberson, and L. A. DeWerd, "Experimental investigation of gafchromic® ebt3 intrinsic energy dependence with kilovoltage x rays, 137cs, and 60co," *Medical physics*, vol. 45, no. 1, pp. 448–459, 2018.

[167] C. Orton and J. Seibert, "The measurement of teletherapy unit timer errors," *Physics in medicine and biology*, vol. 17, no. 2, p. 198, 1972.

[168] C. Ma and J. Seuntjens, "Mass-energy absorption coefficient and backscatter factor ratios for kilovoltage x-ray beams," *Physics in medicine and biology*, vol. 44, no. 1, p. 131, 1999.

[169] B. I. des Poids et Mesures, C. électrotechnique internationale, and O. internationale de normalisation, *Guide to the expression of uncertainty in measurement*. International Organization for Standardization, 1995.

[170] G. Poludniowski, G. Landry, F. DeBlois, P. Evans, and F. Verhaegen, "Spekcalc: a program to calculate photon spectra from tungsten anode x-ray tubes," *Physics in medicine and biology*, vol. 54, no. 19, p. N433, 2009.

[171] M. J. Berger, "Xcom: Photon cross section database," *http://www. nist. gov/pml/data/xcom/index. cfm*, 1998.

[172] J. P. Seuntjens, "Aapm tg-61 report on kilovoltage x-ray dosimetry. ii. calibration procedures and correction factors," in *Engineering in Medicine and Biology Society, 2000. Proceedings of the 22nd Annual International Conference of the IEEE*, vol. 3, pp. 2313–2316, IEEE, 2000.

[173] P. Papaconstadopoulos, G. Hegyi, J. Seuntjens, and S. Devic, "A protocol for ebt3 radiochromic film dosimetry using reflection scanning," *Medical physics*, vol. 41, no. 12, 2014.

[174] S. Devic, N. Tomic, C. G. Soares, and E. B. Podgorsak, “Optimizing the dynamic range extension of a radiochromic film dosimetry system,” *Medical physics*, vol. 36, no. 2, pp. 429–437, 2009.

[175] S. Devic, J. Seuntjens, G. Hegyi, E. B. Podgorsak, C. G. Soares, A. S. Kirov, I. Ali, J. F. Williamson, and A. Elizondo, “Dosimetric properties of improved gafchromic films for seven different digitizers,” *Medical physics*, vol. 31, no. 9, pp. 2392–2401, 2004.

[176] S. Aldelaijan, S. Devic, H. Mohammed, N. Tomic, L.-H. Liang, F. DeBlois, and J. Seuntjens, “Evaluation of ebt-2 model gafchromic™ film performance in water,” *Medical physics*, vol. 37, no. 7, pp. 3687–3693, 2010.

[177] D. Lewis. unpublished work.

[178] D. R. Holmes, “Early complications after intraoperative radiotherapy revisited,” *Journal of surgical oncology*, vol. 115, no. 7, pp. 779–781, 2017.

[179] F. Moradi, N. Ung, M. Khandaker, G. Mahdiraji, M. Saad, R. A. Malik, A. Bustam, Z. Zaili, and D. Bradley, “Monte carlo skin dose simulation in intraoperative radiotherapy of breast cancer using spherical applicators,” *Physics in Medicine & Biology*, vol. 62, no. 16, p. 6550, 2017.

[180] G. Landry, B. Reniers, L. Murrer, L. Lutgens, B.-V. Gurp, J.-P. Pignol, B. Keller, L. Beaulieu, F. Verhaegen, *et al.*, “Sensitivity of low energy brachytherapy monte carlo dose calculations to uncertainties in human tissue composition,” *Medical physics*, vol. 37, no. 10, pp. 5188–5198, 2010.

[181] S. A. White, G. Landry, G. P. Fonseca, R. Holt, T. Rusch, L. Beaulieu, F. Verhaegen, and B. Reniers, “Comparison of tg-43 and tg-186 in breast irradiation using a low energy electronic brachytherapy source,” *Medical physics*, vol. 41, no. 6Part1, 2014.

[182] M. J. Rivard, B. M. Coursey, L. A. DeWerd, W. F. Hanson, M. Saiful Huq, G. S. Ibbott, M. G. Mitch, R. Nath, and J. F. Williamson, “Update of aapm task group no. 43 report: A revised aapm protocol for brachytherapy dose calculations,” *Medical physics*, vol. 31, no. 3, pp. 633–674, 2004.

[183] M. J. Silverstein, M. S. Epstein, K. Lin, P. Chen, S. Khan, L. Snyder, L. E. Guerra, C. De Leon, R. Mackintosh, C. Coleman, *et al.*, “Intraoperative radiation using low-kilovoltage x-rays for early breast cancer: A single site trial,” *Annals of surgical oncology*, vol. 24, no. 10, pp. 3082–3087, 2017.

[184] H.-W. Lai, L.-C. Liu, F. Ouyang, C.-C. Yao, H.-C. Jan, Y.-H. Chang, C.-W. Tu, D.-R. Chen, T.-F. Cheng, Y.-D. Tzeng, *et al.*, “Multi-center study on patient selection for and the oncologic safety of intraoperative radiotherapy (iort) with the xoft axxent® ebx® system for the management of early stage breast cancer in taiwan,” *PloS one*, vol. 12, no. 11, p. e0185876, 2017.

[185] S. Chiavassa, F. Buge, C. Hervé, G. Delpon, J. Rigaud, A. Lisbona, and S. Supiot, “Monte carlo evaluation of the effect of inhomogeneities on dose calculation for low energy photons intra-operative radiation therapy in pelvic area,” *Physica Medica*, vol. 31, no. 8, pp. 956–962, 2015.

[186] D. Bouzid, J. Bert, P.-F. Dupre, S. Benhalouche, O. Pradier, N. Boussion, and D. Visvikis, “Monte-carlo dosimetry for intraoperative radiotherapy using a low energy x-ray source,” *Acta Oncologica*, vol. 54, no. 10, pp. 1788–1795, 2015.

[187] F. Schneider, F. Bludau, S. Clausen, J. Fleckenstein, U. Obertacke, and F. Wenz, “Precision iort–image guided intraoperative radiation therapy (igiort) using online treatment planning including tissue heterogeneity correction,” *Physica Medica*, vol. 37, pp. 82–87, 2017.